October 2019

CHARACTERIZATION OF THE ANOMALOUS pH OF AQUEOUS NANOEMULSIONS

Kieran P. Ramos
University of Massachusetts Amherst

CHARACTERIZATION OF THE ANOMALOUS pH OF AQUEOUS NANOEMULSIONS

A Dissertation Presented

by

KIERAN P. RAMOS

Submitted to the Graduate School of the
University of Massachusetts Amherst in partial fulfillment
of the requirements for the degree of

DOCTOR OF PHILOSOPHY

September 2019

Physics

CHARACTERIZATION OF THE ANOMALOUS pH OF AQUEOUS NANOEMULSIONS

A Dissertation Presented

by

KIERAN P. RAMOS

Approved as to style and content by:

_____

Lori S. Goldner, Chair

_____

Anthony D. Dinsmore, Member

_____

Narayanan Menon, Member

_____

Sarah L. Perry, Member

_____

Narayanan Menon, Department Chair
Physics

DEDICATION

To my beloved wife Nina, my parents, and my brothers.

ACKNOWLEDGMENTS

I would like to give my thanks all the people who helped make this dissertation possible. In particular, I would like to express my sincere gratitude to my research supervisor Lori Goldner for her support and mentorship throughout. The other members of my dissertation committee: Anthony Dinsmore, Sarah Perry, and Narayanan Menon for their insightful thoughts and comments. My wife Nina Zehfroosh for her invaluable scientific discussions and endless patience. Sandra Petersen and all other members of NEAGEP for their support and mentorship. All members of the Goldner laboratory and neighboring laboratories who provided assistance and discussion. Trevor Demille for his contribution to the data in this dissertation. Chang Kee Jung and all other members of the NN Group at Stony Brook University for their mentorship and encouragement to pursue a doctoral degree. And to the open-source software community for their generous contributions to public knowledge.

I would also like to express my eternal appreciation towards my family and friends who have always been there for me and for all their unconditional love and support. My parents who taught me ingenuity and patience. My dear friend Brad who always inspired my scientific thought and creativity. And to my wife again for standing by my side and for her never ending motivation.

ABSTRACT

CHARACTERIZATION OF THE ANOMALOUS pH OF AQUEOUS NANOEMULSIONS

SEPTEMBER 2019

KIERAN P. RAMOS

B.S., STONY BROOK UNIVERSITY

M.S., UNIVERSITY OF MASSACHUSETTS

Ph.D., UNIVERSITY OF MASSACHUSETTS AMHERST

Directed by: Professor Lori S. Goldner

Aqueous water-in-oil nanoemulsions have emerged as a versatile tool for use in microfluidics, drug delivery, single-molecule measurements, and other research. Nanoemulsions are often prepared with perfluorocarbons which are remarkably biocompatbile due to their stability, low surface tension, lipophobicity, and hydrophobicity. Therefore it is often assumed that droplet contents are unperturbed by the perfluorinated surface. However, in microemulsions, which are similar to nanoemulsions, it is known that either the pH of the aqueous phase or the ionization constants of encapsulated molecules are different from bulk solution. There is also recent evidence of low pH in perfluorinated aqueous nanoemulsions. The current underlying theory is that hydroxide ions aggregate at the oil-water interface leaving the bulk of the emulsion more acidic than usual.

In this work, I measured the pH of aqueous nanoemulsions and sub-micron emulsions prepared by ultrasonication using Fluorinert FC-40 and a nonionic surfactant, PFPE–PEG–PFPE. To measure pH I measured a fluorescence emis-

sion ratio of a pH sensitive fluorophore, either fluorescein or difluorofluorescein (commonly called Oregon Green 488), with two apparatus: a fluorimeter for measuring ensemble pH, and a fluorescence microscope for measuring pH and size of single-droplets simultaneously. After lookup of emission ratio in a predetermined instrument–fluorophore calibration, the pH is determined.

For fluorimeter measurements I developed a novel bayesian analytical model that accounts for the aqueous solution buffer capacity giving meaningful uncertainty estimates in the pH measurements. Fits to the fluorimeter calibration curve using currently established models of fluorescein were unsuccessful in obtaining a perfect fit therefore it is likely that these models are still incomplete; a heuristic model was used instead. For droplet measurements I obtained two data series as a function of sodium hydroxide concentration and as a function of surfactant concentration. Assuming hydroxide ions aggregate at the droplet surface both series predict a surface charge density of $0.04\,\mathrm{OH^-\,nm^{-2}}$ to $0.4\,\mathrm{OH^-\,nm^{-2}}$. The measurements indicated a decrease in charging with an increase in surfactant concentration and an increase in charging with an increase in sodium hydroxide concentration.

The primary goal of single-droplet measurements was to measure pH as a function of size. Measuring pH involved a dual-view optical setup, affine transformation of image data, and three dimensional (position and time) lookup of emission ratio in the instrument–fluorophore calibration. Measuring droplet size involved single-particle tracking to obtain particle mean square displacements (MSDs) and fitting of the MSDs. In total I have data on 12 785 droplets using many aqueous sample solution conditions and emulsion preparation conditions. Measurements predicted a surface charge density of $0.08\,\mathrm{OH^-\,nm^{-2}}$ to $0.32\,\mathrm{OH^-\,nm^{-2}}$ with the same trends in surfactant concentration and buffer concentration as in the fluorimeter measurements. As expected there was a decrease in charging with an increase in size. To mitigate surface charging I recommend working with 4 wt% surfactant concentration or greater.

CONTENTS

Page

LIST OF TABLES

Table **Page**

LIST OF FIGURES

CHAPTER 1

INTRODUCTION

Emulsions are dispersions of one liquid as droplets in another immiscible liquid. These liquids are called the dispersed phase and the continuous phase, respectively. Emulsions can be categorized into size regimes that, broadly speaking, predict the physical and chemical properties of the emulsion. Nanoemulsions (also formerly referred to as miniemulsions, colloidal emulsions, and ultrafine emulsions) are kinetically stable dispersions where the mean droplet radius is less than 100 nm [1–3]. To make nanoemulsions it is usually necessary to apply large shear forces typically via vigorous mixing, ultra-sonication, or homogenization. Nanoemulsions share many characteristics with typical emulsions in the micron and submicron range so they will age via Ostwald ripening, flocculation, coalescence, and gravitational separation; however, due to their smaller size they are optically transparent or translucent, and more stable against gravitational separation which includes sedimentation and creaming.

Nanoemulsions, especially those made with perfluorocarbon liquids (PFCs), are currently being evaluated for their use in the area of nanomedicine such as the use of nano-carriers including liposomes and micelles for drug delivery and gene delivery [4–7]. PFCs are also sought after for their high gas solubility and good oxygen transport properties for use as a blood replacement [6]. The major benefit of PFCs is their biologic inertness and low toxicity; however, for PFCs to be useful any effects of PFC nanoemulsions on their encapsulated drugs and genes must be well understood.

Perfluorocarbon nano- and sub-micron- water-in-oil (W/O) inverse emulsions have also been useful in single-molecule studies of RNA confined within the droplets [8–10]. With recent advancements in droplet microfluidics it is now

also possible to generate submicron emulsions by either flow focusing [11], using a T-junction [12], or by splitting larger droplets [13, 14]. And, although not submicron, there have been single-molecule studies in approximately 2.5 µm diameter droplets including a single-enzyme study [15] and a single-quantum-dot detection [16]. As researchers continue to push the boundaries of microfluidic single-molecule measurements they will be more often working with sub-micron- and nanoemulsions. Although this has many potential benefits, as the droplet diameter shrinks below 1 µm, the surface area to volume ratio increases rapidly and the possibility of perturbations to the molecules under study due to interactions of the molecules with the droplet surface also increases rapidly. Then it is critical that the effects of the oil-water interface on entrapped molecules are well understood for the success of future single-molecule in droplet experiments.

Microemulsions are another class of emulsions which are isotropic, thermodynmically stable, optically transparent, and formed by simply mixing oil, water, and surfactant [1, 3]. When surfactant is added to an oil the individual surfactant molecules tend to aggregate presumably due to the inability to completely remove water from the surfactant. When extra water is added to this system the aggregates swell and become what is called a reverse micelle (RM), a type of microemulsion, which contain a water pool. RMs typically have a diameter of about 5 nm to 100 nm, a non-uniform interior due to the surfactant head groups, and a microviscosity environment [17]. In comparison to nanoemulsions, microemulsion have been much more widely studied [1] especially in regards to the characterization of the water pool and behavior of entrapped molecules.

Various enzymes and proteins including intracellular, extracellular, and membrane proteins have been entrapped in RMs usually with no change to their conformation or activities [18]. On the contrary there have been many studies showing change to the acid-base equilibria in thin films, in micellar solutions and within the water pool of RMs [17–26]. The change in acid-base equilibria has been attributed to a change in the ionization constant due to a “medium effect”, when the molecules are adsorbed at neutral interfaces, and an

“electrostatic effect”, when a charged interface perturbs the equilibrium state due to repulsions, which both contribute to an apparent ionization constant [19]. This change has many dependencies including the type of ions, ionic strength, and water-to-surfactant ratio.

The changes to acid-base equilibria have not only been attributed to changes in the ionization constants but also to changes in the effective pH due to the confined water environment. There have been many methods of probing the these environments including: use of pH sensitive fluoresceins dyes [20], nuclear magnetic resonance of decavanadate (a highly charged molecule known to exist in the water pool) [21, 22], without a probe molecule via proton nuclear magnetic resonance [23], and with C-SNARF-1 (a pH sensitive fluorophore) to probe thin films [24, 25]. In all cases, when probing pH or ionization constant shifts it is important that the location of the probe molecule is considered to not misinterpret the data [26]. And it is also possible that the probe molecule itself alters the environment and changes the measurement [27].

Despite the vast amount of literature on measuring pH or ionization constant shifts in micellar, reverse micellar, and thin film systems there is a void of these types of measurements in nanoemulsions. However, in general it is known that oil-water interfaces can become charged due to adsorption of hydroxide ions in the presence or absence of nonionic surfactants [28–34]. Since nanoemulsions are emerging as a new technique for single-molecule measurements and there are bountiful evidence of anomalous pH in similar systems, in this dissertation I will discuss my work on characterizing the pH of water-in-oil (W/O) reverse nanoemulsions and submicron emulsions made from a PFC liquid, Fluorinert™ FC-40, and various aqueous samples with and without added nonionic surfactant.

CHAPTER 2

BACKGROUND

2.1 pH

2.1.1 What is pH?

pH is defined and standardized by the International Union of Pure and Applied Chemistry (IUPAC) [35] as the cologarithm of the activity of the hydrogen ion in solution,

$$\mathrm{pH} = -\log a_{\mathrm{H^+}}, \tag{2.1}$$

where p is an operator that takes the cologarithm $\mathrm{p}x = -\log_{10}(x)$. The activity of a solute B, a_{B}, is a dimensionless quantity that measures the "effective concentration" of solute B and is defined in terms of the chemical potential, μ_{B},

$$a_{\mathrm{B}} = \exp\left(\frac{\mu_{\mathrm{B}} - \mu_{\mathrm{B}}^{\circ}}{RT}\right), \tag{2.2}$$

and the ideal gas constant, R [35]. $\mu_{\mathrm{B}}^{\circ}(T, p^{\circ}, c^{\circ})$ is the standard chemical potential of solute B in a solution at temperature T, the standard pressure $p^{\circ} = 100\,\mathrm{kPa}$, and standard concentration $c^{\circ} = 1\,\mathrm{mol\,L^{-1}}$ and referenced to the ideal dilute behavior of the solute [35]. Therefore the activity and thus the pH depend on any factors that affect the chemical potential including the types of ions in solution due to ion pair interactions, concentrations of all ions, temperature, and pressure.

It is common practice to define the activity in terms of a dimensionless activity coefficient $\gamma_{c,\mathrm{B}}$ such that the activity can be written in terms of the solute concentration

$$a_{\mathrm{B}} = \gamma_{c,\mathrm{B}} \frac{c_{\mathrm{B}}}{c^{\circ}}. \tag{2.3}$$

The subscript c in the activity coefficient is to indicate that it may depend on the solute concentration and for brevity will be henceforth dropped. Also since $c^\circ = 1\,\mathrm{mol\,L^{-1}}$ then it will be dropped with the assumption that all further concentrations are in $\mathrm{mol\,L^{-1}}$. The activity coefficient is a measure of how much the behavior of ions in a solution deviate from ideal behavior.

Its important to note that it is not thermodynamically possible to measure the activity of individual ionic species since the concentrations of single ionic species are not individually controllable in ionic solutions [36]. In other words the concentration of NaCl in solution is controllable but the concentrations of $\mathrm{Na^+}$ and $\mathrm{Cl^-}$ are not independently variables. Thus consider an electrolyte and its dissociation, $\mathrm{C}_{\nu+}\mathrm{A}_{\nu-} \longrightarrow \nu_+\mathrm{C} + \nu_-\mathrm{A}$ where ν_+ and ν_- are the stoichiometric number of the positive and negative ions respectively. The activity of the electrolyte may be written as $a(\mathrm{C}_{\nu+}\mathrm{A}_{\nu-}) = {a_+}^{\nu_+}{a_-}^{\nu_-} = {a_\pm}^{\nu}$ and its activity coefficient as $\gamma = {\gamma_+}^{\nu_+}{\gamma_-}^{\nu_-} = {\gamma_\pm}^{\nu}$ where $a_\pm$ and $\gamma_\pm$ are the thermodynamically measurable quantities termed the mean ionic activity and mean ionic activity coefficient respectively and $\nu = \nu_+ + \nu_-$ [35, 36]. It is not possible to measure a_+ or a_- separately and similarly for γ_+ and γ_-.

2.1.2 How do we measure pH?

What this means is that pH is not a directly measurable quantity. Instead the primary standard method of measuring pH is via a *Harned Cell* which measures $\mathrm{p}(a_{\mathrm{H^+}}\gamma_{\mathrm{Cl^-}}) = -\log a_{\mathrm{H^+}}\gamma_{\mathrm{Cl^-}}$ where $\gamma_{\mathrm{Cl^-}}$ is calculated from Debye-Hückel theory using the Bates-Guggenheim convention [37]. This method produces primary and secondary standard buffers of known pH which can then used with a secondary method of measuring pH. The more commonly used secondary method is via ion-selective glass electrodes that have a liquid junction and must be standardized by calibrating with primary or secondary buffers. Thus pH measurement via the common glass electrode is fully traceable to the International System of Units (SI) with a typical uncertainty of 0.02 to 0.04 when doing a 5-point calibration [37]. In this dissertation I always measured

pH using an Accumet AB15+ meter and Thermo Scientific 9110DJWP double junction electrode calibrated daily with a 5-point calibration to a mix of NIST traceable primary and secondary buffers.

2.1.3 How do we control pH?

Buffer solutions are aqueous mixtures of weak acids or weak bases that buffer against changes in the solution pH. Weak acids and bases as opposed to strong acids and bases do not fully dissociate in water which give them their buffering ability. Consider the dissociation of a weak monoprotic acid in water $\mathrm{HA} \overset{K_a}{\longleftrightarrow} \mathrm{H^+} + \mathrm{A^-}$. The amount of reactants and products must satisfy the equilibrium condition

$$K_a = \frac{a_{\mathrm{H^+}} a_{\mathrm{A^-}}}{a_{\mathrm{HA}}} = \frac{a_{\mathrm{H^+}} c_{\mathrm{A^-}}}{c_{\mathrm{HA}}} \frac{\gamma_{\mathrm{A^-}}}{\gamma_{\mathrm{HA}}} \tag{2.4}$$

where c_i indicates the concentration of species i in $\mathrm{mol\,L^{-1}}$ and K_a is called the acid equilibrium constant which must be measured for each acid.

An important characteristic of a buffer solution is its buffer capacity,

$$\beta = \frac{\mathrm{d}n}{\mathrm{dpH}}, \tag{2.5}$$

where $\mathrm{d}n$ is an infinitesimal addition of infinitely strong base. The buffer capacity is a measure of the ability of a buffer solution to resist changes in pH. To derive a formula for buffer capacity first consider that the total concentration of acid added to solution, C_a, must be fixed such that

$$C_a = c_{\mathrm{HA}} + c_{\mathrm{A^-}}. \tag{2.6}$$

And that after addition of base, $\mathrm{BOH} \longrightarrow \mathrm{B^+} + \mathrm{OH^-}$, the solution must be electrically neutral such that

$$c_{\mathrm{OH^-}} + c_{\mathrm{A^-}} = c_{\mathrm{H^+}} + c_{\mathrm{B^+}} = {\gamma_{\mathrm{H^+}}}^{-1} 10^{-\mathrm{pH}} + n \tag{2.7}$$

where I have used $c_{\mathrm{B^+}} = n$ and $c_{\mathrm{H^+}} = {\gamma_{\mathrm{H^+}}}^{-1} 10^{-\mathrm{pH}}$ [from eqs. (2.1) and (2.3)] to write the last step. Finally the most common weak electrolyte is water itself which dissociates as $\mathrm{H_2O} \longleftrightarrow \mathrm{H^+} + \mathrm{OH^-}$. This reaction is called the self-dissociation of water and its ionization constant is termed the self-ionization of water. The commonly accepted value is $K_w = 1.008 \times 10^{-14}$ at 25 °C as reported by Harned [36] where K_w is defined as

$$K_w = \frac{a_{\mathrm{H^+}} a_{\mathrm{OH^-}}}{a_{\mathrm{H_2O}}} = \frac{10^{-\mathrm{pH}} \gamma_{\mathrm{OH^-}} c_{\mathrm{OH^-}}}{a_{\mathrm{H_2O}}} \approx 10^{-\mathrm{pH}} \gamma_{\mathrm{OH^-}} c_{\mathrm{OH^-}}. \tag{2.8}$$

The approximation I have taken is for dilute solutions where $a_{\mathrm{H_2O}} \approx 1$.

By combining eqs. (2.4) to (2.8) its possible to arrive at the following equation for buffer capacity

$$\beta = \ln(10) \left(\frac{K_w}{\gamma_{\mathrm{OH^-}} 10^{-\mathrm{pH}}} + \frac{10^{-\mathrm{pH}}}{\gamma_{\mathrm{H^+}}} + \frac{10^{-\mathrm{pH}} C_a K_a \gamma_{\mathrm{A^-}} \gamma_{\mathrm{HA}}}{(K_a \gamma_{\mathrm{HA}} + \gamma_{\mathrm{A^-}} 10^{-\mathrm{pH}})^2} \right). \tag{2.9}$$

The previous derivation has been for a single monoprotic acid. If multiple monoprotic acids are in solution then each acid has a contribution to the buffer strength that goes exactly as the last term in the previous equation therefore that term becomes a sum over all acids

$$\beta = \ln(10) \left(\frac{K_w}{\gamma_{\mathrm{OH^-}} 10^{-\mathrm{pH}}} + \frac{10^{-\mathrm{pH}}}{\gamma_{\mathrm{H^+}}} + \sum_{\text{acids}} \left\{ \frac{10^{-\mathrm{pH}} C_a K_a \gamma_{\mathrm{A^-}} \gamma_{\mathrm{HA}}}{(K_a \gamma_{\mathrm{HA}} + \gamma_{\mathrm{A^-}} 10^{-\mathrm{pH}})^2} \right\} \right). \tag{2.10}$$

In the case of a polyprotic acid there are multiple ionizations steps and thus multiple ionization constants. Take for example citric acid in which the citrate ion has a -3 charge and thus the following dissociations

$$\mathrm{H_3Citrate} \overset{K_{a1}}{\rightleftharpoons} \mathrm{H^+} + \mathrm{H_2Citrate^-} \tag{2.11a}$$

$$\mathrm{H_2Citrate^-} \overset{K_{a2}}{\rightleftharpoons} \mathrm{H^+} + \mathrm{HCitrate^{2-}} \tag{2.11b}$$

$$\mathrm{HCitrate^{2-}} \overset{K_{a3}}{\rightleftharpoons} \mathrm{H^+} + \mathrm{Citrate^{3-}}. \tag{2.11c}$$

To derive a formula for the buffer capacity of citrate and other polyprotic acids it is helpful to define the equilibrium constant as follows

$$K_{ai} = \prod_{\mathrm{B}} {a_{\mathrm{B},i}}^{\nu_{\mathrm{B},i}} = \prod_{\mathrm{B}} {\gamma_{\mathrm{B},i}}^{\nu_{\mathrm{B},i}} {c_{\mathrm{B},i}}^{\nu_{\mathrm{B},i}} \tag{2.12}$$

where $\nu_{\mathrm{B},i}$ is the stoichiometric number of a reactant (negative) or product (positive) for the ith reaction [35]. In this way i equals the modulus of the ion charge: $i = |z|$. From here I will define an effective equilibrium constant that absorbs all activity coefficients

$$K_{ai,\mathrm{ef}} = K_{ai} \prod_{\mathrm{B}\neq\mathrm{H}^+} {\gamma_{\mathrm{B},i}}^{-\nu_{\mathrm{B},i}} = {a_{\mathrm{H}^+,i}}^{\nu_{\mathrm{H}^+,i}} \prod_{\mathrm{B}\neq\mathrm{H}^+} {c_{\mathrm{B},i}}^{\nu_{\mathrm{B},i}} \tag{2.13}$$

where the product runs over all solutes except H^+. Using this definition I derive the following formula for the buffer capacity of a polyprotic acid as a function of pH

$$\beta = \ln(10)\left(\frac{K_w}{\gamma_{\mathrm{OH}^-}10^{-\mathrm{pH}}} + \frac{10^{-\mathrm{pH}}}{\gamma_{\mathrm{H}^+}} - \frac{AB - CD}{B^2}\right) \tag{2.14}$$

$$A = C_a \sum_{j=1}^{N} j(N-j)\alpha_j$$

$$B = 10^{-N\mathrm{pH}} + \sum_{j=1}^{N} \alpha_j$$

$$C = C_a \sum_{j=1}^{N} j\alpha_j$$

$$D = N10^{-N\mathrm{pH}} + \sum_{j=1}^{N} (N-j)\alpha_j$$

$$\alpha_j = 10^{-(N-j)\mathrm{pH}} \prod_{i=1}^{j} K_{ai,\mathrm{ef}}$$

where the total concentration $C_a = \sum_{i=0}^{N} c_i$ runs over all acid ions and neutral forms. As in the monoprotic case if more than one type of acid is in the solution then additional terms can be added for each acid.

To calculate the buffer capacity it is necessary to know the activity coefficients which arise from electrostatic ion pair interactions which depends on the specific combination of all ions in solution. An approximation of the activity coefficients can be calculated from Debye-Hückel theory [38, 39] which states that

$$\log \gamma_{\pm} = -A|z_{+}z_{-}|\frac{\sqrt{I}}{1 + B\mathring{a}\sqrt{I}} \tag{2.15}$$
$$A = \frac{e^2 B}{\ln(10) \times 8\pi\epsilon_0\epsilon_r kT}$$
$$B = \left(\frac{2e^2 N}{\epsilon_0\epsilon_r kT}\right)^{1/2}$$

where $\mathring{a}$ is the distance of closest approach of the ion pair; at 25 °C $A = 0.510\,\mathrm{mol}^{-1/2}\,\mathrm{L}^{1/2}$ and $B = 3.288\,\mathrm{nm}^{-1}\,\mathrm{mol}^{-1/2}\,\mathrm{L}^{1/2}$; and I is the ionic strength defined as

$$I = \frac{1}{2}\sum_{i=1}^{n} c_i {z_i}^2 \tag{2.16}$$

where z_i is the charge of the ith ion and the sum runs over all ions in solution. However, the activity coefficient determined by the Debye-Hückel equation is only useful for ionic strengths up to $0.1\,\mathrm{mol\,L}^{-1}$ and this model requires knowledge of $\mathring{a}$ which varies by ion pair.

For use at higher ionic strengths and without the need of $\mathring{a}$ a commonly used model and the one I used in my calculations is the Davies Equation [40]. This model was empirically determined by analysis of a large variety of electrolytes and found to have an average deviation of only 1.6 % for uni-univalent electrolytes at $0.1\,\mathrm{mol\,L}^{-1}$ ionic strength by Davies [40]. It has the following form

$$\log \gamma_{\pm} = -A|z_1 z_2|\left(\frac{\sqrt{I}}{1 + \sqrt{I}} - 0.30I\right). \tag{2.17}$$

Finally the activity coefficient of non-electrolytes such as undissolved acetic acid (CH_3COOH) follows a salting out or salting in model that depends linearly on the ionic strength [36]. The slopes of these models depend on the type of salt that increases the solution ionic strength but are typically very small therefore

T (°C)	$K_w \times 10^{-14}$	T (°C)	$K_w \times 10^{-14}$
0	0.114	55	7.244
5	0.186	60	9.550
10	0.293	65	12.58
15	0.457	70	15.85
20	0.681	75	20.42
25	1.008	80	25.12
30	1.471	85	30.90
35	2.089	90	38.02
40	2.916	95	45.71
45	4.074	100	51.30
50	5.476		

Table 2.1. The temperature dependence of the self-ionization constant of water [36].

taking the activity coefficient as unity is a good approximation. For example acetic acid in an $0.2\,\mathrm{mol\,L^{-1}}$ ionic strength solution with NaCl as the salt the activity coefficient of undissolved acid is about 1.026, only a 2.6 % deviation [36]. Since I do not know the slope of the salting out model for my specific solutions, and the deviation is small for low ionic strengths, I use a value of 1 for any non-electrolytes.

In all calculations the ionization constants were corrected to the temperature of the experiment. The standard $\mathrm{p}K_a$ is usually specified at 25 °C and any temperature variation if known can be applied as

$$\mathrm{p}K_{a,T\,^\circ\mathrm{C}} = \mathrm{p}K_{a,25\,^\circ\mathrm{C}} + (T - 25)\frac{\mathrm{d}\mathrm{p}K_a}{\mathrm{d}T}. \tag{2.18}$$

This correction should be applied before calculation of the effective equilibrium constant since the temperature variation should be specified at infinite dilution. I also corrected the self-ionization constant of water for temperature variation by using a cubic B-spline through the data in table 2.1.

2.1.4 Preparation of pH buffered solutions

To prepare a pH buffered solution it is necessary to mix a weak acid with a strong base or strong acid depending on the desired final pH. If a higher ionic strength is desired then it is necessary to add an inert salt. For all samples HCl and NaOH were used as the strong acid and strong base respectively and NaCl was used as an inert salt.

The first step is to specify the desired total weak acid concentration, C_a, pH, and ionic strength I. The second step is to calculate the amount of strong acid or strong base necessary to obtain the desired pH from the electro-neutrality condition,

$$c_{\mathrm{OH^-}} + c_{\mathrm{Cl^-}} + \sum_{i=1}^{N} i c_i = c_{\mathrm{H^+}} + c_{\mathrm{Na^+}}, \tag{2.19}$$

where $c_{\mathrm{Cl^-}}$ and $c_{\mathrm{Na^+}}$ arise from addition of HCl or NaOH or NaCl. The calculation is done with activity and temperature corrected ionization constants therefore the calculation must be repeated until there is only a small deviation in the ionic strength (e.g. 1 ppm). The third step is to calculate the amount of inert salt, NaCl, or equivalently equal amounts strong acid (HCl) and strong base (NaOH), using the same electro-neutrality condition, eq. (2.19), using the amount of weak acid from the second step. Again this calculation must be iterated until the change in the calculated ionic strength is small (e.g. 1 ppm). Finally the results of the second and third steps, respectively, the amounts of weak acid and inert salt, are combined to calculate the solution pH and ionic strength. If the resultant pH and ionic strength are close enough to the targets set in the first step (e.g. 1 ppm) then the calculation is done; otherwise, the second through fourth steps are repeated using the results of the previous iteration until this condition is satisfied.

After a buffered solution is prepared and its pH is measured a new ionic strength can be calculated again by satisfying the electro-neutrality condition, eq. (2.19), using the known concentrations of the constituents and known pH.

This estimation is likely more accurate since the electrochemical theory is only relied upon for the ionic strength calculation.

2.2 Emulsions

Emulsions are dispersions of two or more immiscible liquids in which one liquid is dispersed in another and often stabilized by surfactants and cosurfactants. In this study emulsions are made with aqueous buffered solutions dispersed in Fluorinert™ FC-40,* a fully perfluorinated liquid. The surfactant used in this work was PFPE–PEG–PFPE, a triblock copolymer of perfluoropolyether (PFPE) and polyethyleneglycol (PEG) [41] where the molar masses were $M_{\mathrm{PFPE}} \approx 6000\,\mathrm{g\,mol^{-1}}$ and $M_{\mathrm{PEG}} \approx 600\,\mathrm{g\,mol^{-1}}$. Therefore the degree of polymerization was $N_{\mathrm{PFPE}} = 40$ to 45 and $N_{\mathrm{PEG}} = 10$ to 12 [42]. The surfactant was purchased from RAN Biotechnologies [43].

This surfactant is miscible in the FC-40 continuous phase and immiscible in water thus mixtures of surfactant and FC-40 were prepared first and the mixtures used for making emulsions. The surfactant mixtures were prepared by weight at concentrations ranging from 0 wt% to 10 wt%. Using the molar mass of FC-40, $M \approx 650\,\mathrm{g\,mol^{-1}}$, the density of FC-40, $\rho = 1.855\,\mathrm{kg\,m^{-3}}$, the total molar mass of the surfactant $M \approx 12\,600\,\mathrm{g\,mol^{-1}}$, and assuming the density of the surfactant is $\rho \approx 1.8\,\mathrm{kg\,m^{-3}}$ (provided by the manufacturer) it is possible to convert wt% to $\mathrm{mol\,L^{-1}}$. Thus the concentration range of surfactant I used was $0\,\mathrm{mmol\,L^{-1}}$ to $14.7\,\mathrm{mmol\,L^{-1}}$. The critical micelle concentration (CMC) of this surfactant in FC-40 has been reported as $40\,\mu\mathrm{mol\,L^{-1}}$ or approximately 0.027 wt% [42].

---

*Fluorinert™ FC-40 Electronic Liquid is a trademark of 3M™ and its composition is perfluorotri-*n*-butylamine ($C_{12}F_{27}N$) mixed with perfluoro-*n*-dibutylmethylamine ($C_9F_{21}N$).

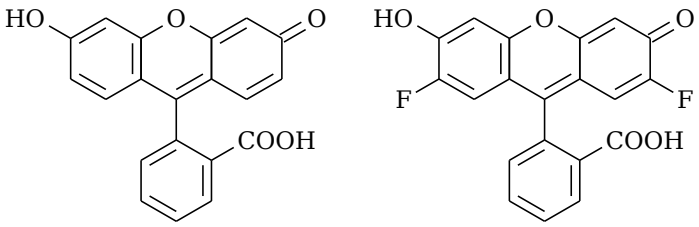

Fluorescein Oregon Green™ 488

Figure 2.1. The structures of fluorescein and Oregon Green™ 488 (2',7'-difluorofluorescein) are shown. Due to the fluorination, Oregon Green 488 has lower pKa's than fluorescein making it useful as a pH sensor only at lower pH.

2.3 Fluorescence Measurement of pH

To measure pH of emulsions the pH-sensitive fluorescent dyes fluorescein and Oregon Green™ 488 (2',7'-difluorofluorescein) were used. These dyes each have four prototropic forms with three equilibrium constants thus their equilibrium can be described by the following set of equations

$$\mathrm{H_3Flu^+} \overset{K_{a1}}{\rightleftharpoons} \mathrm{H^+ + H_2Flu} \tag{2.20a}$$

$$\mathrm{H_2Flu} \overset{K_{a2}}{\rightleftharpoons} \mathrm{H^+ + HFlu^-} \tag{2.20b}$$

$$\mathrm{HFlu^-} \overset{K_{a3}}{\rightleftharpoons} \mathrm{H^+ + Flu^{2-}} \tag{2.20c}$$

where Flu represents the dye and can be either fluorescein or Oregon Green 488. It is due to the differences in the absorptive and fluorescent properties of the prototropic forms that these dyes are good pH sensors. In their neutral forms these dyes are known to have three isomers: quinonoid, lactone, and zwitterion. The structures of these two dyes in their neutral quinonoid states are shown in fig. 2.1 and their prototropic forms are shown in fig. 2.2 [44, 45]. The emission spectra of these dyes with a fixed excitation wavelength are shown in fig. 2.3. From these spectra many pairs of wavelengths could be chosen such that the intensity of one of the wavelengths changes much more than—or in the opposite direction of—the other wavelength as a function of pH. Thus it is possible to construct a ratio from such a pair that is highly sensitive to

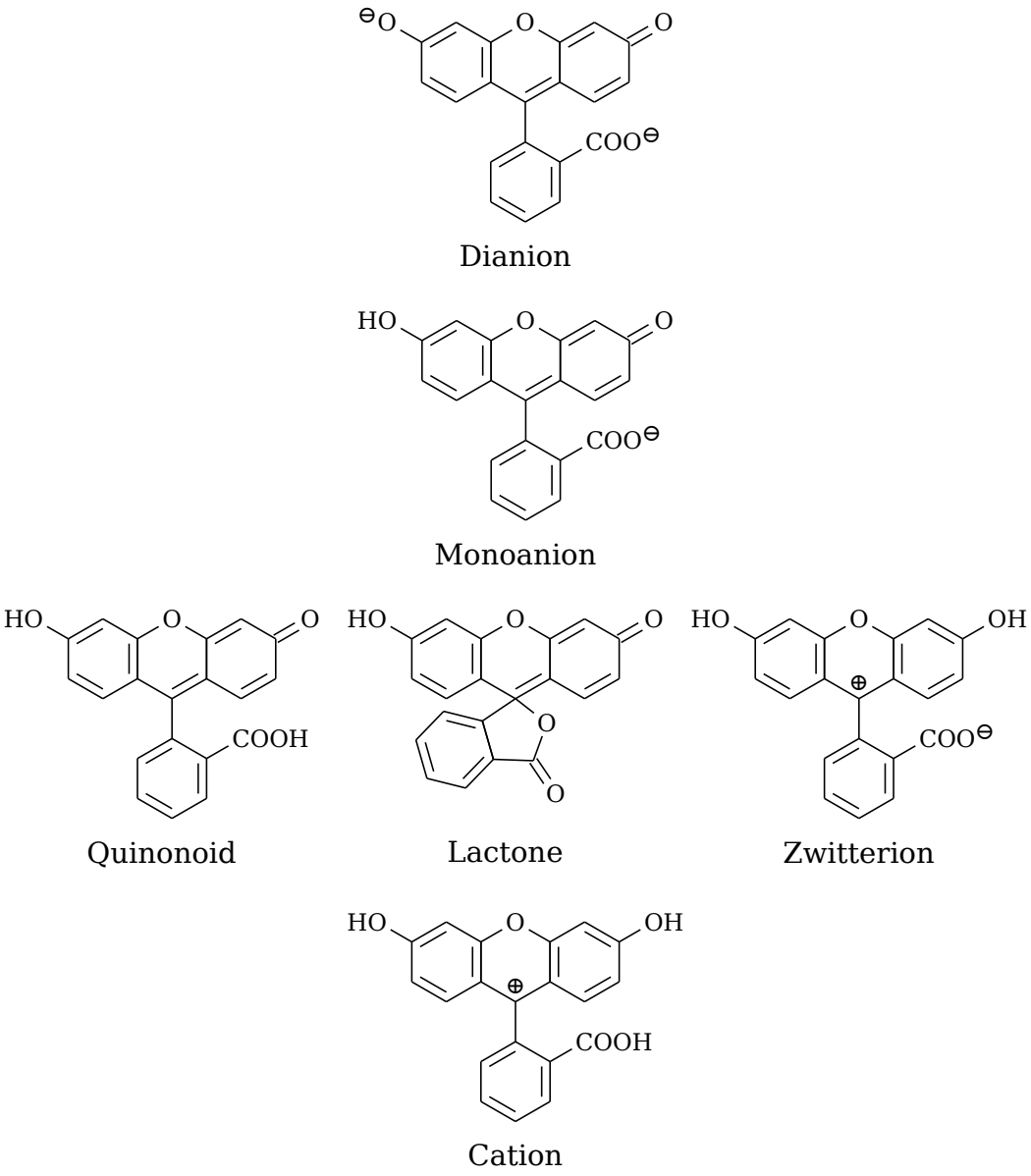

Figure 2.2. The commonly accepted four different prototropic forms of fluorescein including the three different neutral tautomers. It is assumed [45] that the fluorination in Oregon Green 488 does not change the acid–base groups available in fluorescein thus Oregon Green 488 likely shares all the same forms with the only difference being the two fluorine atoms, see fig. 2.1. Not shown is a possible lactone tautomer of the monoanion [46].

changes in pH. Additionally a ratio would be a more robust indicator of pH than the absolute intensity of a single wavelength since it is insensitive to many factors that could affect absolute intensity such as dye concentration, excitation irradiance, collection efficiency, and dye photobleaching. The ratio used in this work is

$$R = \frac{I_0 - I_1}{I_0 + I_1}, \tag{2.21}$$

where I_0 and I_1 are the intensities in channels 0 and 1 respectively. The channel centers and widths need to be chosen to maximize the dynamic range of the ratio within the constraints imposed by the experimental conditions and the measurement apparatus as will be described in later sections.

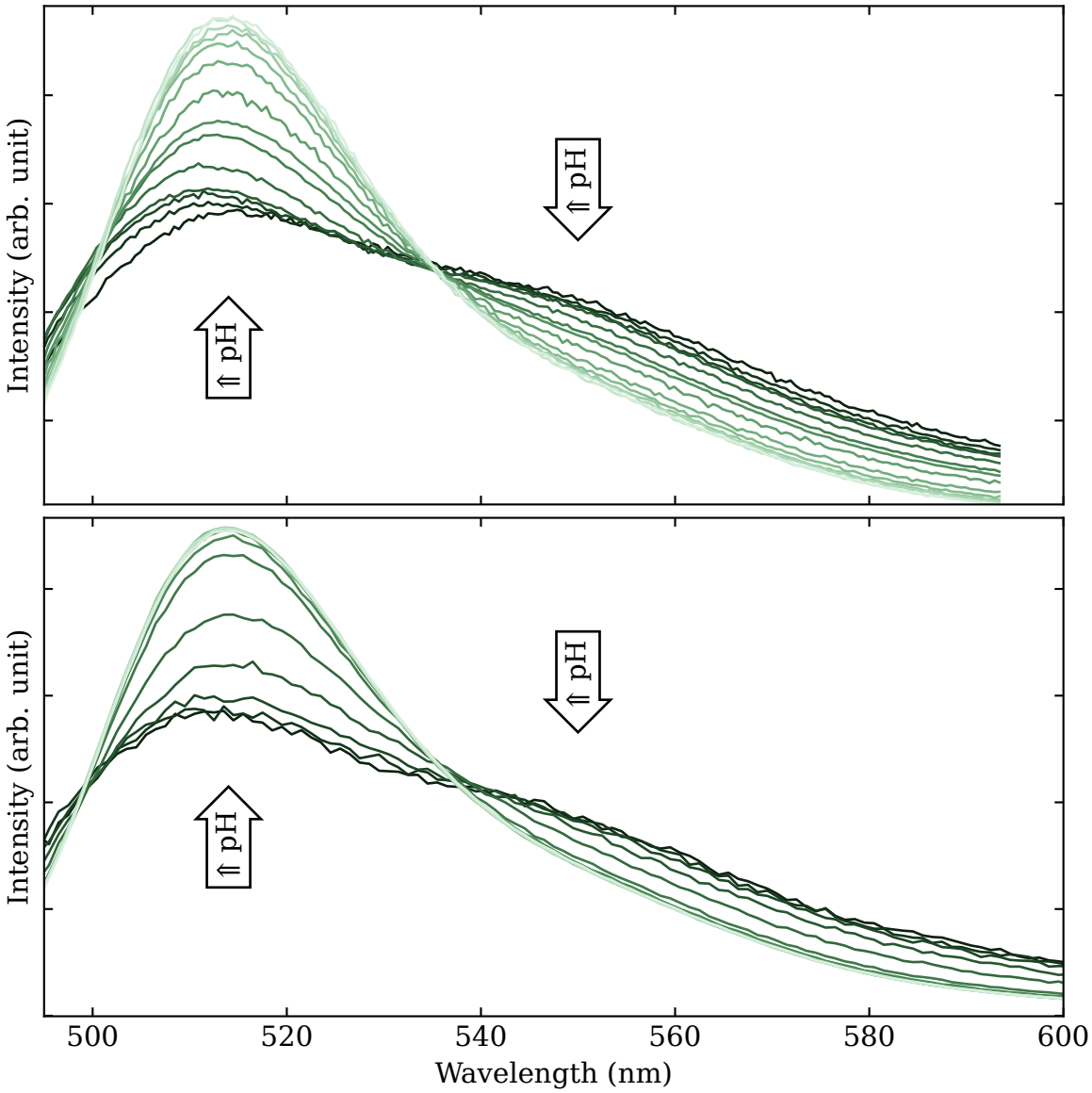

Figure 2.3. Emission spectra for fluorescein (top, $\lambda_{ex} = 460\,nm$) and Oregon Green 488 (bottom, $\lambda_{ex} = 488\,nm$) recorded in buffers with varying pH. Fluorescein pH are, from dark to bright, 2.41, 3.47, 4.07, 4.57, 5.24, 5.59, 5.79, 6.0, 6.36, 6.61, 6.88, 7.15, 7.57, and 8.45. Oregon Green 488 pH are, from dark to bright, 1.54, 2.11, 2.7, 3.24, 3.84, 4.53, 4.97, 5.45, 6.01, 6.56, 7.12, 7.81, 8.35, 8.62, and 9.41. The absolute intensity decreases with decreasing pH giving rise to the relatively larger noise for low pH curves.

CHAPTER 3

ENSEMBLE DROPLET pH MEASUREMENTS

3.1 Setup

Ensemble droplet pH measurements were carried out on a modified PTI QuantaMaster 8000 series fluorimeter which was equipped a xenon short-arc lamp, two Czerny–Turner [47] monochromators (one excitation, one emission) with about 0.5 nm resolution, and a Hamamatsu R928 photomultiplier tube. Additional I modified the fluorimeter by adding an external Hamamatsu C6465 photon counting unit and bypassing the built-in unit which increased the measured countrate linearity up to 1 MHz. To account for pulse-pile the acquisition software, PTI FelixGX, normally applies a correction; however, I could not use this correction since I was unaware of the details of its implementation. Since there was no option to disable the correction applied by FelixGX I set its correction factor, which I will call $\tilde{\tau}$, to the minimum allowable value of 1 thus minimizing its effect on the raw data.

To fully recover the raw data I applied an "un-correction" to remove the incorrect correction applied by the PTI FelixGX software followed by a correction appropriate for the C6465. Using a function generator to drive the data acquisition hardware with known countrates I determined the appropriate form for the "un-correction" function was

$$M = \frac{\tilde{N}}{1 + \alpha \tilde{\tau} \tilde{N}} \tag{3.1}$$

where M is the raw measured—but not reported by the software—countrate, $\tilde{N}$ is the countrate reported by the software, and $\alpha = 5 \times 10^{-10}$. Then, for

sample data, the measured values for M were used to calculate the pulse pile-up corrected countrate, N, using

$$N = \frac{M}{1 - M\tau} \tag{3.2}$$

where τ is the pulse pair resolution and N is the intensity used to calculate the fluorescein emission ratio in eq. (2.21). To estimate the pulse pair resolution I measured the average fluorescein emission ratio in buffer at pH = 9 while modulating the excitation power using neutral density filters or a slider that changes the height of the excitation monochromator exit slit. Then I could identify the proper value of τ by adjusting its value such that the ratio was constant from low to high countrates as the excitation power was modulated all while ensuring the fluorescein emission was linear and not self-quenched. This analysis resulted in $\tau = 87\,\text{ns}$ which is close to the typical value (60 ns) for the C6465 as reported by the manufacturer specification sheet. Equations (3.1) and (3.2) were applied in post-processing. With the C6465 installed and the measured value for τ, the fluorimeter had a maximum usable countrate of about 11.5 MHz, though, for all sample measurements the countrate was kept below 20 % of the maximum by adjusting the excitation power using neutral density filters.

For all measurements the fluorimeter was configured to acquire an emission ratio scan. In this mode the fluorimeter uses a fixed excitation wavelength and alternates between measuring two different emission wavelengths. The excitation wavelength was configured for 460 nm, an isosbestic point of fluorescein, with the spectral width of 3 nm corresponding to opening the slits 1.5 turns. The emission wavelengths were configured for 514 nm and 550 nm with a spectral width of 4 nm corresponding to opening the slits 2 turns. Due to a miscalibration of the emission monochromator there was a +3.4 nm shift such that the true emission wavelengths were 517.4 nm and 553.4 nm. This +3.4 nm shift was calculated as the difference between the specified emission

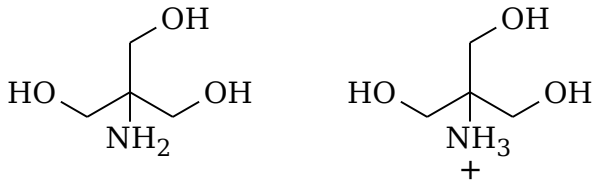

Tris Base Tris Conjugate Acid

Figure 3.1. The structures of the two prototropic forms of tris(hydroxymethyl)-aminomethane are shown.

maximum reported in the fluorescein certificate of analysis and the estimated average emission maxima from 11 measured spectra with pH greater than 7. The fluorescein used for this determination and for all experiments was purchased from Life Technologies Corporation (now a division of Thermo Fisher Scientific), had catalog number F1300, and lot number 1633674. Additionally I outfitted the fluorimeter with a 460 nm to 490 nm bandpass excitation filter, BP460-490 (from Olympus U-MWB2 fluorescence filter cube, manufacturer unknown), just after the exit slit of the emission monochromator and a 488 nm Semrock RazorEdge long-pass emission filter just before the entrance slit to the emission monochromator.

3.2 Sample Preparation

"Tris" [tris(hydroxymethyl)-aminomethane] was used in all calibration samples as a pH buffer to stabilize pH since it is highly compatible with biologic fluids and a commonly used buffer in the physiologic pH range [48]. The structure of tris is shown in fig. 3.1. Tris has $\mathrm{p}K_a = 8.07$ at 25 °C with a temperature dependence of $\mathrm{d}\mathrm{p}K_a/\mathrm{d}T = -0.028\,\mathrm{K}^{-1}$. The $\mathrm{p}K_a$ was adjusted to the temperature of the experiments 22(1) °C. The samples were prepared with $10\,\mu\mathrm{mol\,L}^{-1}$ fluorescein, $20\,\mathrm{mmol\,L}^{-1}$ Tris and a constant target of $200\,\mathrm{mmol\,L}^{-1}$ ionic strength using NaCl as the inert salt to adjust ionic strength. A list of the sample recipes which were used for fluorimeter calibration are shown in table 3.1. It is apparent from the table that samples with a pH between 3.5 and 6 are missing. This is because tris has a pH equivalence point at about 6 therefore the difference

in the amount of HCl necessary to make samples with a pH between 3.5 and 6 is within the pipetting uncertainty. For this reason additional samples were obtained by addition of minute amounts of concentrated HCl to selected samples from the table as described in the table caption. This addition has the undesired effect of diluting the fluorescein concentration, tris concentration, and ionic strength; however, due to the minuscule additional volume the dilution was not greater than 0.17 %.

The need for constant ionic strength across calibration samples is to ensure that the equilibrium constants [see eqs. (2.12), (2.17) and (2.20)] of fluorescein do not vary with pH. Unfortunately due to an error in the concentration of the HCl stock solution these samples were not at constant ionic strength, but instead ranged from 181 $\mathrm{mmol\,L^{-1}}$ to 199 $\mathrm{mmol\,L^{-1}}$ as indicated in table 3.1. However, the magnitude of this error was reduced since the fluorescein calibration is only sensitive up to a pH of about 8 thus the variation in ionic strength is limited to 181 $\mathrm{mmol\,L^{-1}}$ to 189 $\mathrm{mmol\,L^{-1}}$. Furthermore since sample 5 was used for droplet production and had an ionic strength of 186 $\mathrm{mmol\,L^{-1}}$ the variation in ionic strength relative to this sample was only about $^{-2.7\,\%}_{+1.6\,\%}$. This variation is about the same magnitude of the error inherent in solution preparation via micropipettes and is insignificant compared to the observed data.

For emulsion preparation the aqueous dispersed phase was prepared with either tris buffer or NaOH. Emulsions with tris used sample 5 from table 3.1 which had pH = 7.57 when the emulsions were prepared. Table 3.2 contains a list of all dispersed phase solutions in which NaOH was used; the pH were recorded from a glass electrode meter and the ionic strengths were then calculated from the known NaOH and NaCl concentrations and the measured pH.

Once the samples (calibration or emulsion) were prepared they were loaded into a Starna Scientific® 16.100F-Q-10/Z15 quartz cuvette and then measured. This cuvette nominally holds 100 µL of solution but must be filled with at least 125 µL of aqueous solution or 150 µL of emulsion to prevent the meniscus

Sample	ν_{Flu} µL	$\nu_{\mathrm{H_2O}}$ µL	ν_{HCl} µL	ν_{NaCl} µL	ν_{Tris} µL	pH	I mol L^{-1}
0	400	1998	10	792	800	9.53	0.199
1	400	1992	30	778	800	9.08	0.197
2	400	1975	80	745	800	8.54	0.194
3	400	1956	140	704	800	8.07	0.189
4	400	1950	160	690	800	7.85	0.187
5	400	1944	180	676	800	7.60	0.186
6	400	1940	195	665	800	7.33	0.184
7	400	1938	200	662	800	7.22	0.184
8	400	1938	201	661	800	7.19	0.184
9	400	1937	202	661	800	7.15	0.184
10	400	1937	203	660	800	7.11	0.184
11	400	1937	204	659	800	6.96	0.184
12	400	1936	205	659	800	6.88	0.184
13	400	1936	206	658	800	6.90	0.184
14	400	1936	207	657	800	6.78	0.184
15	400	1935	208	657	800	6.73	0.184
16	400	1935	209	656	800	6.65	0.183
17	400	1935	210	655	800	6.61	0.183
18	400	1934	211	655	800	6.43	0.183
19	400	1934	212	654	800	5.95	0.183
20	400	1934	213	653	800	6.06	0.183
21	400	1932	216	652	800	3.47	0.183
22	400	1932	218	650	800	3.28	0.183
23	400	1929	225	646	800	2.98	0.183
24	400	1927	230	643	800	2.84	0.182
25	400	1915	260	625	800	2.41	0.181

Table 3.1. Recipes used to make calibration samples for measurement of pH through measurement of the fluorescein fluorescence emission ratio. All solutions contained 10 µmol L^{-1} fluorescein and 20 mmol L^{-1} tris buffer at the measured pH in a total volume of 4 mL. The ionic strengths, I, were calculated using the model described in section 2.1.4. The stock solutions used were 100 µmol L^{-1} fluorescein, 372 mmol L^{-1} HCl, 1 mol L^{-1} NaCl, and 100 mmol L^{-1} tris. Samples 18, 19, and 20 were used to fill the gaps in pH by addition of minute amounts of concentrated HCl with no more than 0.17 % dilution of other components. Using sample 18 additional samples with pH of 6.36, 6.29, 6.17, 5.99, 5.79, 5.16, 4.73, 4.57, 4.43, 4.23, 4.01, and 3.61 were obtained. Using sample 19 additional samples with pH of 5.74, 5.59, 5.06, 4.45, 4.07, and 3.85 were obtained. Using sample 20 additional samples with pH of 5.98, 5.69, 5.53, 5.45, 5.37, and 5.24 were obtained. Therefore in total there were 50 samples, all of which were used in the fluorimeter calibration. For droplet data, sample 5 was used.

C_{NaOH} mmol L^{-1}	C_{NaCl} mmol L^{-1}	pH	I mmol L^{-1}
0.000	200.0	7.41	200
0.001	200.0	7.75	200
0.010	200.0	8.01	200
0.030	200.0	8.10	200
0.100	200.0	8.60	200
0.300	200.0	9.74	200
1.000	199.5	10.61	200
3.000	198.5	11.28	201
5.000	197.5	11.58	202
7.500	196.0	11.80	203
10.000	195.0	11.80	203
15.000	192.5	12.09	206
30.000	185.0	12.29	210
75.000	162.5	12.67	225
100.000	105.0	12.87	194
125.000	85.0	12.95	194
150.000	65.0	13.07	202
200.000	30.0	13.11	197

Table 3.2. Table of NaOH solutions used for making emulsions. Additionally all solutions contained 10 µmol L^{-1} fluorescein. The goal was to obtain solutions at constant 200 mmol L^{-1} ionic strength and the target final concentrations of NaOH and NaCl in the solutions are given. The pH reported are as measured by a glass electrode and the ionic strength was calculated using the other three columns from the model described in section 2.1.4.

from appearing in the window. Between samples the cuvette was washed with deionized water and spectrophotometric grade methanol. It is important to take all measurements in the same cuvette or a matched set due to differences in the transmission spectra of the cuvette material.

In the ratio measurements each wavelength was integrated for 1 s, there was about 0.32 s delay between wavelengths and 3.23 s between samples thus the fluorimeter sample rate was about 18.6 min^{-1}. Since the intensity for both wavelengths were stable there is no issue with the slight delay between sampling each emission channel and the measured ratios were normally distributed where the standard deviation of each sample was between 0.2 % to 1.2 % of the sample mean.

3.3 Calibration

As discussed in section 2.3, the fluorescein emission ratio [see eq. (2.21)] can be used to measure pH. However, first it is necessary to obtain a calibration curve from samples with known pH. The range of pH values must span the region where measurements will be taken but ideally should cover all pH where the fluorescein emission ratio is sensitive. After calibration the pH of emulsion droplets can be determined using the same fluorescent pH sensor and same instrument.

From the 50 samples listed in table 3.1 I obtained the calibration curve shown in fig. 3.2. For the emission ratio, eq. (2.21), the emission wavelengths, I_0 and I_1, were respectively 517.4 nm and 553.4 nm. For each sample the ratio was measured for 5 min total giving 93 estimates of the ratio therefore in the figure the mean ratios are shown while their uncertainties (standard deviation of the 93 measurements) are smaller than the symbol size and so are not shown. A table of the calibration data is given in table 3.3.

Before measuring the fluorescein ratio in droplets its necessary to invert the calibration curve. It is tempting to invert the curve using a spline interpolation;

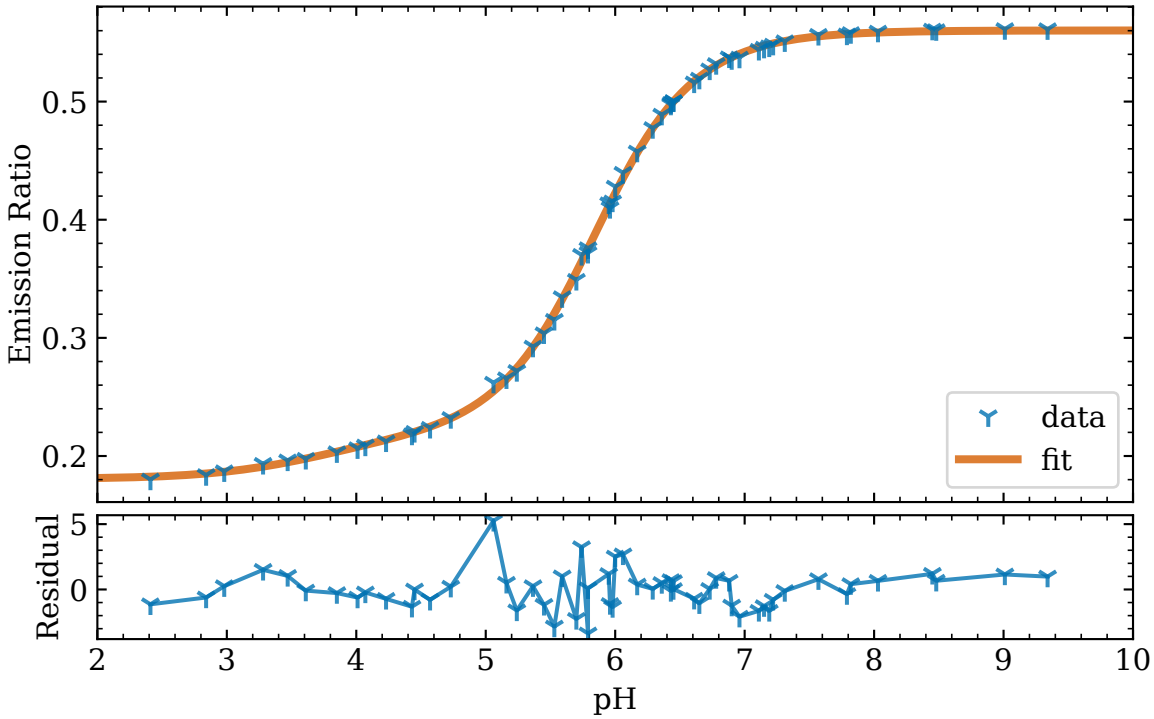

Figure 3.2. Calibration curve for fluorescein in the fluorimeter is shown in the upper plot along with a non-linear least squares fit to eq. (3.5). The fit had a reduced χ^2 of 2.34 and the standardized fit residuals are shown in the lower plot. The uncertainty on the data are within the points and the residuals are standardized by these uncertainties.

pH	R	σ_R	pH	R	σ_R
2.41	0.1801	0.0021	6.06	0.4398	0.0017
2.84	0.1839	0.0021	6.17	0.4577	0.0024
2.98	0.1871	0.0019	6.29	0.4776	0.0021
3.28	0.1934	0.0016	6.36	0.4889	0.0016
3.47	0.1963	0.0015	6.43	0.4987	0.0016
3.61	0.1976	0.0021	6.43	0.4974	0.0015
3.85	0.2032	0.0015	6.45	0.5004	0.0005
4.01	0.2066	0.0018	6.45	0.5002	0.0016
4.07	0.2089	0.0018	6.61	0.5162	0.0015
4.23	0.2124	0.0018	6.65	0.5194	0.0014
4.43	0.2182	0.0012	6.73	0.5272	0.0016
4.45	0.2204	0.0012	6.78	0.5318	0.0014
4.57	0.2239	0.0012	6.88	0.5374	0.0014
4.73	0.2322	0.0009	6.90	0.5359	0.0013
5.06	0.2621	0.0014	6.96	0.5372	0.0015
5.16	0.2658	0.0015	7.11	0.5438	0.0014
5.24	0.2720	0.0016	7.15	0.5456	0.0013
5.37	0.2926	0.0018	7.19	0.5467	0.0010
5.45	0.3039	0.0019	7.22	0.5482	0.0013
5.53	0.3152	0.0019	7.31	0.5511	0.0013
5.59	0.3344	0.0019	7.57	0.5565	0.0016
5.70	0.3491	0.0029	7.79	0.5568	0.0012
5.74	0.3702	0.0018	7.82	0.5580	0.0014
5.79	0.3720	0.0011	8.03	0.5592	0.0011
5.79	0.3759	0.0026	8.45	0.5609	0.0011
5.95	0.4139	0.0020	8.48	0.5605	0.0013
5.96	0.4100	0.0034	9.01	0.5614	0.0012
5.98	0.4154	0.0020	9.34	0.5613	0.0012
6.00	0.4280	0.0022			

Table 3.3. Data for fluorescein calibration curve shown in fig. 3.2. In each row the pH, ratio, and uncertainty on the ratio are given for two different samples separated by the double vertical line. For each sample there were 93 measurements of the fluorescein emission ratio [see eq. (2.21)]. Reported are the mean of these measurements, R, and the standard deviation, σ_R.

however, this has the disadvantage of not providing a meaningful uncertainty on the measurement of pH. For a reliable estimate of uncertainty in the analysis presented a meaningful model for this calibration curve is necessary. By fitting the model to the data, I obtain uncertainties in the fit parameters that are useful in estimating the uncertainty in the pH. For this reason I use the model for fluorescein pH sensitivity presented in chapter 2.

To account for the pH response of fluorescein the model should depend on the concentrations of the prototropic forms which themselves depend on pH. From the fluorescein equilibria presented in eqs. (2.20a) to (2.20c) I derive the following equations,

$$K_{a1} = \frac{a_{\mathrm{H^+}} c_{\mathrm{H_2Flu}}}{c_{\mathrm{H_3Flu^+}}} \tag{3.3a}$$

$$K_{a2} = \frac{a_{\mathrm{H^+}} c_{\mathrm{HFlu^-}}}{c_{\mathrm{H_2Flu}}} \tag{3.3b}$$

$$K_{a3} = \frac{a_{\mathrm{H^+}} c_{\mathrm{Flu^{2-}}}}{c_{\mathrm{HFlu^-}}}, \tag{3.3c}$$

where K_{ai} is the effective equilibrium constant of the ith ionization at the ionic strength and temperature of the measurement and $a_{\mathrm{H^+}} = 10^{-\mathrm{pH}}$ is calculated from the measured sample pH. The total concentration of fluorescein is a constant and equal to the sum of the concentrations of the four prototropic forms, $C_{\mathrm{Flu}} = c_{\mathrm{H_3Flu^+}} + c_{\mathrm{H_2Flu}} + c_{\mathrm{HFlu^-}} + c_{\mathrm{Flu^{2-}}}$, which when combined with eqs. (3.3a) to (3.3c) gives the concentrations of the prototropic forms as functions of known quantities:

$$C_{\mathrm{Flu}} = \text{Total concentration of fluorescein } (10\,\mu\mathrm{mol\,L^{-1}}) \tag{3.4a}$$

$$c_{\mathrm{H_3Flu^+}} = C_{\mathrm{Flu}} \left(1 + \frac{K_{a1}}{a_{\mathrm{H^+}}} + \frac{K_{a1}K_{a2}}{{a_{\mathrm{H^+}}}^2} + \frac{K_{a1}K_{a2}K_{a3}}{{a_{\mathrm{H^+}}}^3} \right)^{-1} \tag{3.4b}$$

$$c_{\mathrm{H_2Flu}} = C_{\mathrm{Flu}} \left(\frac{a_{\mathrm{H^+}}}{K_{a1}} + 1 + \frac{K_{a2}}{a_{\mathrm{H^+}}} + \frac{K_{a2}K_{a3}}{{a_{\mathrm{H^+}}}^2} \right)^{-1} \tag{3.4c}$$

$$c_{\mathrm{HFlu^-}} = C_{\mathrm{Flu}} \left(\frac{{a_{\mathrm{H^+}}}^2}{K_{a1}K_{a2}} + \frac{a_{\mathrm{H^+}}}{K_{a2}} + 1 + \frac{K_{a3}}{a_{\mathrm{H^+}}} \right)^{-1} \tag{3.4d}$$

$$c_{\mathrm{Flu^{2-}}} = C_{\mathrm{Flu}} \left(\frac{{a_{\mathrm{H^+}}}^3}{K_{a1}K_{a2}K_{a3}} + \frac{{a_{\mathrm{H^+}}}^2}{K_{a2}K_{a3}} + \frac{a_{\mathrm{H^+}}}{K_{a3}} + 1 \right)^{-1}. \tag{3.4e}$$

Then the fit function is

$$R = m(\mathrm{pH}|\boldsymbol{\theta}) \equiv F_1 c_{\mathrm{H_3Flu^+}} + F_2 c_{\mathrm{H_2Flu}} + F_3 c_{\mathrm{HFlu^-}} + F_4 c_{\mathrm{Flu^{2-}}}, \tag{3.5}$$

where $\boldsymbol{\theta}$ represents all the fit parameters: four proportionality constants F_1, F_2, F_3, and F_4, and the three equilibrium constants. Note that C_{Flu} can be absorbed into the proportionality constants. The resulting non-linear least squares fit is shown in fig. 3.2. The reduced χ^2 of this fit was 2.34 and the standardized residuals are shown below the calibration curve. This model was the same as used by Smith and Pretorius [44] in their analysis of fluorescein absorbance.

The result of the fit gives $\mathrm{p}K_{a1} = 3.682(165)$, $\mathrm{p}K_{a2} = 5.648(83)$, and $\mathrm{p}K_{a3} = 6.017(103)$ where $\mathrm{p}K_{ai} = 10^{-K_{ai}}$ while the values reported by Smith and Pretorius [44] adjusted to 186 $\mathrm{mmol\,L^{-1}}$ ionic strength were $\mathrm{p}K_{a1} = 2.34(15)$, $\mathrm{p}K_{a2} = 4.32(10)$, and $\mathrm{p}K_{a3} = 6.31(5)$. A possible reason for the discrepancies in the $\mathrm{p}K_a$'s is that the fluorescence of fluorescein is more complicated than absorptivity due to excited state proton transfers which result in different $\mathrm{p}K_a$'s for the excited states [45, 49–51].

Although the $\mathrm{p}K_a$'s from my fit do not agree with the previously reported values, the fit model well approximates the data and has the expected behavior both above and below the range of the calibration data. It is also likely that

any similar fit with 7 parameters would also yield similar results due to high parameter correlations. Attempts at fixing the pK_a's to those values reported in the literature for reducing the number of fit parameters failed to produce a good fit. For these reasons I can reasonably expect this model to obtain meaningful uncertainties in measured pH. However, to be certain I have also explored other models to fit the data.

A generalized logistic function does not properly account for decreasing ratio when pH is less than 5 since the generalized logistic function predicts a constant ratio in this region. In Sjöback et al. [49] a complete fluorescence model of fluorescein is presented that is purportedly able to estimate the emission intensity given any combination of excitation and emission wavelength, pH, ionic strength, and temperature. Thus Sjöback et al.'s model should, in theory, be able to fully predict my calibration curve by calculating the emission ratio [see eq. (2.21)] at the approximate ionic strength of my calibration curve, $186\,\mathrm{mmol\,L^{-1}}$, as a function of pH. However, it fails to do so for two reasons: Sjöback et al.'s model prediction is translated upwards in comparison to the data in fig. 3.2 by about 0.05 units and similar to the failure of the generalized logistic function, Sjöback et al.'s model predicts a constant ratio for pH less than about 5.

Two other other models I evaluated include

$$m(\mathrm{pH}|\boldsymbol{\theta}) = \frac{A}{B} \quad \text{and} \quad m(\mathrm{pH}|\boldsymbol{\theta}) = \frac{A-B}{A+B}$$

with

$$A = F_1 c_{\mathrm{H_3Flu^+}} + F_2 c_{\mathrm{H_2Flu}} + F_3 c_{\mathrm{HFlu^-}} + c_{\mathrm{Flu^{2-}}}$$
$$B = G_1 c_{\mathrm{H_3Flu^+}} + G_2 c_{\mathrm{H_2Flu}} + G_3 c_{\mathrm{HFlu^-}} + G_4 c_{\mathrm{Flu^{2-}}}.$$

In these models F_i and G_i are proportional to the molar absorptivities, quantum yields, and relative emission intensities at 514 nm and 550 nm respectively. Note

that one constant, F_4, can be dropped due to the ratio. Due to the increased number of model parameters I fixed the pK_a's to their expected values at 186 mmol L^{-1} ionic strength using the excited state values reported by Sjöback et al. [49]. Fits of the calibration data in fig. 3.2 with these two models resulted in identical residuals and reduced χ^2's as the model I first discussed in eq. (3.5); however, in these models the proportionality constants F_i and G_i were not as expected since they incorrectly predict that the more protonated prototropic forms are brighter than the deprotonated forms.

Since all the models resulted in the same fit and the latter models have higher complexity I decided to use the simpler model from eq. (3.5). However, since the latter models do not have the expected trend in the proportionality constants and the model proposed by Sjöback et al. [49] does not predict the decreasing ratio when pH is less than 5 there is evidence that the currently accepted model of fluorescein is incomplete.

3.3.1 Dependence on Buffer Species, Fluorescein Concentration, and Ionic Strength

I also measured the dependence of the fluorescein emission ratio on some other parameters. From previous attempts at obtaining a calibration curve I determined that there is no change in the emission ratio with the buffer species citrate, PIPES, HEPES, tris, phosphate, and ethanolamine at up to 50 mmol L^{-1} concentration. However, the emission ratio is dependent on the concentration of fluorescein (see fig. 3.3) and also the ionic strength (see fig. 3.4). The fluorescein concentration dependence was only measured at pH = 9. It is shown that within a factor of two of the calibration concentration, which was 10 µmol L^{-1}, there was only a change of about 0.5 %; however, I expect the dependence to be slightly larger at lower pH. The ionic strength dependence was most pronounced at pH = 6, which is within the most sensitive region of the calibration (5 < pH < 7), yet in all cases there was little to no change in the emission ratio within ±50 % of the ionic strength of the calibration.

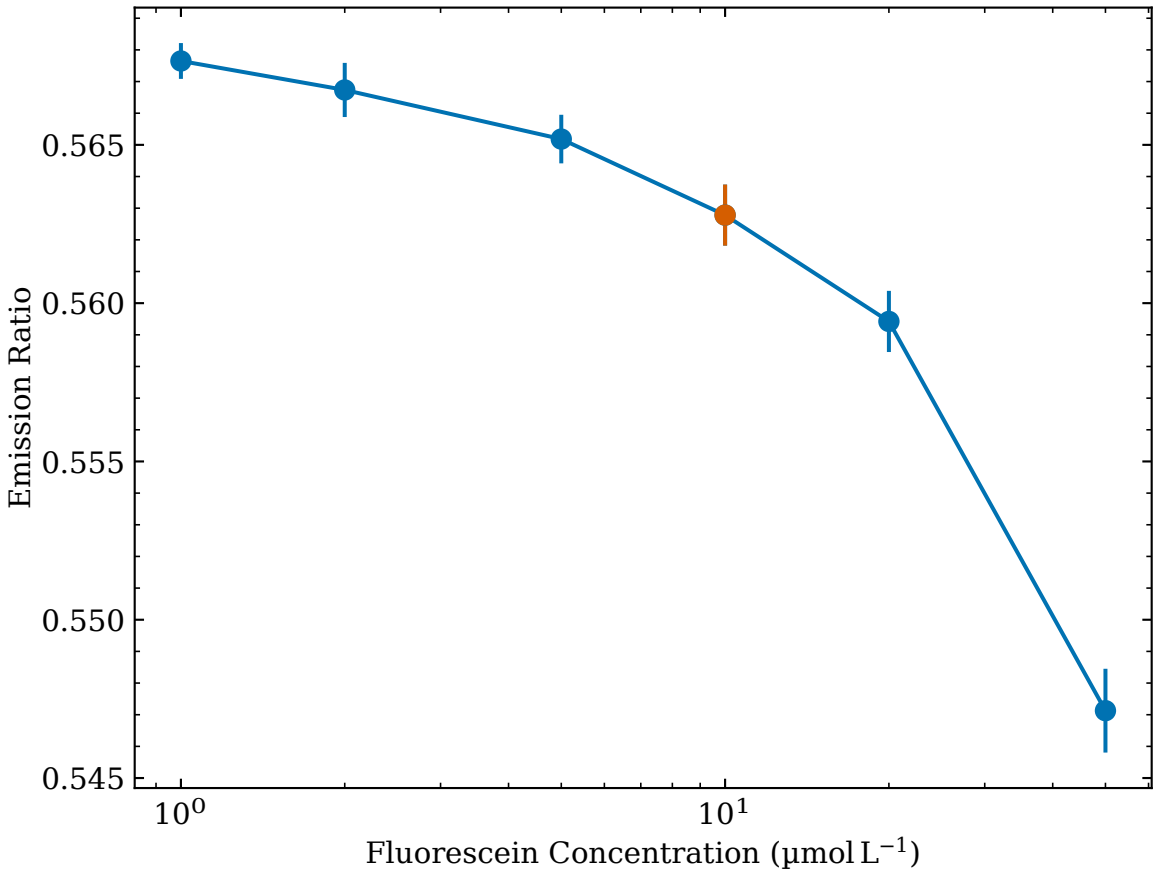

Figure 3.3. The dependence of the fluorescein emission ratio as a function of fluorescein concentration at pH = 9 and 200 mmol L^{-1} ionic strength. At pH = 9 only the dianion of fluorescein is present in solution. The concentration of fluorescein during calibration was 10 µmol L^{-1}.

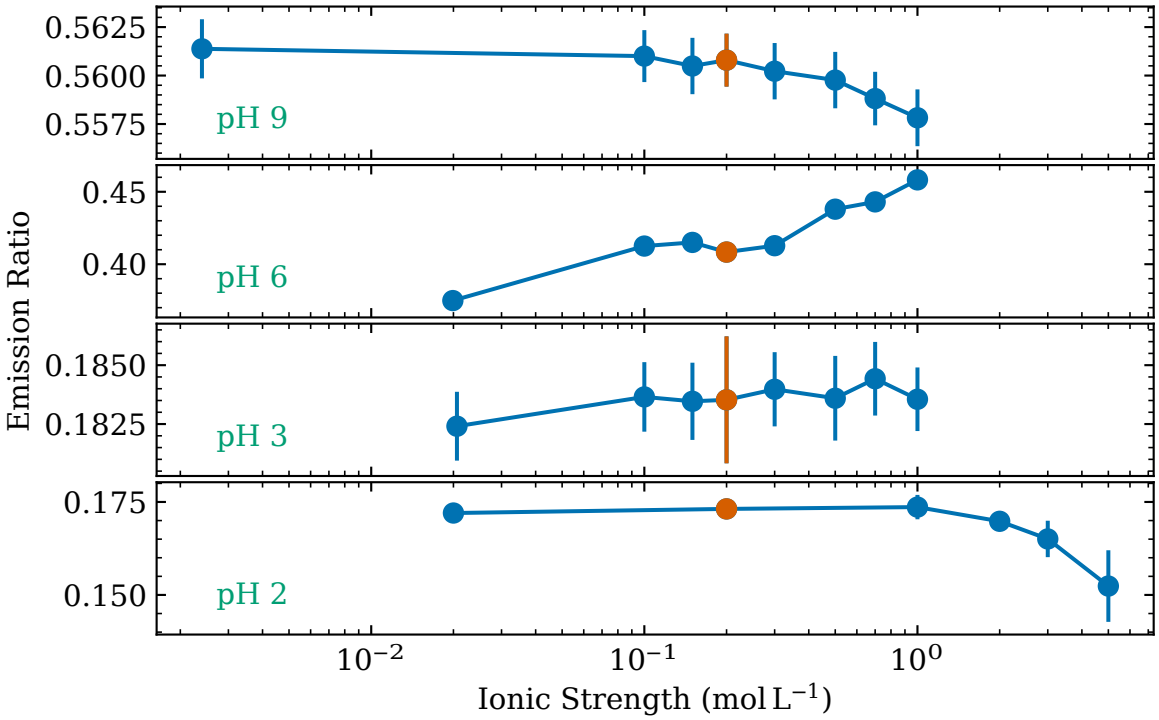

Figure 3.4. The dependence of the fluorescein emission ratio as a function of solution ionic strength is shown for pH = 2, 3, 6, and 9. Note that the data points and error bars indicate the means and standard deviations of 93 measurements of the ratio for each sample. Where error bars are not visible they are smaller than the data points. The ionic strength during calibration was 0.2 mol L^{-1}.

3.4 Droplet Data: Ratio

Emulsions were prepared in an 0.6 mL microcentrifuge tube using a Branson Bransonic 1510R-DTH ultrasonic cleaner which operates at 42 kHz. A custom designed holder held the tube at the top surface of the water bath such that the level of the fluid in the tube was just below the level of the bath water. The bath water contained 10 g L^{-1} Fisherbrand™ Sparkleen™ 1* to reduce the surface tension of the water which effectively increases the transfer of ultrasonic energy to the tube and emulsion. To make an emulsion 200 µL to 300 µL of FC-40 (possibly containing surfactant) was added to the tube then a 1 µL to 6 µL drop of sample (see table 3.1, sample 5) was dispersed into the FC-40 with the sample:FC-40 ratio set to 1:100 or 1:200. Since FC-40 is more dense than water the sample droplet floats and upon ultrasonication can splash onto the upper sidewalls or lid of the tube. The splashed sample would usually not become emulsified thus the sample:FC-40 ratio is not a well defined parameter for this method as it varies from emulsion to emulsion.

Once prepared, emulsions were pipetted into the cuvette and then into the fluorimeter within 30 s of preparation. The emission ratio was then measured for a duration of either 10 min or 30 min which gave 160 or 400 ratios. Since most measurements were stable over time, only the average ratios and their standard deviations are reported.

The average radius of droplets prepared in this method varies from sample to sample, but are approximately 112.7 nm as measured by Milas [52, p. 35] using dynamic light scattering or 126.4 nm as measured by Milas [52, p. 36] using Mie scattering theory to fit UV/Vis absorption data. Since the excitation volume of the fluorimeter is about 1 mm^3 there are approximately 1.5 billion droplets in the focal volume. Therefore this method is an ensemble measurement.

*Fisherbrand™ Sparkleen™ 1 contains 10 % to 50 % sodium tripolyphosphate, 10 % to 25 % sodium dodecylbenzenesulfonate, and 1 % to 10 % nonionic detergent

For ensemble droplet measurements two different series were obtained. In the first series the continuous phase was neat (without surfactant) FC-40 while the dispersed phase contained fluorescein, varying NaOH concentrations, and varying NaCl concentrations with a constant ionic strength of 200 $\mathrm{mmol\,L^{-1}}$. Since the amount of NaOH varied in this series the initial sample pH also varied [see table 3.2]. In the second series the continuous phase was FC-40 with varying amounts of surfactant from 0 wt% to 10 wt% while the dispersed phase was sample 5 from table 3.1; however, the sample pH was shifted to 7.57 from its initial value, 7.60.

The ensemble droplet measurement results for the two series are shown in figs. 3.5 and 3.6. It is shown that for droplets with little sodium hydroxide or surfactant the emission ratio is very low indicating a pH in droplets lower than the pH of the sample from which the emulsions were prepared. When the sodium hydroxide concentration or surfactant concentration are increased there is a concomitant increase in the emission ratio recovering or nearly recovering the expected ratio of the bulk sample.

I also observe that the ratio in droplets is lower than the lowest observed ratio during calibration. In a search of similarly low ratios in bulk sample the only conditions for which I observed lower ratios was by increasing the ionic strength as shown in fig. 3.4(bottom) where at 5 $\mathrm{mol\,L^{-1}}$ ionic strength and pH = 2 the ratio was 0.152(10). This could mean that there is also a higher effective ionic strength in droplets. Indeed such an effects is possible due to Ostwald ripening of the emulsion wherein water is transferred through the continuous phase from small droplets to large droplets which then cream due to their lower density and become removed from the emulsion.

3.5 Bayesian Analysis of Droplet Data

To calculate a pH from ratios in droplets to pH it is necessary to invert the calibration. This can be done using a rule of probability theory called Bayes'

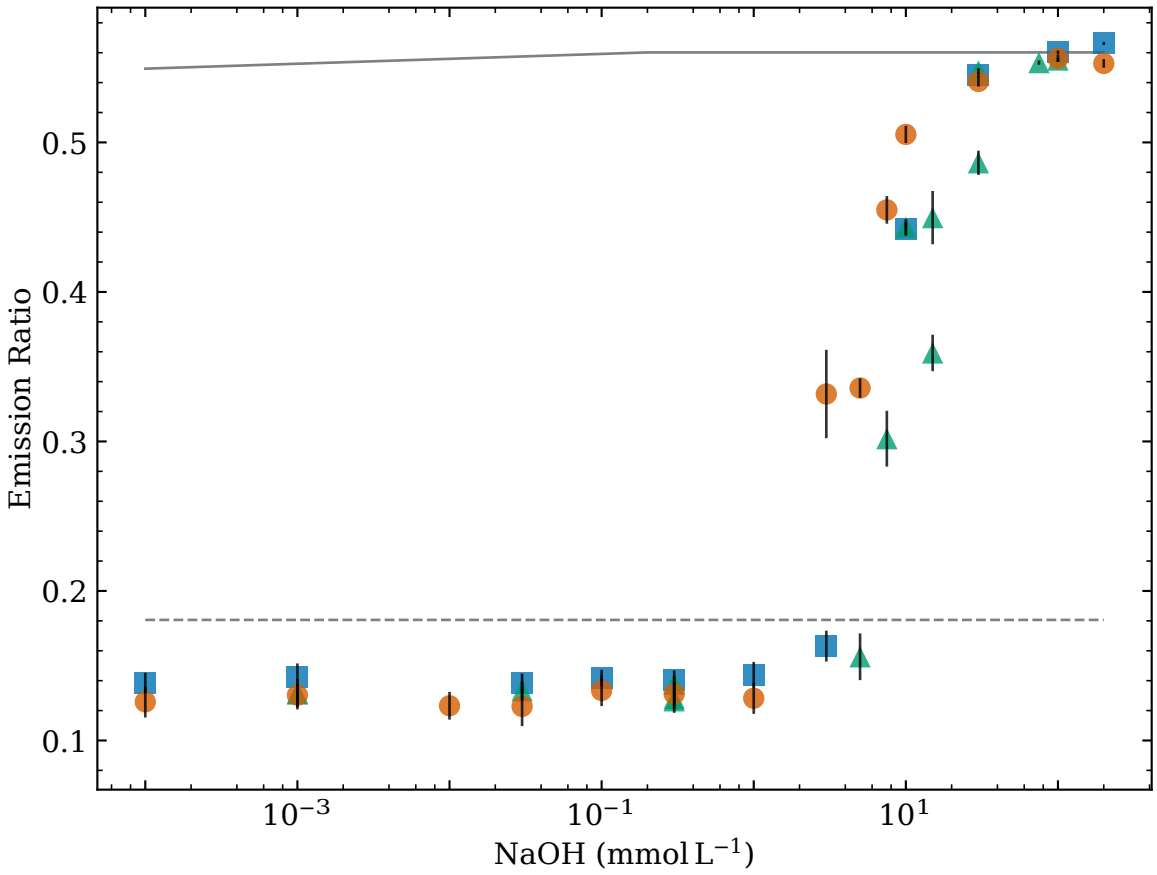

Figure 3.5. Fluorescein emission ratio is shown for droplets made from NaOH solutions and FC-40 without surfactant. All solutions had approximately 200 mmol L^{-1} ionic strength. Three different runs were performed and are shown by different colors and symbols. The gray dashed line indicates the lowest ratio observed in the calibration curve while the solid gray line indicates the expected ratio of the bulk sample.

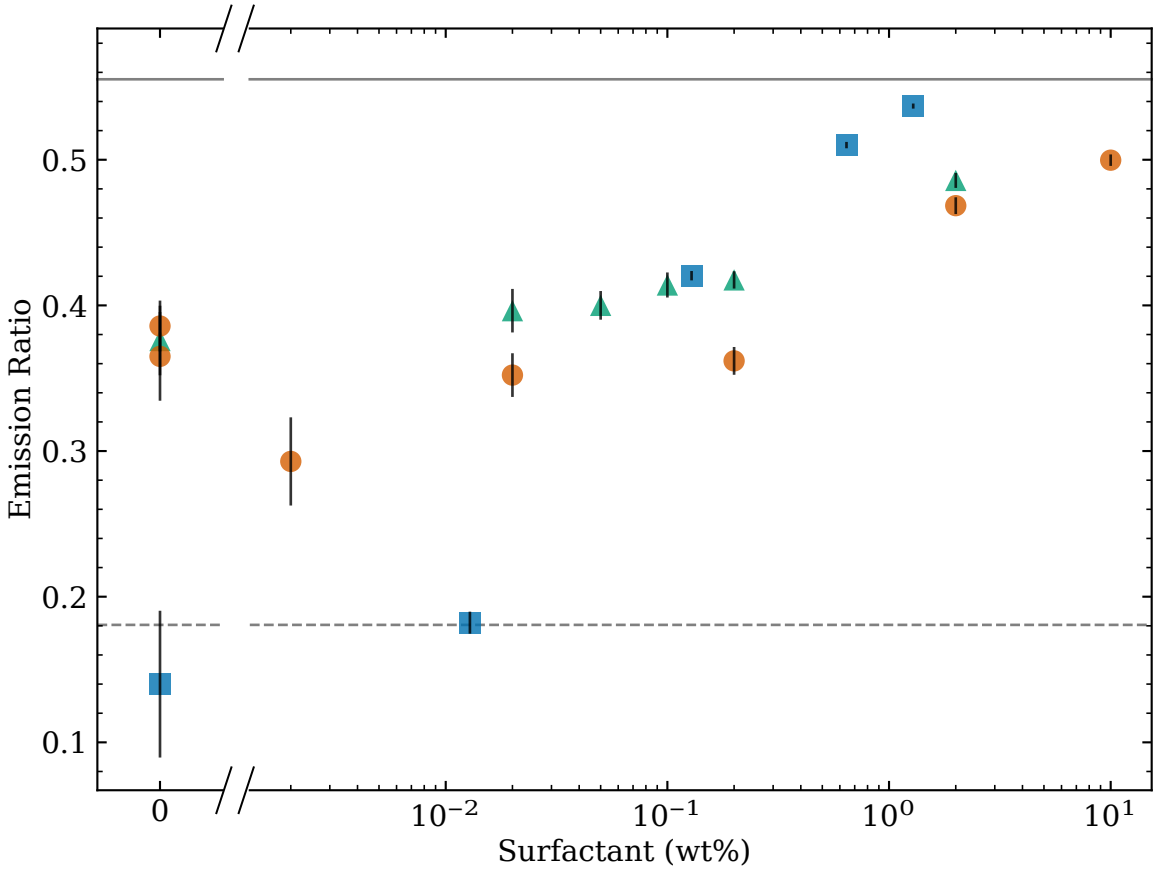

Figure 3.6. Fluorescein emission ratio is shown for droplets made from 20 mmol L^{-1} tris buffer with 186 mmol L^{-1} ionic strength at pH = 7.57 and FC-40 with varying surfactant concentration. Three different runs were performed and are shown by different colors and symbols. The gray dashed line indicates the lowest ratio observed in the calibration curve while the solid gray line indicates the ratio of the bulk sample.

Theorem, but before stating the theorem I will first introduce some definitions. Given two propositions A and B the conditional probability of A being true given that B is true is represented by $p(A|B)$. For example the conditional probability I am trying to find is $p(\text{pH}|R)$: given a measured fluorescein emission ratio, $R = r$, what is the probability that pH = a where a is any real number. The probability that both propositions A and B are true is written as $p(A, B)$ which is also known as the joint probability. If A and B are independent the joint probability is simply the product of the individual probabilities, $p(A, B) = p(A)p(B)$. However, when A and B are dependent this product rule becomes

$$\begin{aligned} p(A, B) &= p(A)p(B|A) \\ &= p(B)p(A|B), \end{aligned} \tag{3.6}$$

where I have written two equivalent ways of representing the joint probability. For the problem at hand, solving for $p(\text{pH}|R)$, it is tempting to stop here and think that the joint probability, $p(\text{pH}, R)$, is simply the calibration curve in fig. 3.2 such that $p(\text{pH}|R) = p(\text{pH}, R)/p(R)$ where $p(R) = \int p(\text{pH}, R)\text{dpH}$. Whereas this would not be incorrect, I will show that by continuing with Bayes' Theorem a more complete result will be obtained.

Bayes' Theorem can be derived by rewriting the right hand side of eq. (3.6):

$$p(A|B) = \frac{p(B|A)p(A)}{p(B)};$$

however, this is usually written as

$$p(H_0|D, I) = \frac{p(D|H_0, I)p(H_0|I)}{p(D|I)} \tag{3.7}$$

where H_0 is a proposition asserting the truth of a hypothesis of interest, I is a proposition representing our prior information, and D is a proposition representing data [53]. Note that the conditional dependence on I was added to all terms thus not changing the equality. $p(D|H_0, I)$ is called the likelihood

function, $\mathcal{L}(H_0)$, and it gives the probability of observing the data, D, given that the propositions H_0 and I are true. $p(H_0|I)$ is called the prior probability density function (PDF) and it estimates the probability density of H_0 before observing any data based on prior information I. The denominator is simply a normalization factor $p(D|I) = \int p(H_0|I)p(D|H_0, I)\mathrm{d}H_0$. Finally $p(H_0|D, I)$ is called the posterior PDF and it gives the probability that the proposition H_0 is true after observing data, D, and based on prior information I. For all these statements the proposition H_0 is an assertion that the true value of H_0 lies in the interval h to $h + \mathrm{d}h$.

To convert ratio to pH it is necessary to calculate the prior PDF, $p(\mathrm{pH}|I)$, and the likelihood function, $p(R|\mathrm{pH}, M, \boldsymbol{\theta}, I)$, where M is the fit model of fluorescein in eq. (3.5), and $\boldsymbol{\theta}$ represents the best fit parameter values. Since this experiment has not been done before there is limited prior information except that we know the resistance of the buffer to changes in pH as given by the buffer capacity in eq. (2.9), and the initial sample pH. First I will calculate the buffer capacity then I will simply state the likelihood function which was derived by Gregory [53, sec. 4.8] and generally applicable to models and data with random normal errors.

When there is little prior information typically one chooses a uniform prior or Jeffrey's prior. The uniform prior gives equal probability in a finite range and zero otherwise. Jeffrey's prior is similar but gives equal probability per decade with more weight for smaller decades. Neither of these priors would be suitable since it is unclear what to use as minimum and maximum values of pH. Now it can be seen that if tempted to calculate $p(\mathrm{pH}|R) = p(\mathrm{pH}, R)/p(R)$ as previously suggested a uniform prior (a constant) would have been assumed since $p(\mathrm{pH}, R) = p(R|\mathrm{pH})p(\mathrm{pH})$ thus $p(\mathrm{pH})$ can only be a constant that is absorbed by the normalization $p(R)$; however, since the constant was not specified any pH would be given a finitely probability even highly improbable values such as -100. Additionally due to the shape of the fluorescein model function this method leads to an infinitely long tail in the posterior PDF if a

ratio is measured at or outside of the bounds of the calibration curve which would make it impossible to define reasonable uncertainties.

Instead of imparting a prior on pH first consider the integration of the buffer capacity,

$$g_{\mathrm{pH}_i}{}^{-1}(y) \equiv \int_{\mathrm{pH}_i}^{y} \beta \mathrm{dpH} = \Delta n, \tag{3.8}$$

where pH_i is the known initial sample pH and y is the final sample pH. The inverse function $x = g_{\mathrm{pH}_i}{}^{-1}(y)$ gives the number of moles of strong base, $x \equiv \Delta n$, necessary to change the sample pH from its initial to its final value. Now it is possible to specify a prior PDF for Δn thus take advantage of the knowledge of the initial sample pH and buffer capacity. Let X be a random variable representing Δn then the prior PDF for Δn will be $f_X(x)$. If Y is a random variable representing pH with PDF $f_Y(y)$ and both $y = g_{\mathrm{pH}_i}(x)$ and $x = g_{\mathrm{pH}_i}{}^{-1}(y)$ are monotonic, differentiable functions then the probability $y \leq Y \leq y + \mathrm{d}y$ must equal the probability $x \leq X \leq x + \mathrm{d}x$, or

$$|f_Y(y)\mathrm{d}y| = |f_X(x)\mathrm{d}x|.$$

Since the probabilities are always positive, this can be written as [53]

$$f_Y(y) = f_X(x)\left|\frac{\mathrm{d}x}{\mathrm{d}y}\right|. \tag{3.9}$$

The derivative on the right hand side can be evaluated by inputting eq. (3.8):

$$\left|\frac{\mathrm{d}x}{\mathrm{d}y}\right| = \left|\frac{\mathrm{d}}{\mathrm{d}y} g_{\mathrm{pH}_i}{}^{-1}(y)\right| = \left|\frac{\mathrm{d}}{\mathrm{d}y}\int_{\mathrm{pH}_i}^{y} \beta \mathrm{d}y\right| = \beta(y). \tag{3.10}$$

For the prior PDF of Δn I chose the normal distribution

$$X \sim \mathcal{N}\left(\mu_{\Delta n} = 0, \sigma^2_{\Delta n} = 0.0001\right).$$

This choice predicts no change in the pH of the sample on average and given the samples I used (see section 3.2), there is finite probability for pH from about

1.5 to 12.5 since the spread of the standard deviation of the normal distribution is quite large compared to the buffer strength. In future experiments more prior information would be available from the results of the current experiments thus the values for $\mu_{\Delta n}$ and $\sigma_{\Delta n}$ could be set accordingly. Then, in general with inputting $f_X(x) = \mathcal{N}\left(\mu_{\Delta n}, \sigma^2_{\Delta n}\right)$ into eqs. (3.9) and (3.10) the prior PDF for pH is

$$p(\mathrm{pH}|I) = f_Y(y) = \frac{\beta(\mathrm{pH})}{\sqrt{2\pi\sigma^2_{\Delta n}}} \exp\left(-\frac{\left({g_{\mathrm{pH}_i}}^{-1}(\mathrm{pH}) - \mu_{\Delta n}\right)^2}{2\sigma^2_{\Delta n}}\right). \tag{3.11}$$

For $\beta(\mathrm{pH})$ and ${g_{\mathrm{pH}_i}}^{-1}(\mathrm{pH})$ I will use the monoprotic buffer capacity given by eq. (2.10) since for all ensemble measurements only solutions of monoprotic acids were used. Thus it follows from eqs. (2.10) and (3.8) that

$$\begin{aligned} {g_{\mathrm{pH}_i}}^{-1}(\mathrm{pH}) &= \frac{K_w}{\gamma_{\mathrm{OH^-}} 10^{-\mathrm{pH}}} - \frac{10^{-\mathrm{pH}}}{\gamma_{\mathrm{H^+}}} + \sum_{\text{acids}} \left\{ \frac{C_a K_a \gamma_{\mathrm{HA}}}{10^{-\mathrm{pH}} \gamma_{\mathrm{A^-}} + K_a \gamma_{\mathrm{HA}}} \right\} \\ &\quad - \frac{K_w}{\gamma_{\mathrm{OH^-},i} 10^{-\mathrm{pH}_i}} + \frac{10^{-\mathrm{pH}_i}}{\gamma_{\mathrm{H^+},i}} - \sum_{\text{acids}} \left\{ \frac{C_a K_a \gamma_{\mathrm{HA},i}}{10^{-\mathrm{pH}_i} \gamma_{\mathrm{A^-},i} + K_a \gamma_{\mathrm{HA},i}} \right\} \\ &\approx \sum_{\text{acids}} \left\{ \frac{C_a K_a \gamma_{\mathrm{HA}}}{10^{-\mathrm{pH}} \gamma_{\mathrm{A^-}} + K_a \gamma_{\mathrm{HA}}} - \frac{C_a K_a \gamma_{\mathrm{HA}}}{10^{-\mathrm{pH}_i} \gamma_{\mathrm{A^-}} + K_a \gamma_{\mathrm{HA}}} \right\}, \end{aligned} \tag{3.12}$$

where the activity coefficients are not necessarily equal at the final and initial pH due to possible variation in the ionic strength; however, this effect should be minimal as it only affects the buffer ion concentrations which in the case of the tris samples the buffer strength is only 10 % of the ionic strength. Thus the approximation will be used.

A demonstration of the prior calculation see figs. 3.7 and 3.8. In these figures the normal distribution prior on Δn and eqs. (3.11) and (3.12) are shown. The prior on Δn is as discussed with $\mu_{\Delta n} = 0$ and $\sigma_{\Delta n} = 0.01$ in both figures. The prior for all tris samples is shown in fig. 3.7. The prior for NaOH samples depend the concentration of NaOH and the measured pH, but as an illustration the prior of a 10 mmol L^{-1} NaOH sample is shown in fig. 3.8. A key feature to take note of is the flat region in ${g_{\mathrm{pH}_i}}^{-1}(y)$ and $f_Y(\mathrm{pH})$ around pH = 4 to pH = 6 for tris and pH = 4 to pH = 10 for NaOH. In this region there is no

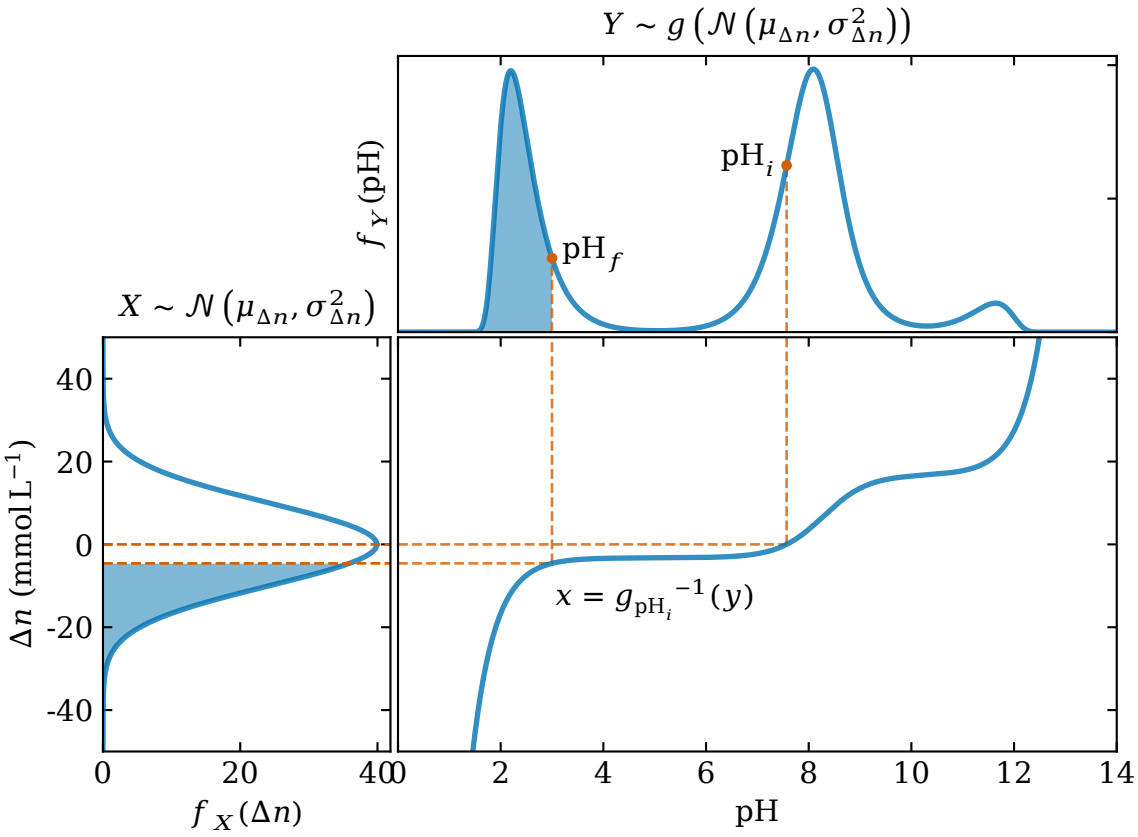

Figure 3.7. Prior PDF as calculated by eq. (3.11) for a 20 mmol L^{-1} tris solution at 200 mmol L^{-1} ionic strength initially at $\mathrm{pH}_i = 7.57$. The left panel shows the prior PDF for the amount of strong base added to the solution is normally distributed. The center panel shows the buffer dependent function that maps final pH (pH_f) to Δn. The top panel shows the corresponding prior PDF on pH. If $\Delta n = 0$ the initial and final pH would be identical as indicated by the dashed line. The other dashed line shows that integrating $f_X(\Delta n)$ from negative infinity to $\Delta n = -4.6$ mmol L^{-1} is identical to integrating $f_Y(\mathrm{pH})$ from negative infinity to $\mathrm{pH}_f = 3$.

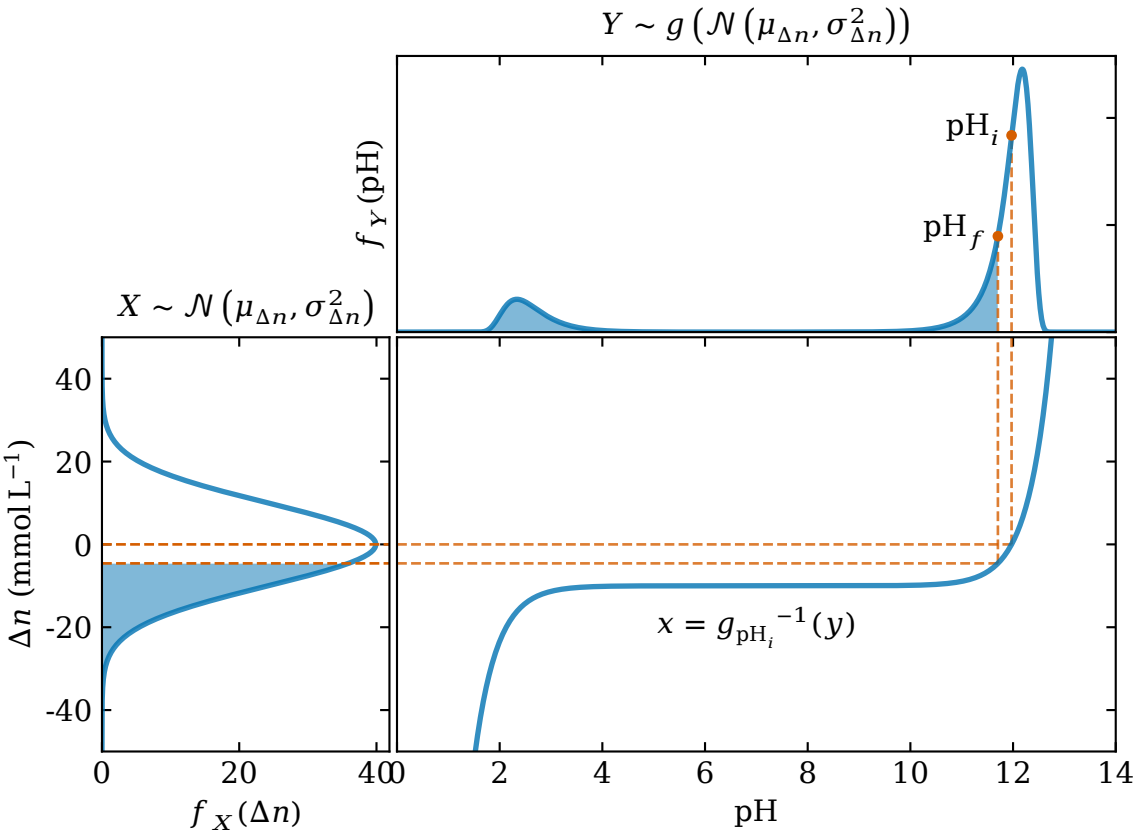

Figure 3.8. Prior PDF as calculated by eq. (3.11) for a 10 mmol L^{-1} NaOH solution at 200 mmol L^{-1} ionic strength initially at $\mathrm{pH}_i = 11.97$. The left panel shows the prior PDF for the amount of strong base added to the solution is normally distributed. The center panel shows the buffer dependent function that maps final pH (pH_f) to Δn. The top panel shows the corresponding prior PDF on pH. If $\Delta n = 0$ the initial and final pH would be identical as indicated by the dashed line. The other dashed line shows that integrating $f_X(\Delta n)$ from negative infinity to $\Delta n = -4.6$ mmol L^{-1} is identical to integrating $f_Y(\mathrm{pH})$ from negative infinity to $\mathrm{pH}_f = 11.7$.

essentially no buffer capacity such that a small change in Δn would cause the pH to change rapidly. Thus there is very little prior probability to measure a pH in this region. Although since there is non-zero probability if the emission ratio data suggests that the most likely pH is in this region then the prior would not reject such a measurement. In the lower and upper tails the prior probability rapidly diminishes therefore should the emission ratio data predict such a pH it would be heavily shifted inward. The prior will not likely alter the median value predicted by the data either, unless that prediction is weakly supported because of a large standard deviation. Then the main action of the prior is to change the shape of the prediction from the emission ratio data (likelihood) thus to change the shape of the posterior probability of pH. By altering the shape of the posterior PDF the prior has the desired effect of giving more meaning to the uncertainty and avoiding probabilities that extend to infinity if a measured ratio were outside the bounds of the calibration.

The likelihood of the fluorescein emission ratio data is calculated according to

$$p(R|\mathrm{pH}, M, \boldsymbol{\theta}, I) = \left(2\pi(\sigma_R^2 + \sigma_m^2(\mathrm{pH}))\right)^{-1/2} \exp\left(-\frac{(\mu_R - m(\mathrm{pH}|\boldsymbol{\theta}))^2}{2(\sigma_R^2 + \sigma_m^2(\mathrm{pH}))}\right) \quad (3.13)$$

where μ_R is the mean measured ratio, σ_R^2 is the standard deviation of the measured ratios, $m(R|\boldsymbol{\theta})$ is the ratio model function given in eq. (3.5), and $\sigma_m^2(\mathrm{pH})$ is the pH dependent model variance derived from the covariance matrix of the fit parameters. This formula accounts for statistical noise in the measurement and for statistical uncertainty in the model. It assumes that measurement errors and model uncertainty are normally distributed. This equation was taken from Gregory [53, p. 91].

To calculate the model variance let $\boldsymbol{\Sigma}_{\boldsymbol{\theta}} \in \mathbb{R}^{n\times n}$ be the variance–covariance matrix of the n model fit parameters. Then,

$$\sigma_m^2(\mathrm{pH}) = \boldsymbol{J}\boldsymbol{\Sigma}_{\boldsymbol{\theta}}\boldsymbol{J}^{\mathrm{T}}, \quad (3.14)$$

where $\boldsymbol{J} \in \mathbb{R}^{1\times n}$ is the Jacobian matrix of the model function evaluated at the best fit parameter values and at the desired pH as follows:

$$\boldsymbol{J} = \frac{\partial}{\partial \boldsymbol{\theta}} m(\text{pH}|\boldsymbol{\theta}) = \left[\frac{\partial m}{\partial \theta_1} \cdots \frac{\partial m}{\partial \theta_n}\right]. \tag{3.15}$$

This method of calculating the model variance account for the parameter variances $\text{diag}(\boldsymbol{\Sigma_\theta})$ as well as the parameter covariances from the off-diagonal elements of $\boldsymbol{\Sigma_\theta}$.

With the prior PDF and likelihood now determined it is possible to calculate the posterior PDF. From Bayes' Theorem [see eq. (3.7)] and using the notation developed thus far the posterior PDF for pH is

$$p\left(\text{pH}|R, M, \boldsymbol{\theta}, I\right) = \frac{p\left(R|\text{pH}, M, \boldsymbol{\theta}, I\right) p\left(\text{pH}|I\right)}{p\left(R|M, \boldsymbol{\theta}, I\right)}. \tag{3.16}$$

The information necessary and designated by I to calculate the prior [see eq. (3.11)] include the sample solution constituents, initial sample pH, the theoretical calculation of buffer capacity, and prior knowledge of the expected Δn. The information, I, needed to calculate the likelihood [see eq. (3.13)] include the fluorimeter–fluorescein calibration data, the model function of the calibration described in section 3.3, the best fit parameters ($\boldsymbol{\theta}$) of the model, and the variance–covariance matrix of the model parameters ($\Sigma_{\boldsymbol{\theta}}$). Recall that the denominator, $p\left(R|M, \boldsymbol{\theta}, I\right)$, is simply a normalization factor calculated by integrating the numerator over pH.

Two examples of the calculation of the posterior PDF are shown in fig. 3.9. In this figure the prior is shown by the dotted blue lines, the likelihood by dashed green lines, and the posterior by solid orange lines. Both panels share hypothetical data where $\mu_R = 0.22$; however, the top panel is shown with $\sigma_R = 0.008$ while the lower panel with $\sigma_R = 0.002$. It can be seen that the likelihoods both predict the same pH, but when the standard deviation of the data is large the spread of the likelihood is also large and thus the posterior

is more affected by the shape of the prior. And when small the posterior is virtually unaffected by the prior.

From the posterior PDFs the most probable pH values (the maxima of the posteriors) are reported along with a 95 % credible interval where the credible interval was calculated by using the highest density interval. To calculate the highest density interval I integrated the posterior PDF starting from the most probable value then added points to the left or the right ensuring that as the left and right bounds were extended, the direction of extension was chosen to maximize the probability until the target credible interval was reached. In other words I define the highest density interval as a continuous, unbroken interval about the most probable value which maximizes the growth rate of the interval.

3.6 Droplet Data: pH

Now it is possible to calculate the pH of the ratio data in in section 3.4, figs. 3.5 and 3.6 by applying the bayesian analysis described in the previous section. The result of this analysis is shown in figs. 3.10 and 3.11. The results show that the pH in droplets is lower than the bulk sample from which they were prepared but as more sodium hydroxide or more surfactant is added the pH of droplets tends towards the bulk pH. The dynamic range of the pH data for points which are within the bounds of the calibration (filled symbols) is also more compressed than that of the ratio data indicating that there is less change than was originally suggested by the ratio data. It can also be seen that the uncertainty is asymmetric and that the uncertainty for data out of the bounds of the calibration (open symbols) become very large. This is especially apparent in the tris data, fig. 3.11, where the low points out of the calibration bounds now appear not that dissimilar from the data within the bounds of the calibration.

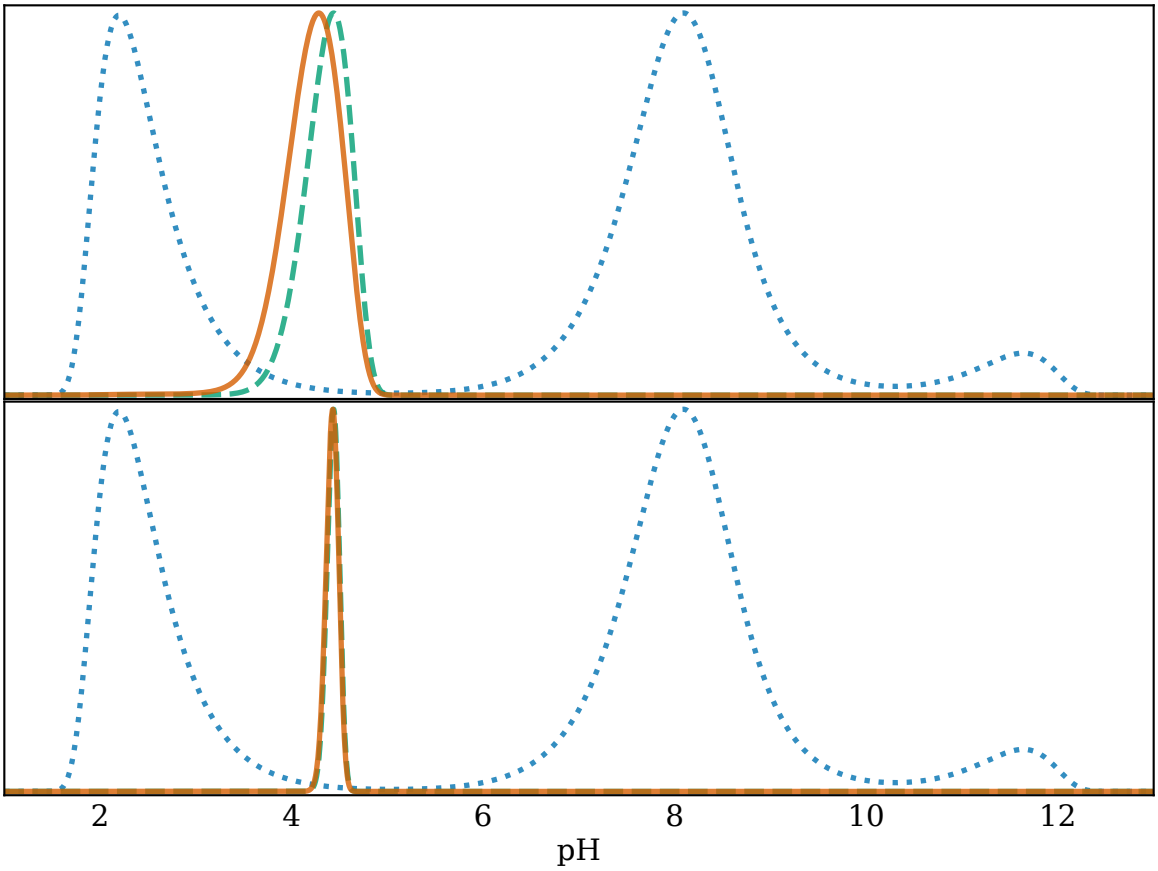

Figure 3.9. Bayesian analysis of fluorimeter ratio data. The dotted blue lines show the prior probability density function, see eq. (3.11), shown here a solution containing $20\,\mathrm{mmol\,L^{-1}}$ tris buffer at pH = 7.57 and at $200\,\mathrm{mmol\,L^{-1}}$ ionic strength. The dashed green lines show the likelihood function [see eq. (3.13)] of hypothetical emission ratio measurements with (μ_R, σ_R) equal to (0.22, 0.008) in the top panel and (0.22, 0.002) in the bottom panel. The solid orange lines show the posterior probability density function [see eq. (3.16)]. Note that all curves are scaled to the same height for illustration purposes.

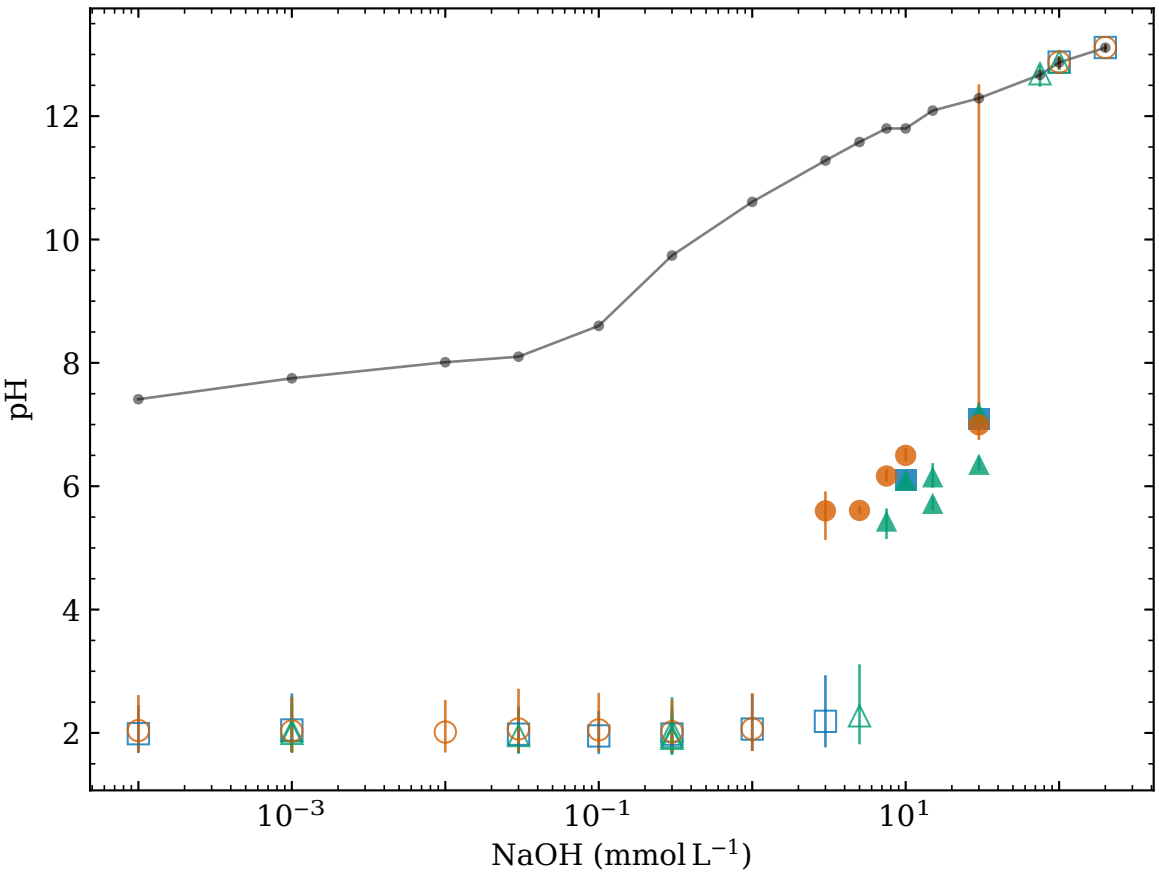

Figure 3.10. pH of droplets made from NaOH solutions and FC-40 without surfactant. Data shown is the result of bayesian analysis of the ratios in fig. 3.5. All solutions had approximately 200 mmol L^{-1} ionic strength. Three different runs were performed and are shown by different color–symbol pairs. The solid gray line indicates the pH of the bulk as measured by a glass electrode. Open symbols indicate fluorescein emission ratio measurements which were out of or at the very edge of the bounds of the calibration and filled symbols otherwise.

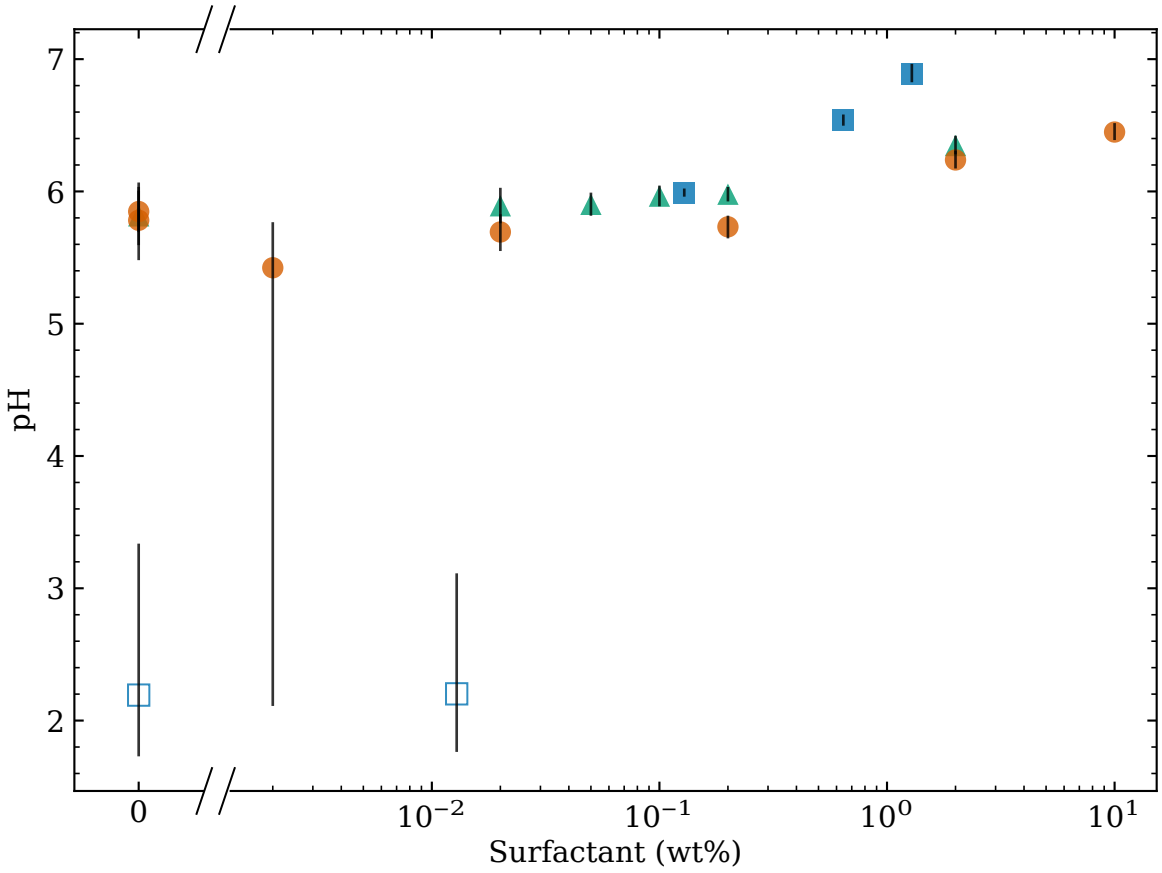

Figure 3.11. pH of droplets made from 20 mmol L^{-1} tris buffer with 186 mmol L^{-1} ionic strength at pH = 7.57 and FC-40 with varying surfactant concentration. Data shown is the result of bayesian analysis of the ratios in fig. 3.6. Three different runs were performed and are shown by different color–symbol pairs. Open symbols indicate fluorescein emission ratio measurements which were out of or at the very edge of the bounds of the calibration and filled symbols otherwise.

3.7 Droplet Data: Δn

The next step in my analysis was to calculate the molar equivalent of strong base, Δn, necessary to change the pH of the emulsion droplets from the initial to the final pH. This calculation is done by evaluating ${g_{\mathrm{pH}_i}}^{-1}(\mathrm{pH}_f)$ [see eq. (3.12)] at the final pH values, pH_f. This is equivalent to integrating the buffer capacity as demonstrated in fig. 3.12 for a tris solution and an NaOH solution with $\Delta n = -10\,\mathrm{mmol\,L^{-1}}$ in both cases.

To obtain uncertainty on Δn I applied standard uncertainty propagation techniques through ${g_{\mathrm{pH}_i}}^{-1}$ of the variances of the following parameters: final pH, initial pH ($\sigma_{\mathrm{pH}_i} = 0.04$), total buffer concentration ($\sigma_{C_a}/C_a = 0.05$), solution ionic strength ($\sigma_I/I = 0.05$), and temperature ($\sigma_T = 1$). To maintain the asymmetric uncertainty of the previous analysis I compute

$$\sigma^2_{\Delta n} = \boldsymbol{J}\,\boldsymbol{\Sigma}\,\boldsymbol{J}^{\mathrm{T}}$$

two times; one for positive uncertainty and one for negative uncertainty which used the positive and negative variance of final pH respectively. In these calculations $\boldsymbol{\Sigma}$ is diagonal with the variances specified and the Jacobian is equivalent to the gradient evaluated at the most probable values.

For the NaOH data, results are shown in figs. 3.13 and 3.14. It is now evident that open symbol data corresponding to low emission ratio which were out of the calibration bounds data appear only slightly lower than the rest of the data within uncertainty. In other words a small uncertainty in pH is actually a large uncertainty in Δn due to pH being on a logarithmic scale. The open symbol data at high NaOH concentration do have large uncertainty they do not disagree with $\Delta n \approx 0$, a reasonable expectation that large concentrations of NaOH would not significantly change by emulsification. However, nominally my initial expectation would be that irregardless of the NaOH concentration Δn would be identical for all emulsions. While the data overall show Δn between $0\,\mathrm{mmol\,L^{-1}}$ and $20\,\mathrm{mmol\,L^{-1}}$, there is a slight trend in the more reliable filled

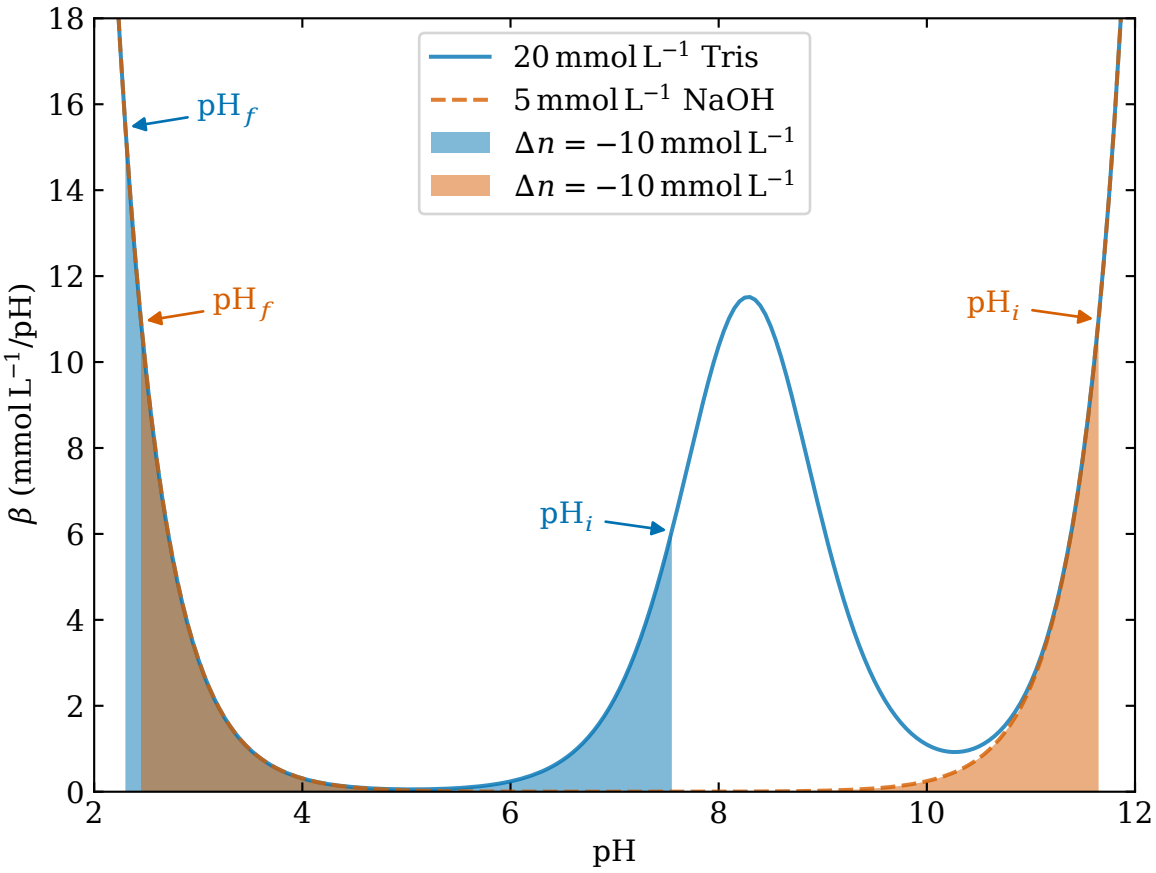

Figure 3.12. The effect of a $-10\,\mathrm{mmol\,L^{-1}}$ addition of strong base is shown for two hypothetical solutions: $20\,\mathrm{mmol\,L^{-1}}$ tris buffer initially at pH = 7.57 (blue) and $5\,\mathrm{mmol\,L^{-1}}$ NaOH solution initially at pH = 11.67 (orange). Both solutions assume $200\,\mathrm{mmol\,L^{-1}}$ ionic strength. The buffer capacity of tris (NaOH) is indicated by the solid blue line (dashed orange line) and was calculated using eq. (2.9). The final pH were calculated by bisection of ${g_{\mathrm{pH}_i}}^{-1}(\mathrm{pH}_f) = -10$ where ${g_{\mathrm{pH}_i}}^{-1}$ is given in eq. (3.12). The shaded regions indicate a $-10\,\mathrm{mmol\,L^{-1}}$ addition of strong base.

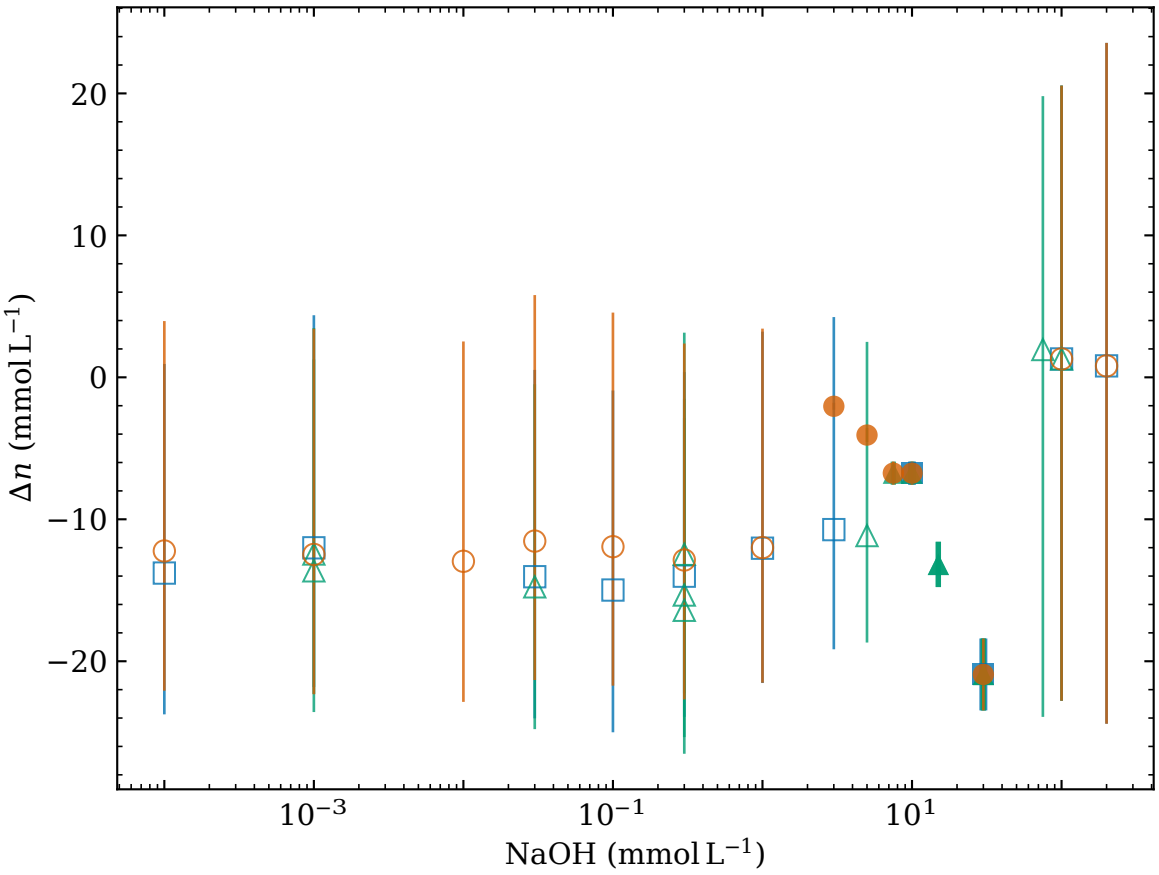

Figure 3.13. Effective molar addition of strong base is shown for droplets made from NaOH solutions and FC-40 without surfactant. All solutions had approximately 200 mmol L^{-1} ionic strength. Three different runs were performed and are shown by different color–symbol pairs. The solid gray line indicates the pH of the bulk as measured by a glass electrode. Open symbols indicate fluorescein emission ratio measurements which were out of or at the very edge of the bounds of the calibration and filled symbols otherwise. For showing only the filled symbols see fig. 3.14.

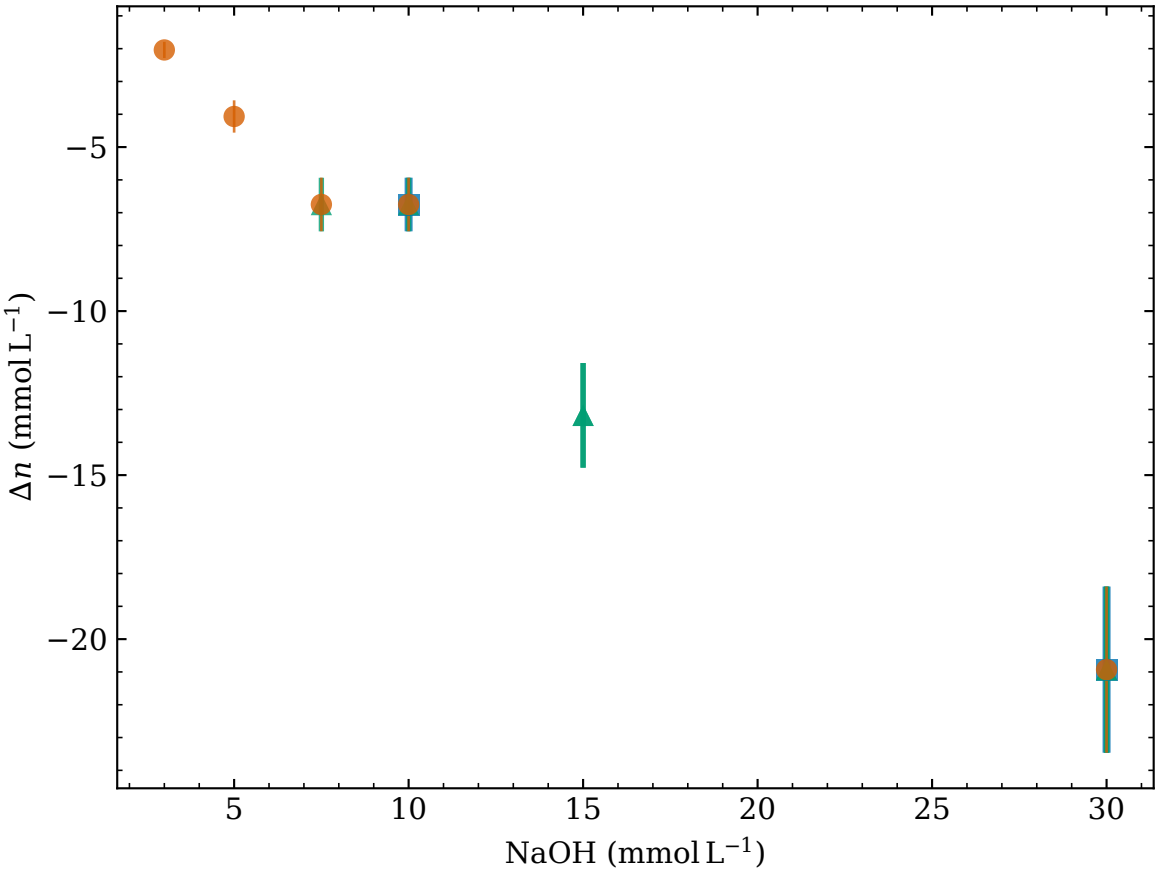

Figure 3.14. Effective molar addition of strong base is shown for droplets made from NaOH solutions and FC-40 without surfactant. All solutions had approximately 200 mmol L^{-1} ionic strength. Three different runs were performed and are shown by different color–symbol pairs. Only selected data are shown; all the data are shown in fig. 3.13.

symbol data. A plot of only the filled symbol data is shown in fig. 3.14 and indicate that the higher the NaOH concentration, the larger is Δn.

For the tris data, results are shown in figs. 3.15 and 3.16. The major difference when compared to the corresponding pH plots is that the two open symbols that are from ratios out of the bounds of the calibration are now no longer distinguishable within the uncertainty from the other points. These two data are much less reliable and therefore I remove them and show a plot of only the filled symbols (see fig. 3.16). From this plot a slight trend with surfactant is still visible and all data are within the same range as the NaOH data.

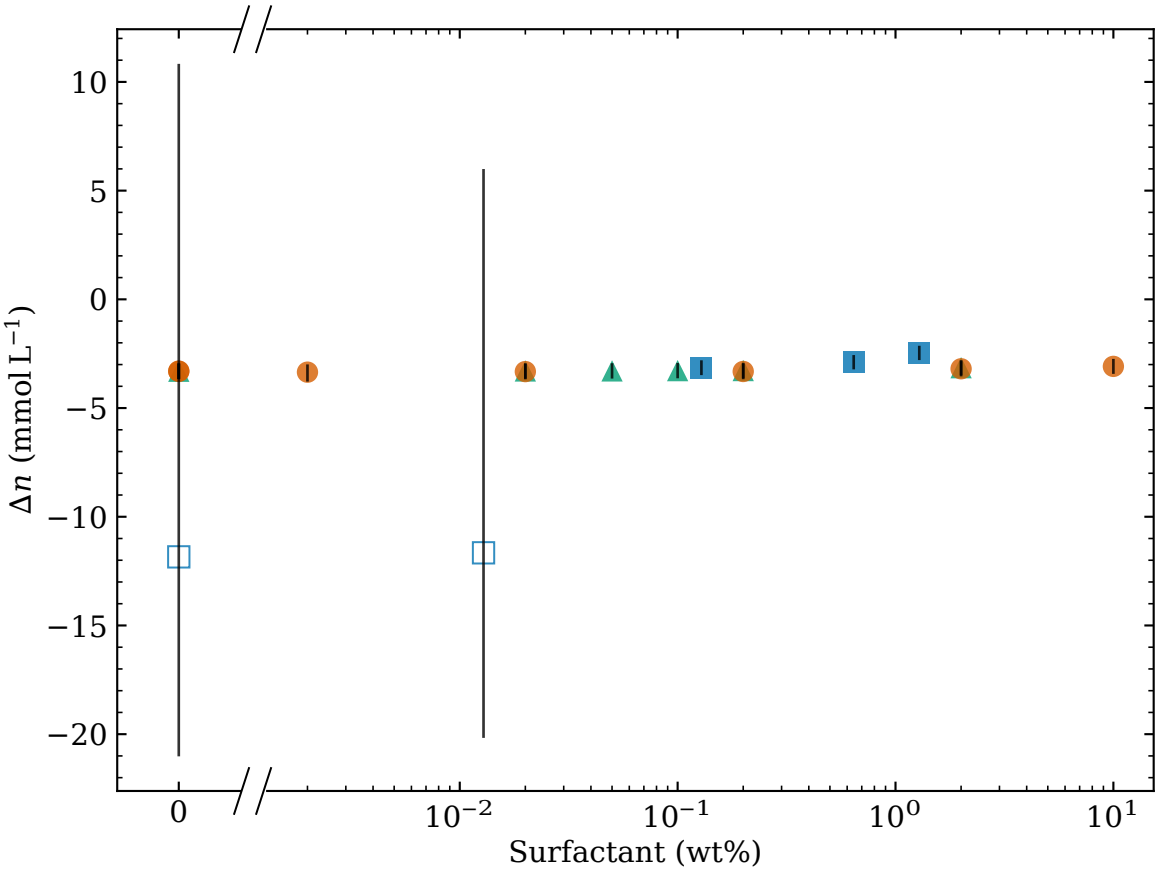

Figure 3.15. Effective molar addition of strong base is shown for droplets made from 20 mmol L^{-1} tris buffer with 186 mmol L^{-1} ionic strength at pH = 7.57 and FC-40 with varying surfactant concentration. Three different runs were performed and are shown by different color–symbol pairs. Open symbols indicate fluorescein emission ratio measurements which were out of or at the very edge of the bounds of the calibration and filled symbols otherwise. For a plot showing only the filled symbols see fig. 3.16.

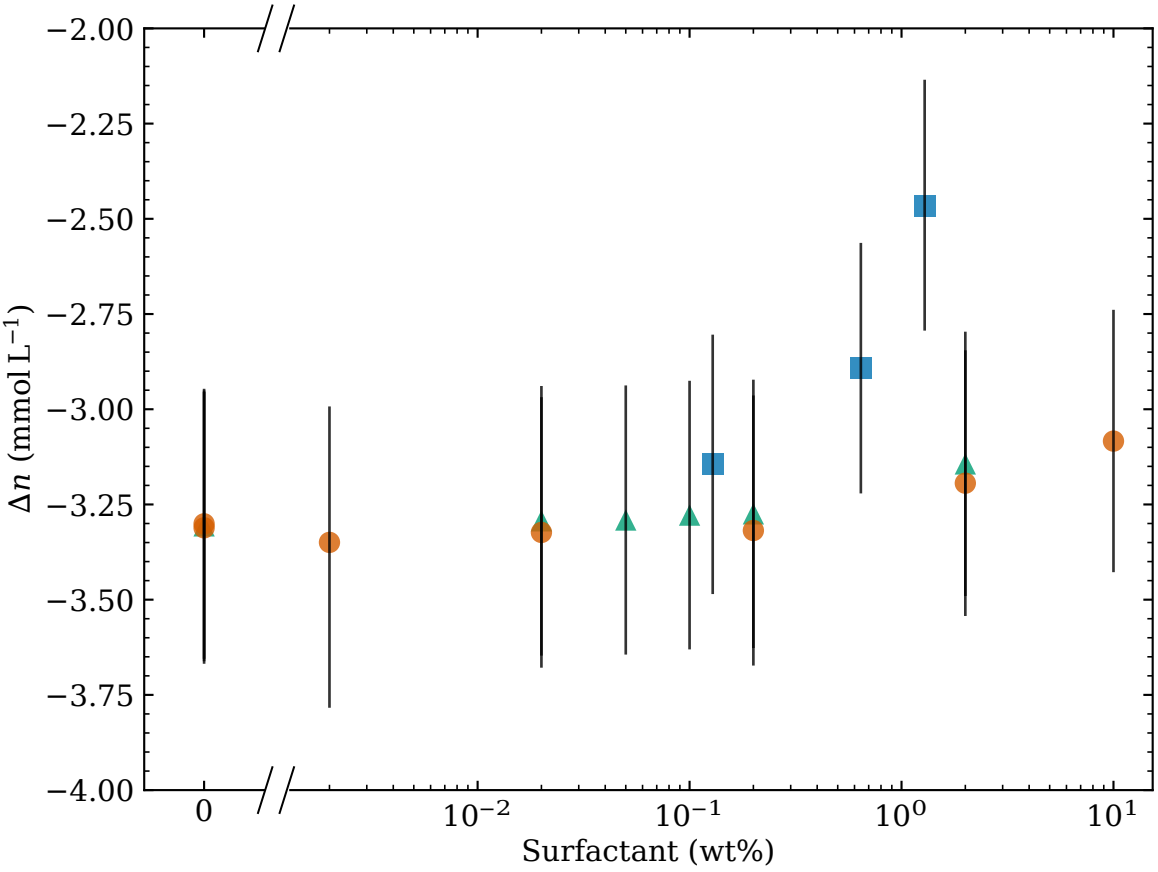

Figure 3.16. Effective molar addition of strong base is shown for droplets made from 20 mmol L^{-1} tris buffer with 186 mmol L^{-1} ionic strength at pH = 7.57 and FC-40 with varying surfactant concentration. Three different runs were performed and are shown by different color–symbol pairs. Only selected data are shown; for a plot of all the data see fig. 3.15.

Assuming that the cause of $\Delta n < 0$ is because hydroxide ions leave the core of the droplet and plate out on the surface then I can calculate a surface charge density of hydroxide ions by

$$\sigma = N_{\mathrm{A}} \frac{V_{\mathrm{drop}}}{S_{\mathrm{drop}}} \Delta n = N_{\mathrm{A}} \frac{r}{3} \Delta n, \tag{3.17}$$

where V_{drop} and S_{drop} are the volume and surface area of the droplet respectively, and $N_{\mathrm{A}} = 6.022 \times 10^{23}\,\mathrm{mol}^{-1}$ is the Avogadro constant. Based on the filtered NaOH and tris data a reasonable range for Δn is $-2\,\mathrm{mmol\,L}^{-1}$ to $-20\,\mathrm{mmol\,L}^{-1}$ and although the precise average droplet diameter is unknown I will assume 200 nm to calculate the surface charge density. In this way the calculation shows about $0.04\,\mathrm{OH}^-\,\mathrm{nm}^{-2}$ to $0.4\,\mathrm{OH}^-\,\mathrm{nm}^{-2}$. This is consistent with the values reported in Beattie and Djerdjev [29]. Beattie found that for various hydrocarbon oil in water emulsions the surface charge density was $-7.3\,\mu\mathrm{C\,cm}^{-2}$ to $-4.6\,\mu\mathrm{C\,cm}^{-2}$ when no surfactant was used and for squalene with $2\,\mathrm{mmol\,L}^{-1}$ surfactant (sodium dodecylsulfate) it was $-1.6\,\mu\mathrm{C\,cm}^{-2}$. This corresponds to $0.1\,\mathrm{OH}^-\,\mathrm{nm}^{-2}$ to $0.46\,\mathrm{OH}^-\,\mathrm{nm}^{-2}$ which overlaps with my data.

The data in fig. 3.14 show a linear trend. This trend could have several possible explanations. It could be that droplet size decreases as the sodium hydroxide concentration increases such that the magnitude of Δn would need to increase if the surface charge density is constant. It could also be that there is a shift in the ionization constants of the fluorescein due to interaction with the surface. Such a scenario would be difficult to distinguish from a change in pH and a $\mathrm{p}K_a$ shift cannot be easily assumed due to there being three constants that are subject to change. Another possible explanation is given that these emulsions are not surfactant stabilized, the rate of ageing is increased. The combined ageing effect of Ostwald ripening and coalescence is to shrink the average droplet size in the emulsion. As the droplets shrink they loose water and may not loose ions. In this way the fluorescein concentration and ionic strength would both increase. According to figs. 3.3 and 3.4 these increases lead to

lower fluorescein emission ratio therefore lower pH and larger magnitude of Δn.

Finally it is important to realize that the properties of water in a 200 nm diameter droplet may differ from that of bulk water. Namely, the definition of pH may no longer be valid since at pH = 7, there would only be 0.25 hydrogen ions per droplet on average and this number will drop by one order of magnitude per pH increment. As shown in table 3.2 the bulk pH of all NaOH data range from 7.41 to 13.11 such that if the droplet pH were not significantly different then the hydrogen ion concentration would be diminishing potentially affecting the photophysics of fluorescein.

CHAPTER 4

SINGLE DROPLET pH MEASUREMENTS

4.1 Introduction

In this chapter I will discuss a method I developed for simultaneously measuring the pH and size of emulsion droplets. This is a single-droplet technique using a modified fluorescence microscope which acquires “two-color” images. To obtain a calibration for this method required noise reduction, feature extraction, affine transformation, image segmentation, and spline fitting. Droplet trajectories of interest were obtained by affine transformation then particle tracking and particle filtering. Droplet size was then determined by calculation and fitting of the mean square displacements (MSD) from the particle trajectory. Droplet pH was determined from spatio-temporal calibration lookup of affine transformed droplet images, with careful attention to background estimation, using a fluorescence emission ratio to lookup pH similar to the ensemble approach. This method was capable of measuring pH and size for droplets with radii down to about 40 nm diameter.

For these measurements I used Oregon Green 488 (OG488) as the fluorescent pH sensor due to its higher quantum yield and greater photostability when compared to fluorescein [54]. OG488, also called 2’,7’-difluorofluorescein, is an analog of fluorescein thus it also has four charged states (see figs. 2.1 and 2.2) and three ionization constants [see eqs. (2.20a) to (2.20c)]. However, due to the high electronegativity and small van der Waals radius of the fluorine atom, and the double substitution of hydrogen atoms with fluorine atoms, there are profound changes to the behavior OG488 compared to fluorescein [46]. According to fig. 2.3 the shape of the spectra of OG488 are largely unchanged in comparison to fluorescein; however, the ionization constants are significantly

lower with the pK_a's reported as 1.016(7), 3.610(10), and 4.688(4) [45]. Therefore the useful range of OG488 as a pH sensor is at best approximately 0 to 6.5. Oregon Green 488 was purchased from Life Technologies Corporation (now a division of Thermo Fisher Scientific), had catalog number D6145, and one of two lot numbers: 1555273 or 1819905. The concentration of OG488 was $50\,\mu\text{mol}\,\text{L}^{-1}$ in all experiments. This slightly increased concentration in comparison to fluorescein in the fluorimeter measurements helped to boost the signal-to-noise ratio of single-droplets while still avoiding dye self-quenching.

As described in section 2.3 the fluorescence measurement of pH requires acquisition of two intensities, I_0 and I_1, to calculate the emission ratio, eq. (2.21). Since each intensity is the result of integrating the dye emission spectrum, i_{em}, transmitted through the filters and dichroics, $T(\lambda)$, $I = \int i_{\text{em}}(\lambda)T(\lambda)\text{d}\lambda$, then the location and width of the spectral bands determine the maximum dynamic range of the emission ratio and therefore the sensitivity of the calibration curve. In the fluorimeter measurements the spectral bandwidth was set to 3 nm while in the microscopy measurements the spectral bands were set as wide as possible within the limitations of the optical setup described in section 4.2.2 to maximize the signal-to-noise ratio of the images of droplets. Higher signal-to-noise increases the fidelity of the emission ratio and size measurements since these measurements depend on the localization accuracy. Thus the spectral bands in the microscopy measurements were 498 nm to 526 nm for I_1 and 526 nm to 710 nm for I_0.

4.2 Methods

4.2.1 Sample Preparation

Like in the fluorimeter measurements emulsions were prepared from an aqueous pH buffered sample and FC-40. The primary buffer used was citrate which has three ionizations [see eqs. (2.11a) to (2.11c)] with the following ionization constants: 3.128, 4.761, and 6.396. Due to the multiple ionizations

citrate is useful as a buffer over a much wider range in comparison to tris. Citrate also has much higher buffer capacity at lower pH values due to its lower ionization constants.

In the microscopy measurements emulsions were prepared via tip sonication instead of the bath sonication method which was used in the fluorimeter measurements. The reasons for the switch to tip sonication include: it is a more efficient processing method such that the sample:FC-40 ratio is more accurate and repeatable, it is faster, it is capable of much lower sample:FC-40 ratios, and it is capable of making low volume emulsions. Therefore it is also a lower cost method due to the high cost of surfactant.

The tip sonicator setup, shown in fig. 4.1, included a Sonics VCX-750 Ultrasonic Processor (750 W, 20 kHz), a "reverse coupler" (Sonics P/N: 630-0613) which attenuates the amplitude, and a 2 mm stepped microtip probe (Sonics P/N: 630-0423). The small diameter of the stepped microtip allowed preparation of very small volumes of emulsion. The sonicator had an amplitude control setting that ranges from 21 % to 100 %; however, when the reverse coupler was equipped the amplitude range should be considered as approximately halved to 11.5 % to 50 % which is helpful in reducing the very high gain of the stepped microtip. I always used the reverse coupler when preparing emulsions and I found the ideal amplitude setting for FC-40 using this setup was about 60 % to 70 % (approximately equal to 30 % to 35 % if not using the reverse coupler). It was possible to determine the correct setting by visual and aural cues: too low of an amplitude caused too little cavitation and no rigorous mixing while too high of an amplitude caused too much cavitation and significantly vaporizes the FC-40.

To prepare an emulsion usually 0.5 µL sample was placed on the bottom of the tip sonicator probe and 200 µL of FC-40 with or without surfactant was placed in an 0.6 mL microcentrifuge tube which was then brought up and around the probe such that the probe was submerged in the fluid about 2 mm to 5 mm as shown in fig. 4.2. In this way the initial drop of sample sticks to the probe, is

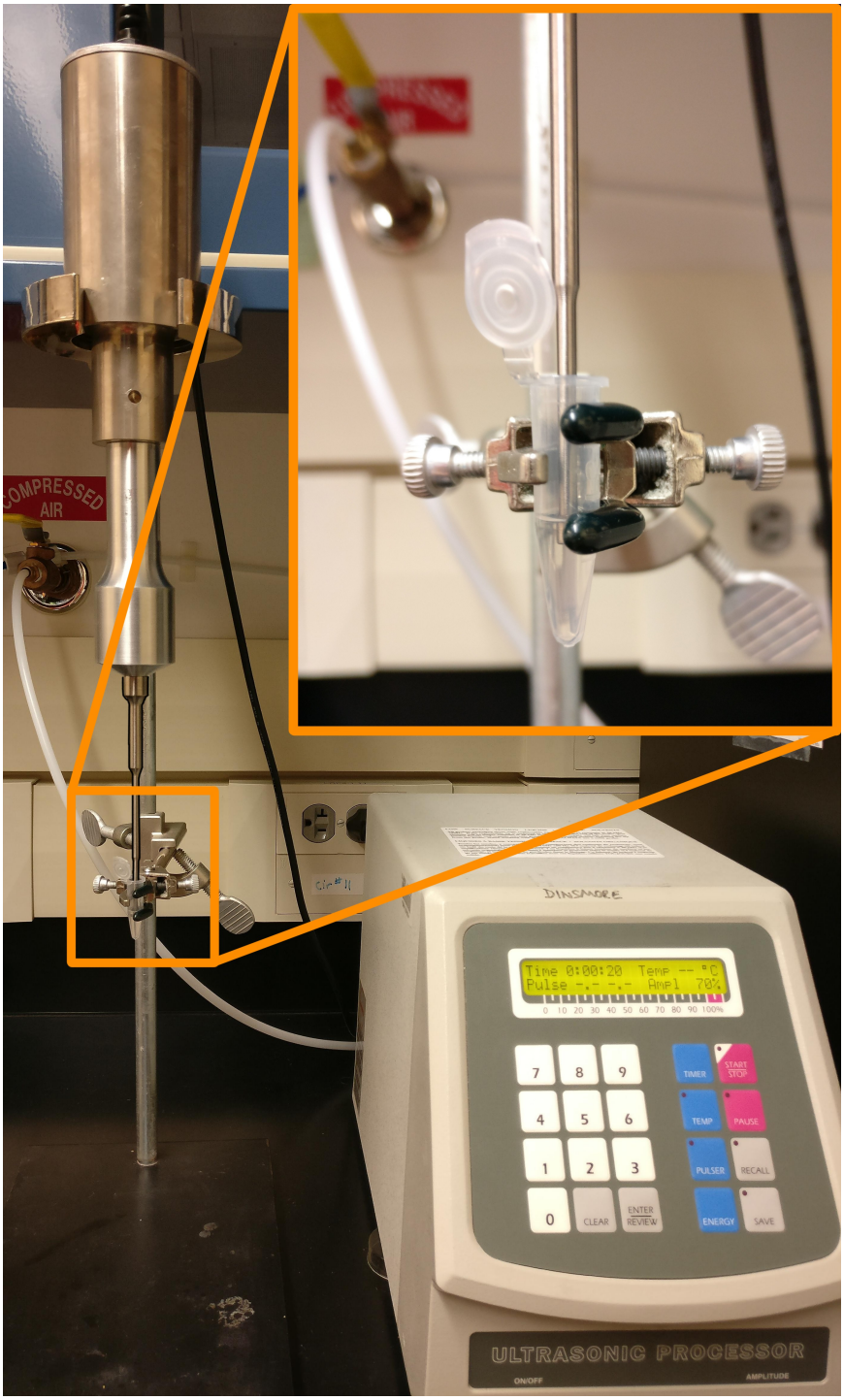

Figure 4.1. Tip sonicator setup with a sample mounted and ready to be emulsified. The tip sonicator is a Sonics VCX-750 with a "reverse coupler" (Sonics P/N: 630-0613) and a 2 mm stepped microtip probe (Sonics P/N: 630-0423) mounted on the transducer. The stepped microtip is outlined in black. The inset shows how the sample tube is held during sonication. For a close-up of the sample tube and probe tip see fig. 4.2.

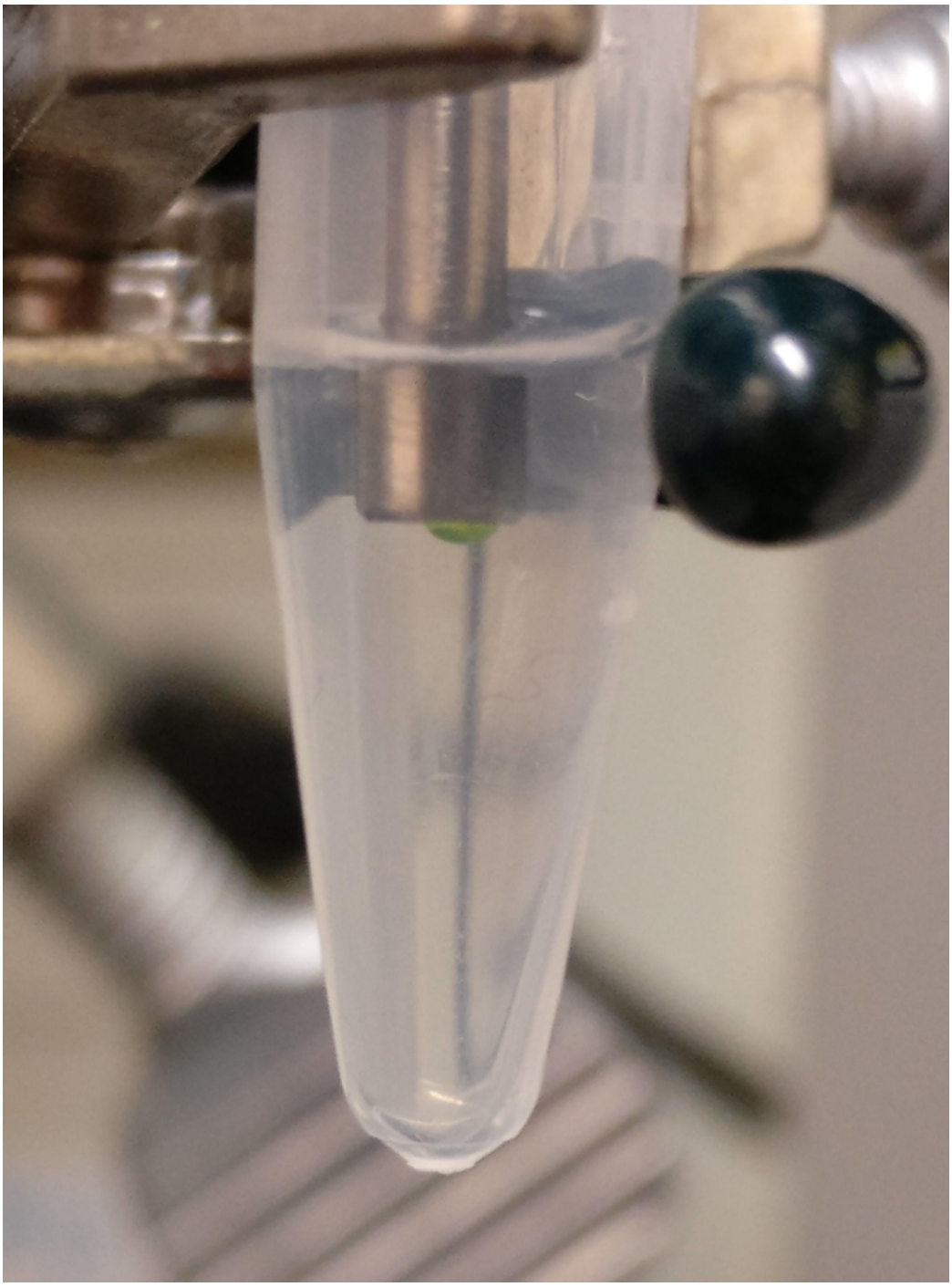

Figure 4.2. An emulsion just before emulsification and mounted on the tip sonicator setup. The emulsion contains 200 µL of FC-40 and a 0.5 µL (green) drop of sample containing OG488 which is suspended on the tip of the sonicator. The probe is submerged about 2 mm below the surface of the FC-40. For a full, zoomed out, view of the tip sonicator setup see fig. 4.1.

prevented from floating to the top surface, and is much more readily emulsified when the probe is energized. The amplitude should be sufficiently high to break up the initial drop of sample, prevent it from floating and remaining on the top surface, and prevent it from sticking to the side of the probe or walls of the tube, all by continuously mixing it to keep it passing through the high intensity region of greatest cavitation. For this method to work it is necessary that the initial drop of sample sticks to the probe and does not float to the top surface as soon as the tube of FC-40 is brought around the probe. This can be done by ensuring there is no residual FC-40 or surfactant on the probe by cleaning via sonication in acetone and water, then blowing dry with N_2 between making emulsions.

Once prepared, an emulsion is loaded into a sample chamber. A sample chamber is made from a glass slide and a glass coverslip connected by strips of double faced tape separated about 3.5 mm apart forming a channel about 100 µm deep and 22 mm long. An image of a sample holder with eight sample chambers (six of them filled with OG488 samples) and undergoing data acquisition is shown in fig. 4.3. After a sample chamber is filled it is sealed on the two open ends with VALAP.*

All glass slides and coverslips were cleaned with the following multi-step process using a bath sonicator: (1) sonication for 20 min in 5 vol% Sparkleen 1, (2) two rinses with deionized water and sonication for at least 5 min in deionized water, (3) sonication for 20 min in 10 wt% KOH solution, and (4) repeat step two. Cleaned glass slides and coverslips were stored in deionized water until ready for use then blown dry with N_2 just before use.

*VALAP is a 1:1:1 mixture (by weight) of Vaseline, lanolin, and paraffin. VALAP is soft at room temperature and has a low melting point so is easily liquefied by an alcohol stove. To use for sealing sample chambers a capillary is filled by pushing into solid VALAP then heated on an alcohol stove and then the capillary is run over the edge to be sealed. When sealing a sample chamber that was filled with FC-40 it works better if the VALAP is very hot to displace the FC-40 from the glass giving a better seal.

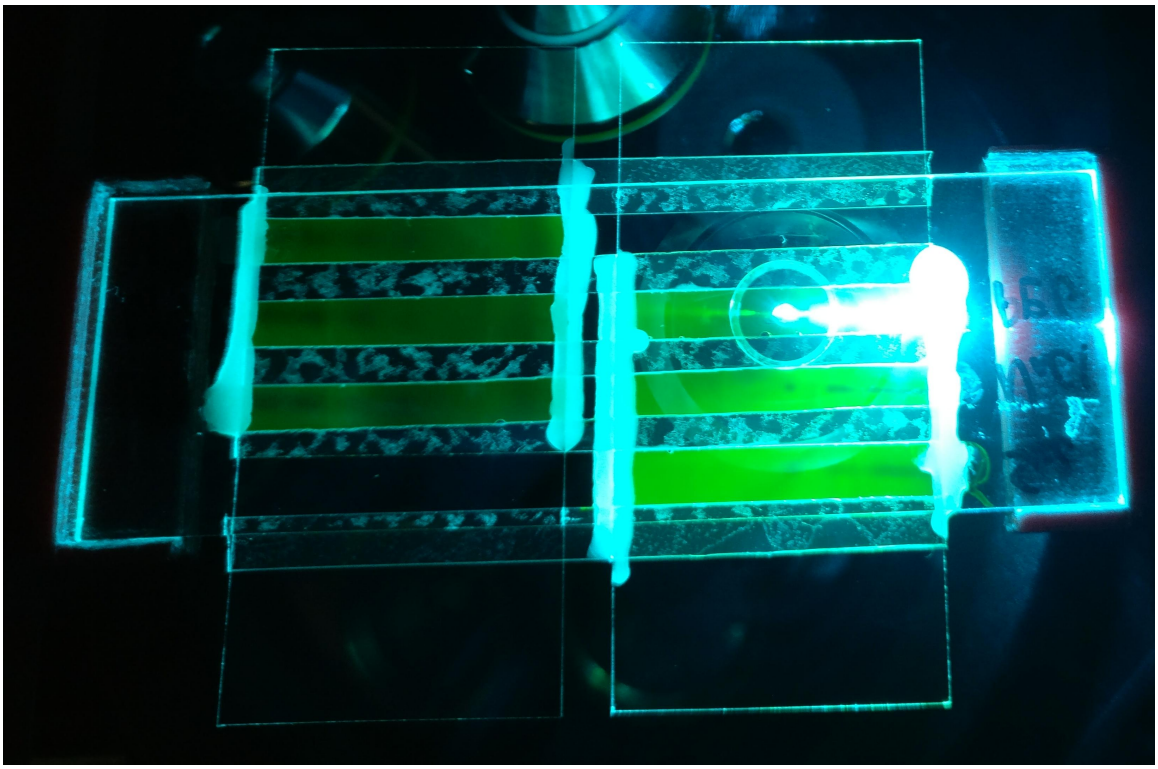

Figure 4.3. A sample holder with six of eight chambers filled, one of which was undergoing data acquisition on the microscope. The sample holder is made of a cleaned glass slide and two cleaned coverslips with five strips of double sided tape. For details of the glass cleaning process see text. After the chambers were filled with sample they were sealed with VALAP and then placed on the microscope stage coverslip down. The samples shown here were for calibration, so are brightly fluorescent and thus are good at demonstrating that the observation volume and areas to the right are readily photobleached. Therefore to avoid repeated acquisitions in a photobleached area data are acquired from the right edge of a chamber to the left edge of that chamber.

4.2.2 Optical Setup

The optical setup for measuring droplet pH is shown in fig. 4.4. The setup uses a 200 mW Sapphire 488 nm diode pumped solid state laser (DPSSL), an Olympus IX-81 inverted fluorescence microscope with a 60x, 1.45 numerical aperture oil-immersion[†] objective (PLAPON60XOTIRFM), a modified TIRF excitation arm, a Hamamatsu Photonics ORCA Flash 4.0 V2+ scientific CMOS (sCMOS) camera, and an Arduino for controlling the camera and shutters. The microscope was also equipped with an Olympus ZDC2 continuous autofocus system that was used in all experiments to maintain the observation volume a specific z height above the coverslip.

The microscope fluorescence filter cube was equipped with a Chroma ET488/10x (488(5) nm) excitation filter, Semrock Di01-R488 (488 nm split) dichromatic mirror, and a Chroma RET493LP (493 nm long pass) emission filter.

The laser launch allowed the laser to be used in epifluorescence, variable-angle fluorescence, or total internal reflection fluorescence where the laser emits out of the objective vertically, greater than 0° and less than 90° above the horizontal, or not at all respectively. The laser launch was modified by changing the manufacturer dovetail mounted fiber mount/translator with a 5-axis kinematic mount for easier alignment, faster alignment, and faster switching between excitation modes. To obtain droplet trajectories it is necessary for the droplets to be freely diffusing, which means the droplets must be observed away from the coverslip surface such that any perturbations in the droplet movements would be reduced or eliminated. Therefore in all data, I recorded droplets with the z focal plane of the microscope set to 3.5 µm to 20.1 µm from the bottom (coverslip) surface.

To obtain the two spectral bands, I_0 and I_1, it is necessary to have either two cameras or an optical setup which can split the spectral bands onto two halves of a single camera. The latter method is called a “dual-view” setup and is what

[†]Olympus Type F immersion oil was used in all experiments.

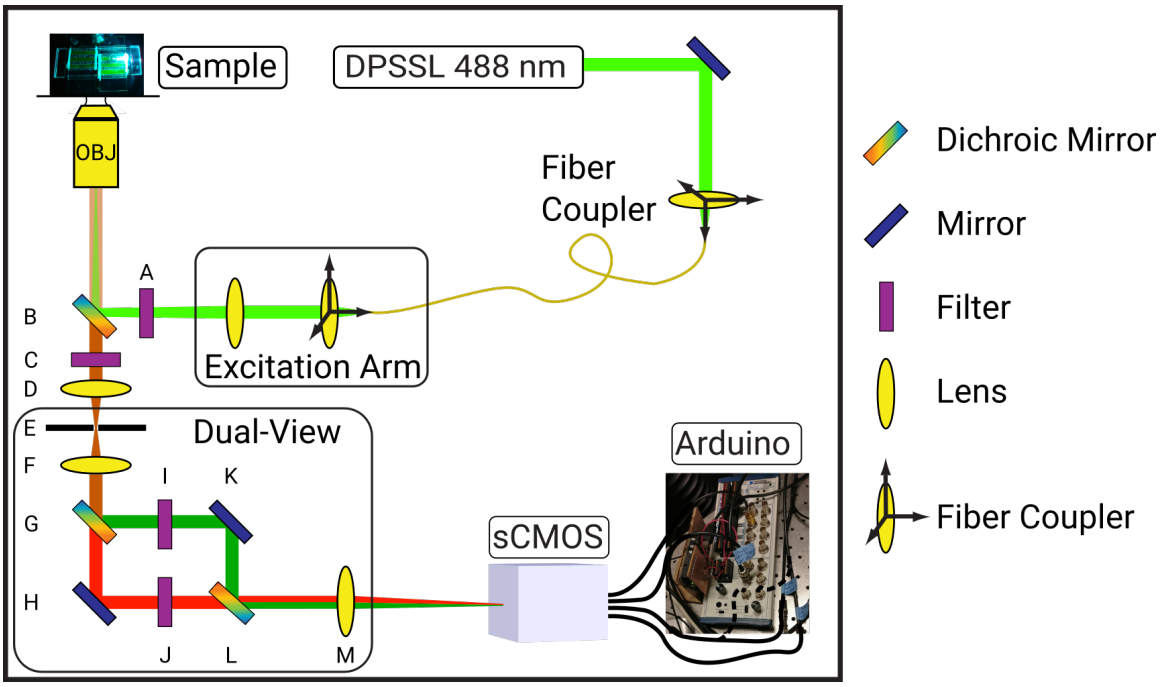

Figure 4.4. Optical setup of the microscope. The setup uses a 488 nm fiber-coupled laser and an sCMOS camera which was controlled by an Arduino. The excitation arm was used for variable-angle fluorescence, but could also be used for total internal reflection fluorescence. The objective was a high numerical aperture (1.45) oil-immersion type with 60x magnification. The microscope fluorescence filter cube (A, B, and C) provided 488 nm excitation and 493 nm long pass emission. The dual-view was configured for 2x magnification (by lenses F and M) giving a total of 120x magnification to the camera. Three lenses (D, F, and M) along with a rectangular slit (E) defined a rectangular image of the sample on the camera. The dual-view used two identical dichroics (G and L) along one band-stop filter (I) to define two spectral bands. The two colored images were steered using two movable mirrors (H and K). Filer J was not used. The microscope was also equipped with an Olympus ZDC2 continuous autofocus (not shown).

Channel	Dichroic Action	Spectral Band	Image Side	“Color”
0	Transmit	526 nm to 710 nm	Left	Red
1	Reflect	498 nm to 526 nm	Right	Green

Table 4.1. Definitions and terminology of the two channels of the microscope setup with homemade dual-view.

I used in this dissertation. The “homemade” dual-view was comprised of two achromatic lenses with 75 mm (Unknown manufacturer, 25 mm diameter) and 150 mm (Thorlabs AC508-150-A-ML) focal lengths, an adjustable rectangular slit, two Semrock FF526-Di01 (526 nm split) dichromatic mirrors, two front-silvered mirrors, and a 488 nm (Unknown manufacturer) centered notch-filter with about a 20 nm wide rejection band. This setup is shown in the bottom left corner of fig. 4.4 though for simplicity the 75 mm lens and the microscope tube lens are not shown. With the 60x objective and the 2x additional magnification of the dual-view the total magnification was 120x. The 488 nm notch-filter was used to remove excess laser light leaking through the RET493LP emission filter in the microscope filter cube.

With this setup the two spectral bands were defined by the dichroic mirrors which split at 526 nm, the long-pass emission filter and notch-filter which make the lower edge at about 498 nm, and the autofocus laser cleanup filter that cuts at 710 nm. Thus the definition of the two spectral bands were primarily dependent on the action of the dichroic mirrors. “Green” light reflected by the dichroic mirrors was from 498 nm to 526 nm and “red” light transmitted through the dichroic mirrors was from 526 nm to 710 nm. These spectral bands and the approximate OG488 spectra as passed through them are shown in fig. 4.5. The transmission band was focused on the left half of the camera and was termed channel 0 while the reflection band was focused on the right half of the camera and was termed channel 1. For an easy to read summary of this information see table 4.1.

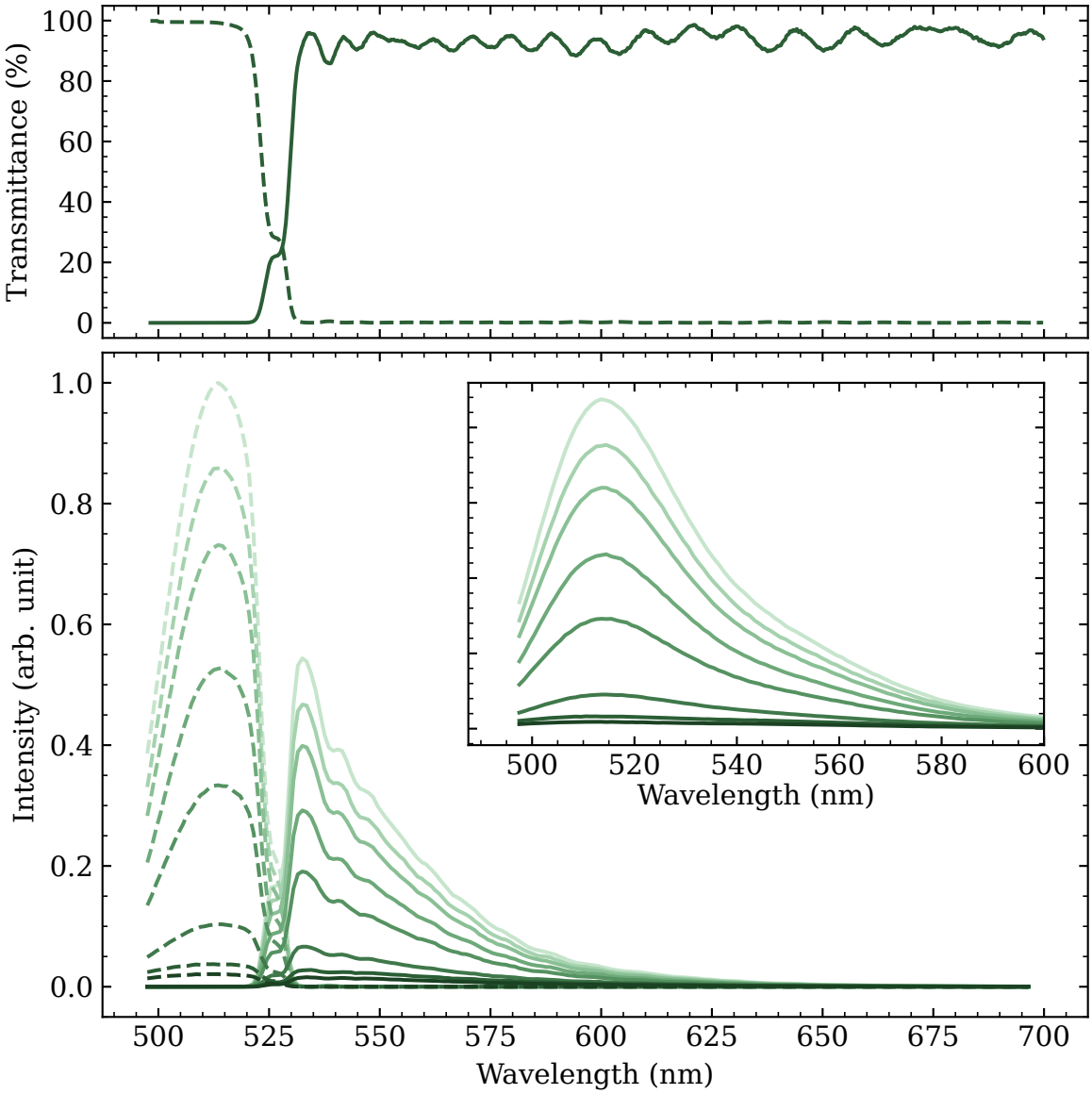

Figure 4.5. Approximate spectral bands of the homemade microscope dual-view (top panel) and the OG488 spectra as passed through these bands (bottom panel). The dashed lines (solid lines) indicate the transmittance of the dual-view or the approximate intensity of OG488 spectra as seen in right (left) half of image data and labeled as channel 1 (channel 0). The transmittance shown is approximate and only considers the double reflection or transmission through two Semrock FF526-Di01 dichromatic mirrors and ignores the transmittance of other mirrors, lenses, and filters. The inset shows the OG488 spectra which when multiplied by the transmittance (top panel) gives the spectra passed through the dual-view (bottom panel). The pH of the OG488 spectra displayed are, from dark to bright, 1.54, 2.7, 3.84, 4.53, 4.97, 5.45, 6.01, and 6.56.

The ORCA sCMOS camera had 2048×2048 pixel grid with $6.5\,\mu\text{m} \times 6.5\,\mu\text{m}$ pixels and a maximum full-frame frame rate of 100 Hz. The camera was used full-frame for all data and at the maximum frame rate for all droplet data. With the added magnification of the dual-view, the magnification was 120x and each camera pixel imaged $54.5\,\text{nm} \times 54.5\,\text{nm}$ in channel 0 and $55.6\,\text{nm} \times 55.6\,\text{nm}$ in channel 1 as per my measurements using images of a line grating. The ORCA camera had a well depth of about 30 000 electrons and a median readout noise of 1.0 electron at 100 frames per second. Therefore the camera had a dynamic range of about 30 000:1 necessitating that the data be stored at 16 bits per pixel. To fully utilize the 16 bits the electron count conversion was reported by the camera as 0.48 electron per count; I refer to this conversion by k. The camera also had a count offset in the images of about 100 which was subtracted from all data in my post-processing background subtraction. The ORCA's low readout noise, high dynamic range, fast framerate, and high quantum efficiency, $\Phi = 82\,\%$, were essential for the success of this method. Data can be converted from analog-to-digital units (ADUs) to incident photons flux by

$$\phi_{\text{q}} = \frac{100k \cdot \text{ADU}}{\Phi t_E}, \tag{4.1}$$

where the incident photon flux, ϕ_{q}, is measured in hertz, given that the exposure time, t_E, is in seconds.

4.2.3 Data Acquisition

Calibration data were acquired with the help of an Arduino which was used to externally trigger the camera and synchronously trigger the laser shutter. The external trigger circuit was programmed to acquire some images, typically 10, at the maximum framerate possible with external triggering followed by more images, typically 55, evenly spaced on a logarithmic scale up to the desired maximum duration. In external trigger mode the maximum frame rate of the ORCA camera is reduced, but is about 50 frames per second full-frame

when using a 10 ms exposure time. The logarithmically-spaced frames typically spanned 60 s. Therefore this method significantly reduced the number of images to be acquired (e.g., 65 instead of 6000) and gave sufficient data out to relatively long durations.

Droplet data were acquired in a streaming mode with the frame interval equal to the exposure time. These data were usually acquired with a 10 ms exposure time (100 frames per second [FPS]); however, 20 ms to 40 ms (50 FPS to 25 FPS) and exposure times were also briefly explored. I observed that greater than 20 ms (50 FPS) data were not useful due to the droplets diffusing too far between frames. 20 ms data were also of limited use due to droplet fluorescence photobleaching yielding fewer frames in the trajectories.

For 10 ms exposure time the camera was programmed to trigger the laser shutter. In this way the camera began its acquisition then approximately 10 ms later the shutter began opening such that the opening of the shutter could be seen in the acquired images. I observed that the first frame with the shutter fully opened was the 4th frame and so the first three frames were always discarded.

When the exposure time was greater than 10 ms the camera was unable to trigger the shutter. Therefore in this case a physical push button was used to trigger open the shutter (Uniblitz LS6ZM2) and the shutter driver (Uniblitz VCM-D1) would then trigger the camera, to start the acquisition, after the shutter was 80 % opened. The shutter had a transfer time, the time from closed to 80 % opened, of only 0.7 ms, and the camera begins acquisition only 87.7 µs after receiving a trigger. Therefore, the shutter would be fully opened at the start of the exposure with less than 0.8 ms prior illumination of the sample. Thus for data acquired with an exposure time greater than 10 ms no frames were discarded.

4.3 Particle Tracking and Image Processing

In general there were two types of data acquired for the microscopy measurements of pH and size: droplet data and calibration data. As an example, a movie of droplets is shown in fig. 4.6 and a movie of a calibration sample is shown in fig. 4.7. In these movies a linear contrast-stretch is applied to each half-image for every frame. The linear contrast-stretch method sets the black-point and white-point such that a desired percentage of the pixels are black or white after the contrast-stretch. After the black-point and white-point intensities are set all pixel intensities are linearly scaled between the black- and white-points.

A common feature of both these movies is that there are two half-images showing nearly the same region of the sample but with different spectra. Recall that I have defined the left half-image as channel 0 and the right half-image as channel 1. To analyze these data it is necessary to map regions of the right channel onto the same regions of the left channel, or vice versa. However, it can be seen that the right image is of a region slightly left of and slightly down of the left image. The half-images also appear to have some slight relative rotation and although not visible there is some relative scaling as well. Thus to obtain a mapping it is necessary to calculate an affine map which is a linear transformation that can include translation, scaling, rotation, shear, and mirroring. In my data only translation, scaling, rotation, and shear are necessary.

4.3.1 Particle Tracking

To calculate an affine map it is necessary to have a set of points in each half-image which are known to be the same location. Movies of droplets are ideal data for this since the droplets appear as bright, high-contrast points and these data are the data that need to be transformed. Thus it was necessary to find the droplet locations and trajectories. These actions are respectively called “localization” and “linking” or referred to together as “particle tracking”. One of the most common algorithms for particle tracking is known as the Crocker–

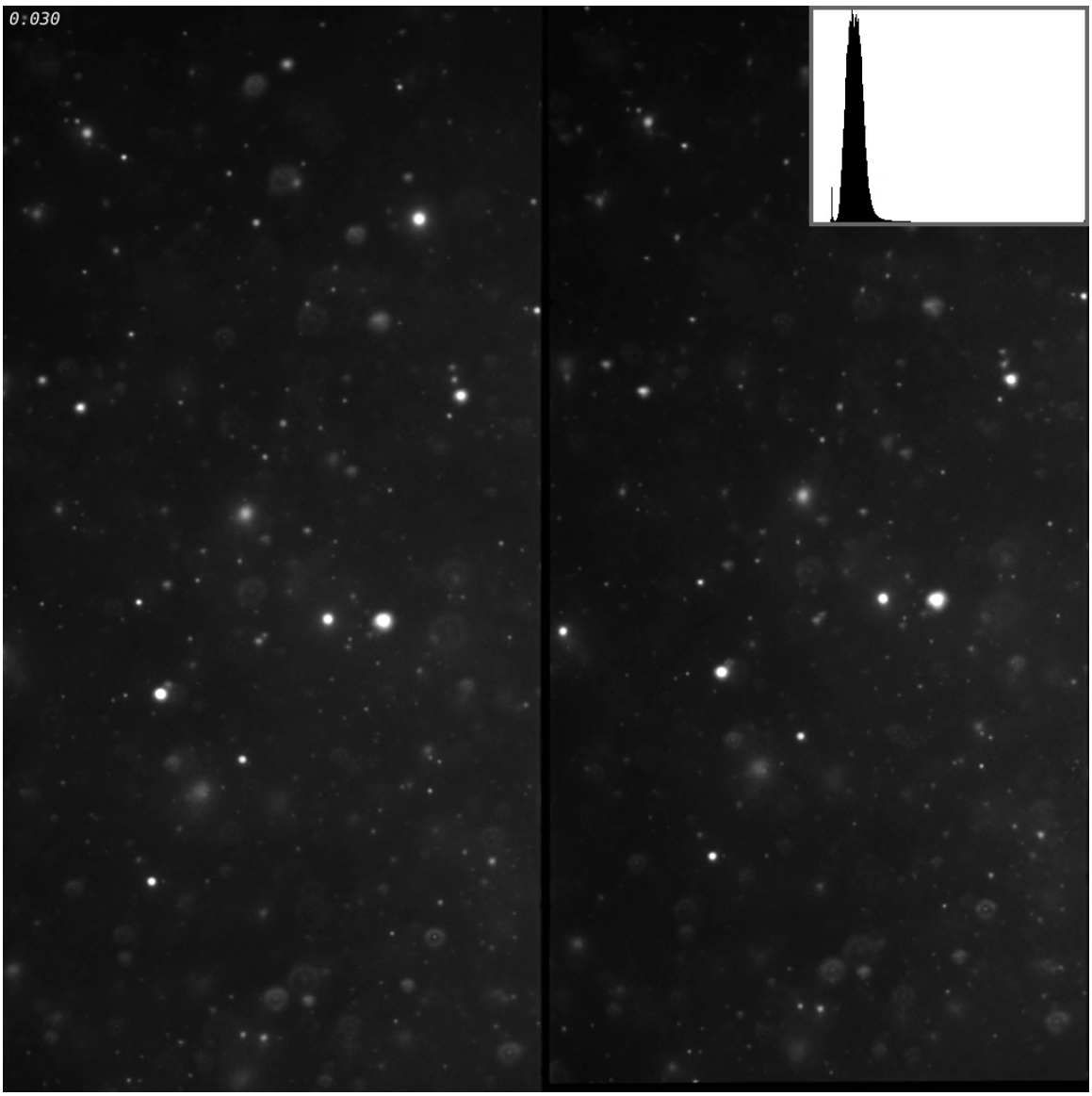

Figure 4.6. The image above shows the first frame of a movie of a fluorescent emulsion; for the whole movie see `droplets.mp4`. The emulsion aqueous phase contained 50 µmol L^{-1} OG488, 200 mmol L^{-1} tris, and 200 mmol L^{-1} ionic strength at pH = 7.76 before emulsification. The emulsion was prepared with 0.5 µL sample to 200 µL FC-40 containing 4 wt% surfactant giving a 1:400 sample:FC-40 ratio. The sample was sonicated for 10 s with the tip sonicator set to 70 % amplitude delivering 83 J of energy to the emulsion. All this with the sonicator tip submerged 2 mm. This sample was excited with $E_e \approx 14.6\,W\,cm^{-2}$ and observed at $z \approx 3.5$ µm from the coverslip surface. In the movie the frame time is shown in the upper left corner. The histogram is representative of the whole frame and has the same scaling in all frames. Each half-image has a linear contrast-stretch applied with 0.15 % pixels blacked-out and 0.05 % pixels whited-out as described on page 69.

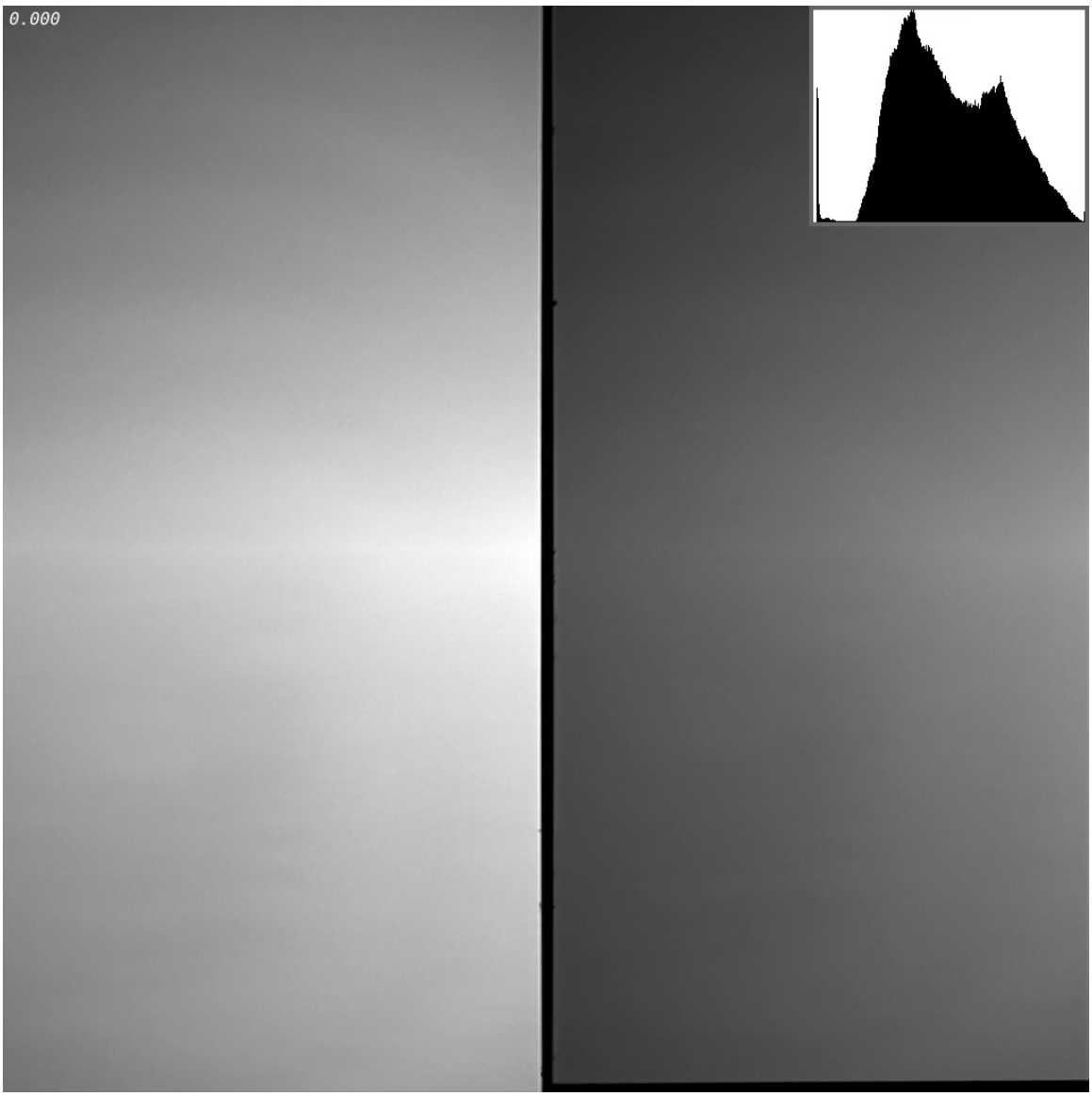

Figure 4.7. The image above shows the first frame of a movie of a calibration sample; for the whole movie see `calibrationData.mp4`. The sample contained 50 µmol L^{-1} OG488, 8 mmol L^{-1} citric acid, and 50 mmol L^{-1} ionic strength at pH = 3.52. The objective was focused at $z \approx 3.5$ µm above the coverslip. The camera exposure time was 10 ms. In the movie there 102 frames over 120 s (evenly spaced on a logarithmic scale) and the same exposure time for all frames. Data was taken with continuous laser illumination at $E_e \approx 173$ W cm^{-2} on the sample for the full 120 s. In the movie the frame time is shown in the upper left corner. The histogram is representative of the whole frame and has the same scaling in all frames. Each half-image has a linear contrast-stretch applied with 0.15 % pixels blacked-out and 0.05 % pixels whited-out as described on page 69.

Grier algorithm (originally described by Crocker and Grier, 1996) [55] and the modern implementation of this algorithm that I used was called `trackpy` [56] which was written in the Python programming language.

For localization the Crocker-Grier algorithm essentially calculates the two dimensional center of mass over pixelated circular regions around initial estimates of the particle locations:

$$\begin{bmatrix} \tilde{x}_0 \\ \tilde{y}_0 \end{bmatrix} = \begin{bmatrix} x_0 \\ y_0 \end{bmatrix} + \frac{1}{m_0} \sum_{i^2+j^2 \leq w^2} \begin{bmatrix} i \\ j \end{bmatrix} A(x_0 + i, y_0 + j), \tag{4.2}$$

where A is a two dimensional array representing an image, x_0 and y_0 are the initial locations, $\tilde{x}_0$ and $\tilde{y}_0$ are the refined particle locations, w is a characteristic radius, and

$$m_0 = \sum_{i^2+j^2 \leq w^2} A(x_0 + i, y_0 + j) \tag{4.3}$$

is the integrated brightness or integrated intensity of the particle. Initial particle locations are found by identifying local maxima within w after the image has been filtered through a bandpass method to reduce background noise and enhance image contrast. The bandpass method involves a low-pass Gaussian smoothing by convolving the image with a Gaussian kernel and a high-pass boxcar average to remove background modulation facilitating background subtraction. The local maxima are also only selected from the image's brightest pixels. Equation (4.2) is repeated until there is no longer any refinement.

For linking the Crocker-Grier algorithm maximizes the probability that an ensemble of N noninteracting, identical, Brownian particles with diffusion coefficient D have traveled a distance δ in time t:

$$P(\{\delta_i\}|t) = \left(\frac{1}{4\pi Dt}\right)^N \exp\left(-\sum_i^N \frac{\delta_i^2}{4Dt}\right). \tag{4.4}$$

Note that eq. (4.4) is a product of all the single Brownian particle probabilities and must be calculated for all possible combinations of particle displacements

Parameter	Description
`diameter`	Extent of a feature to be tracked; equal to $2w + 1$, in pixels, and must be odd
`minmass`	Reject features with an integrated brightness, m_0, below this value
`separation`	Minimum separation between features; brighter features are kept; typically set equal to `diameter` + 1
`noise_size`	Width of Gaussian blurring kernel, in pixels; typically set equal to 1
`smoothing_size`	Size of boxcar smoothing, in pixels; typically set equal to `diameter`
`threshold`	Clip pixels with intensity below this value in bandpass filtered image
`search_range`	Defines subnetwork size; equal to L, in pixels; value should be set based on frame interval, t and expected diffusion coefficient, D (if known)
`memory`	Maximum number of frames during which a feature can vanish, then reappear nearby and be considered the same particle; typically set to 0

Table 4.2. Selected input parameters and their descriptions for `trackpy` [56], the Python programming language implementation of the Crocker–Grier [55] particle tracking algorithm. Some parameter descriptions refer to eqs. (4.2) to (4.4) and their descriptions in the text.

between two successive frames. Also note that maximizing eq. (4.4) is equivalent to the simpler task of minimizing $\sum_i^N \delta_i^2$. Since this simpler calculation would still take $\mathcal{O}(N!)$ calculations the amount of work is simplified to $\mathcal{O}(N \ln N)$ by reducing the network size by considering only particles within a characteristic length L under the assumption that it is unlikely for a Brownian particle to diffuse beyond L.

From eqs. (4.2) and (4.4) we can see that there must be some input parameters to tune the tracking algorithm. A brief overview of some of the relevant parameters, with their names in the `trackpy` implementation, is given in table 4.2.

4.3.2 Affine Transformation

An affine transformation that scales, rotates, shears, and translates is given by

$$\begin{bmatrix} \tilde{x} \\ \tilde{y} \\ 1 \end{bmatrix} = \begin{bmatrix} s_x \cos(\theta) & -s_y \sin(\theta + \phi) & t_x \\ s_x \sin(\theta) & s_y \cos(\theta + \phi) & t_y \\ 0 & 0 & 1 \end{bmatrix} \begin{bmatrix} x \\ y \\ 1 \end{bmatrix}, \tag{4.5}$$

where (x, y) is a point in the original space, $(\tilde{x}, \tilde{y})$ is the corresponding point in the transformed space, s_x and s_y are the x and y scaling factors, θ is a counter-clockwise rotation, ϕ is a counter-clockwise shear, and t_x and t_y are the x and y translations. Such an affine map was used for all microscopy data to transform the data in channel 1 onto channel 0. The mapping was calculated every day for which data were taken using droplet data taken on the same day. If no droplet data were obtained on that day then images of 0.13 µm diameter fluorescent polystyrene beads were used instead; however, droplet data were preferred since the brightness in both channels was sufficient while the fluorescent beads were often too dim in one of the channels.

As discussed at the start of section 4.3.1 to calculate the affine map it is necessary to have a set of points in each half-frame that represent the same physical objects being observed. To obtain that set of points I used `trackpy` to localize droplets or beads in each half-image and then link the localized points as though the two half-images were actually two successive frames. This procedure was carried out over all frames in a movie to increase the number of points and the frame coverage. I then calculated the affine map given in eq. (4.5) using a Python image processing library called `scikit-image` [57]. To further increase the fidelity of the transform the image was split into a 4×2 grid and a separate transform was calculated for each split giving a total of eight transforms. This splitting helped accommodate for non-linear aberrations present in the images due to the optical setup.

Since this process required tuning of the tracking parameters, verification that the correct set of points are selected, and had to be performed each day

data were taken, I built a tool in Python to assist the process using `matplotlib` [58, 59], a Python plotting library. An image of the tool is shown in fig. 4.8. The tool shows a frame from the movie being used to calculate the transform and circles the regions selected by `trackpy`. Regions circled in red and labeled with an adjacent number in black have been found as a match in the two half-images and share the same ID number in each half-image. Regions circled in blue have no match in the other half-image. In this way it is easy to identify that the correct set of points has been determined. The radio buttons change how the images are shown: "Equalize" shows the images after histogram equalization, "Bandpass" shows the images after using the bandpass method of `trackpy`, and "Neither" uses linear contrast-stretching with 1 % blacked-out pixels and 0.05 % whited-out pixels; in all cases the images are color-mapped to further enhance the contrast. The sliders allow the user to change the tracking parameters or some offsets. Additionally all parameters can be specified on the command-line as well as some others like where the image split into two halves and what orientation, vertical or horizontal, to split.

After calculating the transform the channel 1 image is then warped onto the channel 0 using the `warp` method in `scikit-image`[57] with nearest-neighbor interpolation. In the warping step interpolation may be necessary due to the scaling, shearing, or rotation of the affine map. The default interpolation method of the `warp` method is bi-linear; however, this can cause banding in the images likely affects localization. Therefore I used nearest-neighbor interpolation instead such that blobs remain well defined.

Also when warping the two channels usually do not overlay perfectly, mostly due to translation or scaling, so there are edges with no data in the warped image. These edges were filled in with NaN (Not a Number) such that they could be easily removed in later analyses.[‡] Figure 4.9 shows the result of warping

[‡]NaN is not able to be stored in integer data. Since the camera stores image pixels as unsigned 16 bit integer data they had to be converted to floating point which was performed by the warping method.

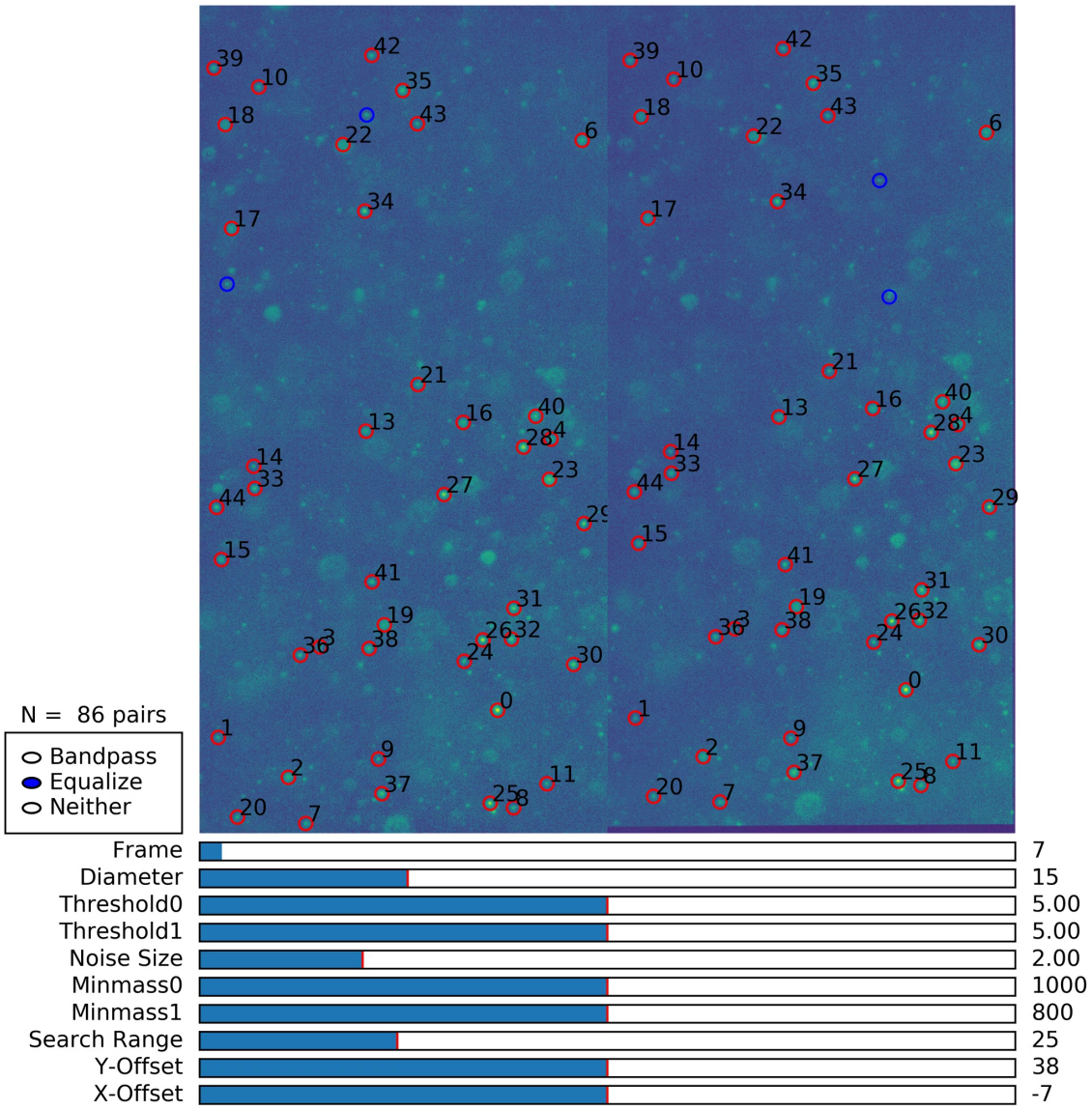

Figure 4.8. The image above shows the first frame of a video demonstration of a tool I built to assist in finding the appropriate affine transform; for the whole video see `transform.mp4`. Droplet data were being used to calculate the transform. Regions circled in red showing matching droplet pairs and regions circled in blue show identified droplets but with no match in the other half-image. Matching pairs share the same unique number in each half-image. Sliders change tracking parameters, current frame, or image offsets and the figure updates in real-time. Typically only the top 150 brightest pairs were kept and this was adjusted by a command-line option. This tool was built with `matplotlib` [58, 59], `trackpy` [56], `scikit-image` [57], and `scipy` [60].

where the channels are colored red and green, according to table 4.2, such that droplets appear yellow if the transformation is correct or if the transformation was poor droplets would have red or green fringes. Although the data presented in this way (as red and green) is useful in demonstrating the transformation and warping, and was a part of my transformation tool, for further analysis the data were not processed in this way. More details about how the data is handled will be given in the following sections.

4.4 Calibration

4.4.1 Photoinduced Effects

As stated in section 4.2.2, calibration data were measured over a long duration relative to the frame exposure time. The reason for this was to determine the optimal time after the laser exposure had begun to calculate the calibration. As can be seen in fig. 4.10(top) the photon flux of OG488 rapidly decays. This is due to photoinduced effects such as when a fluorophore in the excited singlet spin state undergoes an intersystem crossing to a long-lived, phosphorescent, excited triplet spin state or to some other non-radiative, long-lived state such as a free radical or a conformational change; and by photobleaching wherein the dye switches off by irreversible destruction [61–63]. As can be seen in fig. 4.10(bottom) the emission ratio also changes rapidly, but by only a small amount in comparison to the intensity changes. The emission ratio is also nearly flat at long times for pH less than about 4 and while the emission ratio does change at greater pH there is still a measurable difference in emission ratio up to about pH = 6. The data also shows that at early times it would be difficult to discern a pH = 6 sample from a pH = 7 sample.

The major concern about photoinduced effects is whether or not they are identical in droplets as they are in bulk. If the photodynamics are in any way different than they are in droplets the calibration would be less useful for determining pH in droplets. It is possible to tune the photophysics of dyes and

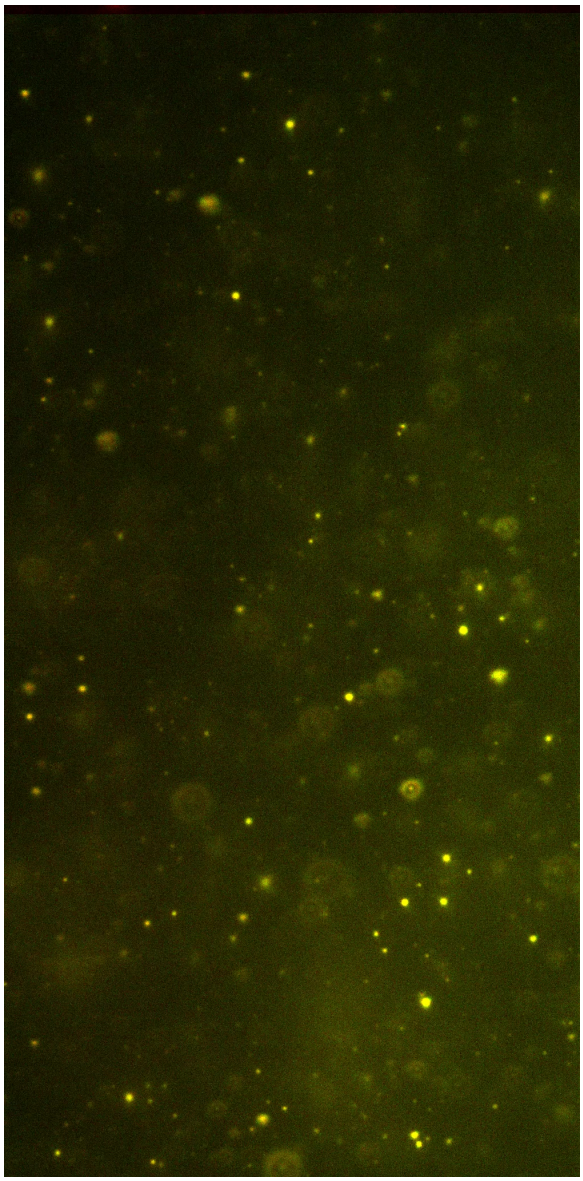

Figure 4.9. The image above shows the first frame of a movie of an emulsion where channel 1 has been warped onto channel 0 using eight affine transformations in a 4×2 grid; for the full movie of these data see `coloroverlay.mp4`. Channel 0 is colored red and channel 1 is colored green. Droplets with good overlay appear yellow while droplets with poor overlay would have red or green fringes. On close inspection the upper edge is only red since there was no channel 1 data for this region. Such regions were not used in any analysis.

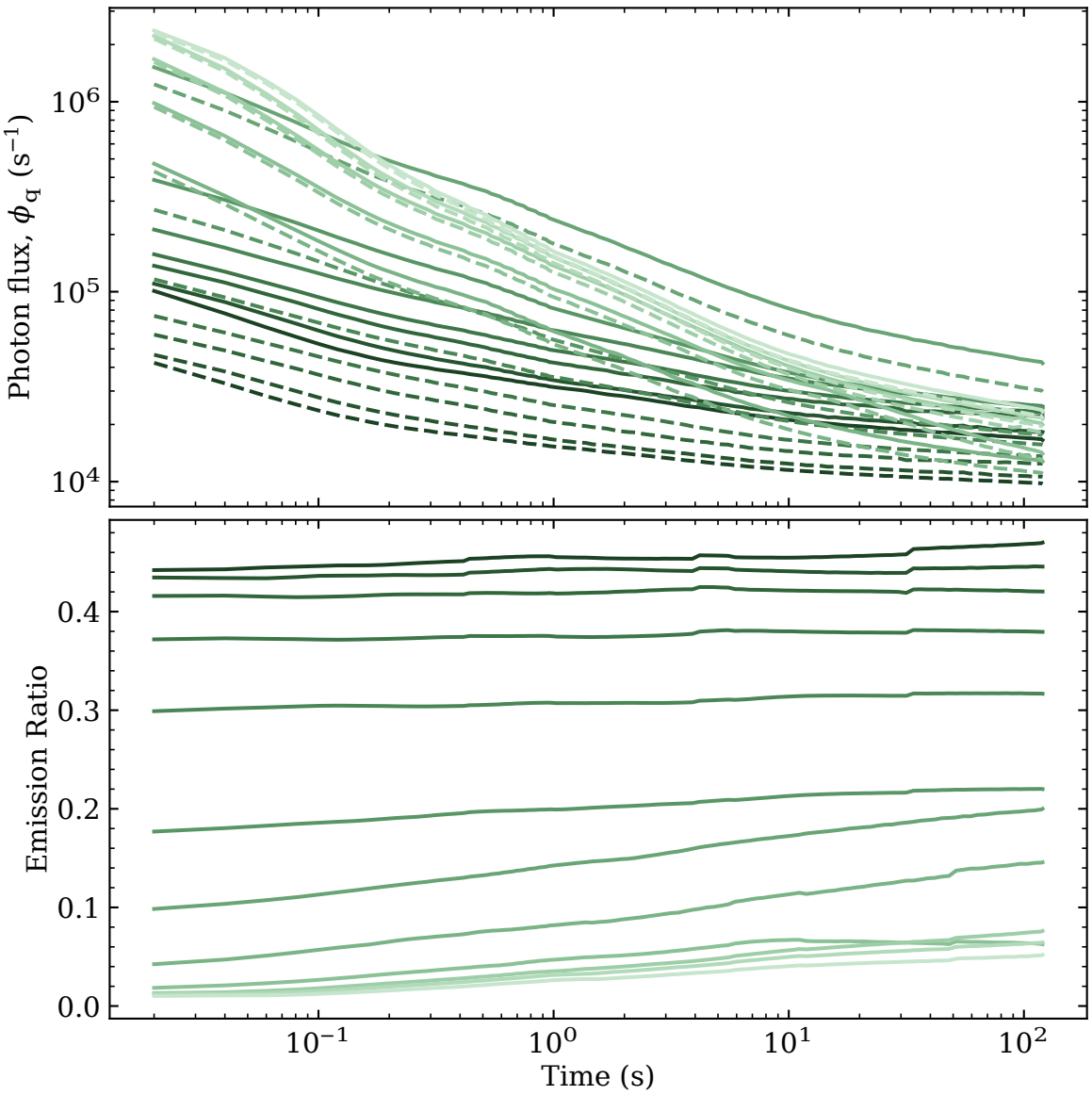

Figure 4.10. Average Photon flux (top) and average emission ratios (bottom) for a set of OG488 microscope calibration data. Averages were taken per frame over all pixels. Data are shown for 12 samples with pH = 1.55, 2.03, 2.53, 3.05, 3.52, 4.06, 4.54, 5.06, 5.56, 6.09, 6.58, and 7.01 which are colored from dark to bright respectively. Photon flux is shown for channel 0 (solid lines) and channel 1 (dashed lines). Sample with pH < 5 were exposed for 10 ms while samples with pH > 5 were exposed for 1.004 ms due to the much brighter fluorescence at higher pH. In all cases there were 102 frames acquired at identical times evenly space on a logarithmic scale. The objective was focused with $z \approx 3.5\,\mu m$ above the coverslip. Data was taken with continuous laser illumination at $E_e \approx 173\,W\,cm^{-2}$ on the sample for the full 120 s. The samples contained $50\,\mu mol\,L^{-1}$ OG488 and $8\,mmol\,L^{-1}$ citric acid at $50\,mmol\,L^{-1}$ ionic strength.

there have been many studies exploring methods to reduce dye blinking and reduce photobleaching by chemical methods that result in brighter and longer-lived dyes. However, it is not likely that these methods would be sufficient to make the emission ratio unchanging in time across all pH for both calibration data and droplets. Nonetheless, these methods may be of some benefit by reducing the dynamics of the emission ratio.

The basic concept behind tuning dye photophysics is through a reducing and oxidizing system (ROXS) in which the triplet state is reduced by a reducing agent to a radical state then an oxidizing agent rapidly oxidizes the radical to the ground state [62]. The success of these systems depend on other sample contents, especially pH, and are dye dependent such that a system that works for one dye or dye group may not for another.

Another concern is of molecular oxygen which when in its ground state (triplet O_2) it readily quenches fluorophores in excited singlet or triplet states. After quenching, oxygen enters a highly reactive singlet state that tends to cause dye photobleaching [64]. Therefore it can be beneficial to remove oxygen from the sample, thereby simplifying the task of the ROXS. One common O_2 scavenging system is with a combination of an enzyme, protocatechuate-3,4-dioxygenase (PCD), and its substrate, protocatechuic acid (PCA) [65, 66].

For stabilizing the OG488 emission ratios I tested two different ROXS with and without the PCA/PCD O_2 scavenging system. Trolox is a vitamin E analog that acts as a reducing agent and after dissolution in water it oxidizes to form a quinoid that behaves as an oxidizing agent thus together acting as ROXS [63, 67]. The other ROXS uses two separate chemicals: ascorbic acid as a reducing agent, and methylviologen (1,1’-dimethyl-4,4’-bipyridinium dichloride hydrate) as the oxidizing agent [68, 69]. I also tested samples with only ascorbic acid and only methylviologen.

I found that ascorbic acid at $1\,\mathrm{mmol\,L^{-1}}$ was most effective for calibration data at high pH and was better than no treatment; however, in droplet data every treatment I tested only made the emission ratio change more rapidly in

comparison to no treatment. I did not test any treatments for calibration data at lower pH where the results are likely to differ. These results are not surprising since these reducing and oxidizing and O_2 scavenging systems have all been tested on different types of dyes including cyanines, rhodamines, and oxazines; and I have not found any reports of tests on fluorescein and OG488 or other xanthenes. It is likely that tuning the photophysics of complex pH sensitive dyes is not possible with the current ROXS available across the entire pH range necessary for calibration. For example using one ROXS may help at high pH, but may hinder or not work at lower pH. It is also likely that stabilizing fluorescence in droplets is more challenging since FC-40 has a high solubility of oxygen and the amount of water in an emulsion is insufficient for an O_2 scavenging system to work effectively. Due to the complexity of tuning the photophysics of OG488, lack of prior work, and failure to improve stability in droplets I did not use any ROXS or O_2 scavenging system in any reported data.

It is possible to slightly mitigate photoinduced effects by using lower excitation irradiance and this can be done as long as there is significant emission intensity to resolve emission ratios well enough to determine pH. Although in bulk calibration data there is plenty of fluorescence and the excitation irradiance can be lowered, I had originally thought there would be insufficient fluorescence to obtain good droplet data. After realizing I could actually obtain useful data in droplets at lower excitation irradiance I obtained new calibrations and droplet data with about 10 times and 30 times lower excitation irradiance.

The effect of lower excitation irradiance is shown in fig. 4.11 where the pink-to-purple and green-to-brown curves were taken with $E_e \approx 173\,W\,cm^{-2}$ while the blue curves were taken with $E_e \approx 14.6\,W\,cm^{-2}$. At early times, represented by the brightest shades, it can be seen that the blue curves are shifted slightly down at low pH, shifted appreciably down at mid pH, and unshifted at high pH. Note that the pink and green curves lie directly on top of each other at early times. In this figure the curve brightness is indicative of the acquisition time after laser excitation has begun where the brightest shade is zero time,

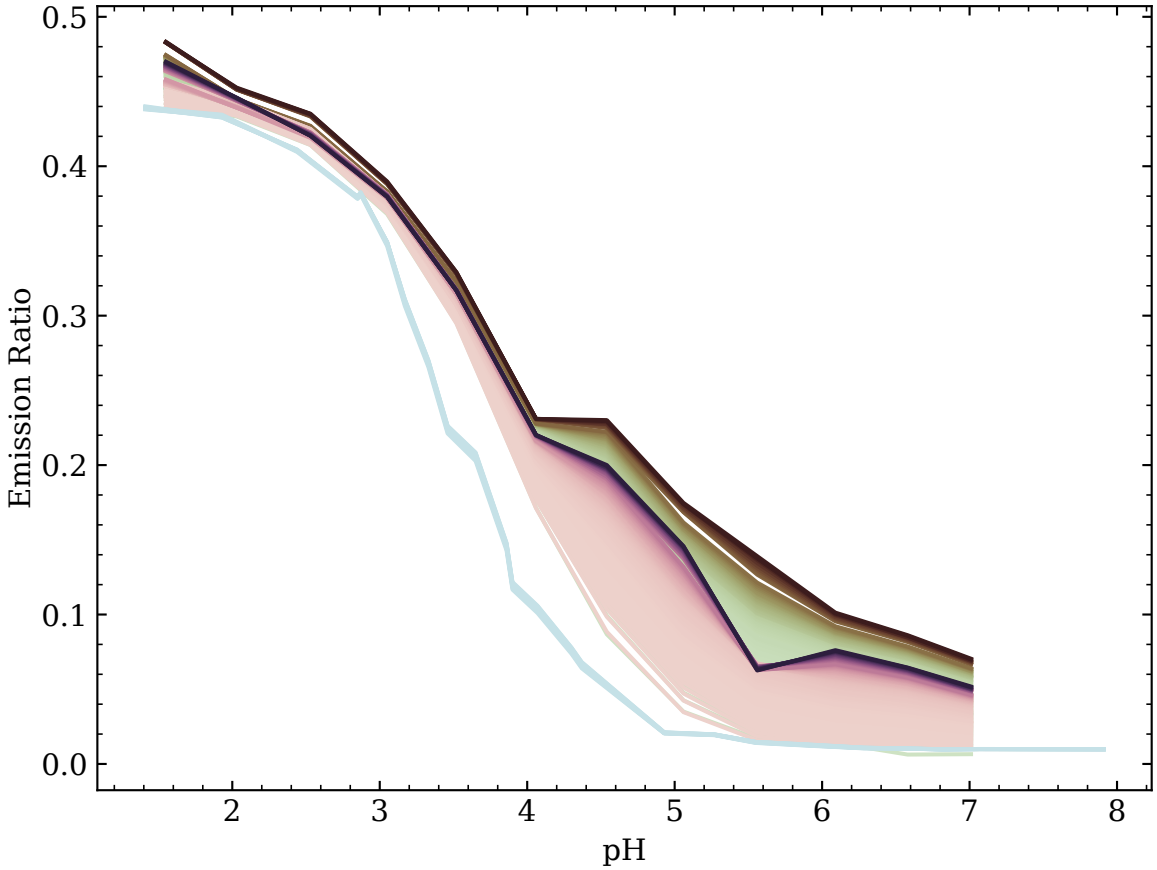

Figure 4.11. Average OG488 microscope calibration curves for three different calibrations at two different excitation irradiances and two different z focal depths. Averages were taken per frame over all pixels. The pink-to-purple curves show the same data shown in fig. 4.10(bottom) which was taken with $z \approx 3.5\,\mu\text{m}$, and $E_\text{e} \approx 173\,\text{W}\,\text{cm}^{-2}$ over 102 frames or 120 s. The green-to-brown curves show the same samples as the pink-to-purple curves observed under the same conditions except with $z \approx 20.1\,\mu\text{m}$ instead. The blue curves show another set of data with $50\,\mu\text{mol}\,\text{L}^{-1}$ OG488, $20\,\text{mmol}\,\text{L}^{-1}$ tris, and $200\,\text{mmol}\,\text{L}^{-1}$ ionic strength at pH = 1.41, 1.93, 2.44, 2.85, 2.87, 3.05, 3.17, 3.33, 3.46, 3.65, 3.86, 3.90, 4.07, 4.30, 4.37, 4.93, 5.27, 5.55, 5.89, 6.28, 6.82, 7.07, and 7.91 taken with $z \approx 3.5\,\mu\text{m}$ and $E_\text{e} \approx 14.6\,\text{W}\,\text{cm}^{-2}$ (about an order of magnitude lower than the pink-to-purple and green-to-brown curves) over 10 frames or 0.1 s; these blue curves are derived from averages of four acquisitions of each sample. In all cases the curves are shaded according to their acquisition time where zero time is the brightest shade and 120 s is the darkest darkest. Thus all curves share the same brightness at the same acquisition time irregardless of their color differences. At early times the pink curves and green curves lie directly on top of each other; it is only at late times where they differ. The blue curves do not have darker shades because of the lack of more data.

the darkest shade is 120 s later, and the brightness of curves in between varies linearly, with acquisition time, between these shades; however, since acquisition time is logarithmic the shades progress from bright to dark logarithmically. Since there are many more acquisitions at early times compared to late times there are more brighter shaded curves in this figure. Additionally all three calibrations (pink-to-purple, green-to-brown, and blue) share the same maximum and minimum brightness such that two curves which appear to have the same brightness also have the same acquisition time.

In the pink-to-purple and green-to-brown curves it can be seen that after a long exposure the calibration curves are shifted up. This effect is similar to the difference of low (blue curves) and high (pink-to-purple and green-to-brown curves) excitation irradiance, but in the opposite direction. Although I do not have data for lower excitation irradiance at longer duration my conjecture is that lower excitation irradiance at longer exposures would result in the same or similar curves as the high excitation irradiance at early exposures.

My original idea at the outset of determining a calibration was that I would select a time in the calibration that gave the most stable emission ratio with the lowest slope; however, after seeing the data I decided it was best to always use the earliest possible time since there was never a stable period and since the rate of change of the emission ratio is much more rapid in droplet data. Therefore the earliest acquisition time in the calibration is most likely to match the earliest acquisition time in the droplet data. In the earliest times all the fluorophore molecules are in their ground state while at later times the molecules are in a mixture of excited and dark states that is unlikely to be identical in bulk calibration as it is in droplets which have a small water pool, large surface area to interact with, and a huge oxygen bath.

4.4.2 Method

In total I obtained eleven OG488 microscope calibrations. Two of the calibrations were taken with 100 ms exposure time as a test and were not used.

The remaining nine calibrations were taken for different sample contents, z focal depths, or irradiance E_e. These calibrations were used for droplet data taken under exactly the same conditions and typically taken on the same date, but sometimes at a later date. All measurements used $50\,\mu mol\,L^{-1}$ OG488 and tris buffer or citric acid buffer with ionic strength ranging from $10\,mmol\,L^{-1}$ to $200\,mmol\,L^{-1}$. Tris was used at $20\,mmol\,L^{-1}$ to $200\,mmol\,L^{-1}$ and citric acid was used at $1\,mmol\,L^{-1}$ to $80\,mmol\,L^{-1}$. I do not see any changes in the calibrations by changes in sample contents. The important variables that change the calibration include the z focal depth, irradiance E_e, and the acquisition time after laser exposure as was discussed in the previous section. However, as can be seen in fig. 4.11 there is no difference between $z \approx 3.5\,\mu m$ and $z \approx 20.1\,\mu m$ at early times.

For every calibration, one or more background measurements were taken under identical conditions except that the background samples did not contain OG488. Thus for every acquisition time in the calibration data I had a corresponding background image. The background image at each acquisition time was smoothed with a Gaussian blurring kernel with $\sigma = 10\,px$ and subtracted pixel-by-pixel from the calibration data at that time. This must be done carefully ensuring that the integer values are clipped to zero if the result of subtraction would be less than zero; otherwise the negative values would be converted to a large positive integer near the upper end of the 16 bit unsigned integer range. Despite this careful background subtraction the background data were always uniform with only a few ADUs above the camera offset (100 ADUs) and had very little acquisition time dependence.

After background subtraction, an emission ratio image was calculated as per eq. (2.21) for every acquisition time and stored as a separate image stack. As per the discussion in the previous section the earliest usable time point was then selected from the separate emission ratio stacks to make a calibration file. The earliest usable time point was identified as the greater of either the first frame in which there was no overexposure of the image or the first frame in which the

shutter was fully opened depending on the shutter synchronization method. For calibrations acquired over 60 s to 120 s the first frame was overexposed so the second frame was used; this includes all of the higher irradiance calibrations. For the lower irradiance calibration I switched the acquisition method to continuous internally trigger with the ORCA performing shutter synchronization, the same as for droplet data. In this way the first frame in which the shutter is fully opened and the frame which I used for calibration was the fourth frame.

The final result for calibration is a single ratio image per pH, an example of which is shown in fig. 4.12. In this figure we can see that the calibration has a spatial dependence with a large change across the x axis and a small change across the y axis. Therefore to measure droplet pH it is necessary to lookup the correct set of (pH, R) pairs based on the droplet (x, y) positions. This per-pixel lookup must be done for every frame due to droplet diffusion. To prevent noise in the calibration data from giving rise to excessive noise in the droplet pH by this per-pixel lookup, I applied moderate Gaussian smoothing to the ratio images by convolving with a Gaussian blurring kernel with $\sigma_i = n_{i,\mathrm{px}}/100$ where i is the axis, x or y and $n_{i,\mathrm{px}}$ is the number of pixels in the ith axis such that the divisor, equal to 100 in this example, determines the amount of smoothing.

Since the calibration images have approximately $2048\,\mathrm{px} \times 1024\,\mathrm{px} \approx 2 \times 10^6\,\mathrm{px}$ I could not use the same high fidelity model for inverting the calibration data given by eqs. (3.5) and (3.16) as was used for the ensemble fluorimeter data. Using that technique requires fitting the model to data and visually verifying that the model produces a good fit. This cannot be easily done for two million datasets. Instead I used two million one dimensional, linear, interpolating splines that were calculated on demand. Linear interpolating splines, unlike cubic smoothing splines, do not ever produce large outlying values so do not need to be checked for validity before use. Any ratio which was out of the range of the spline was discarded and not included in further analysis.

I also tested another method of preventing excessive noise from the calibration per-pixel lookup. This method compiled the calibration data with no

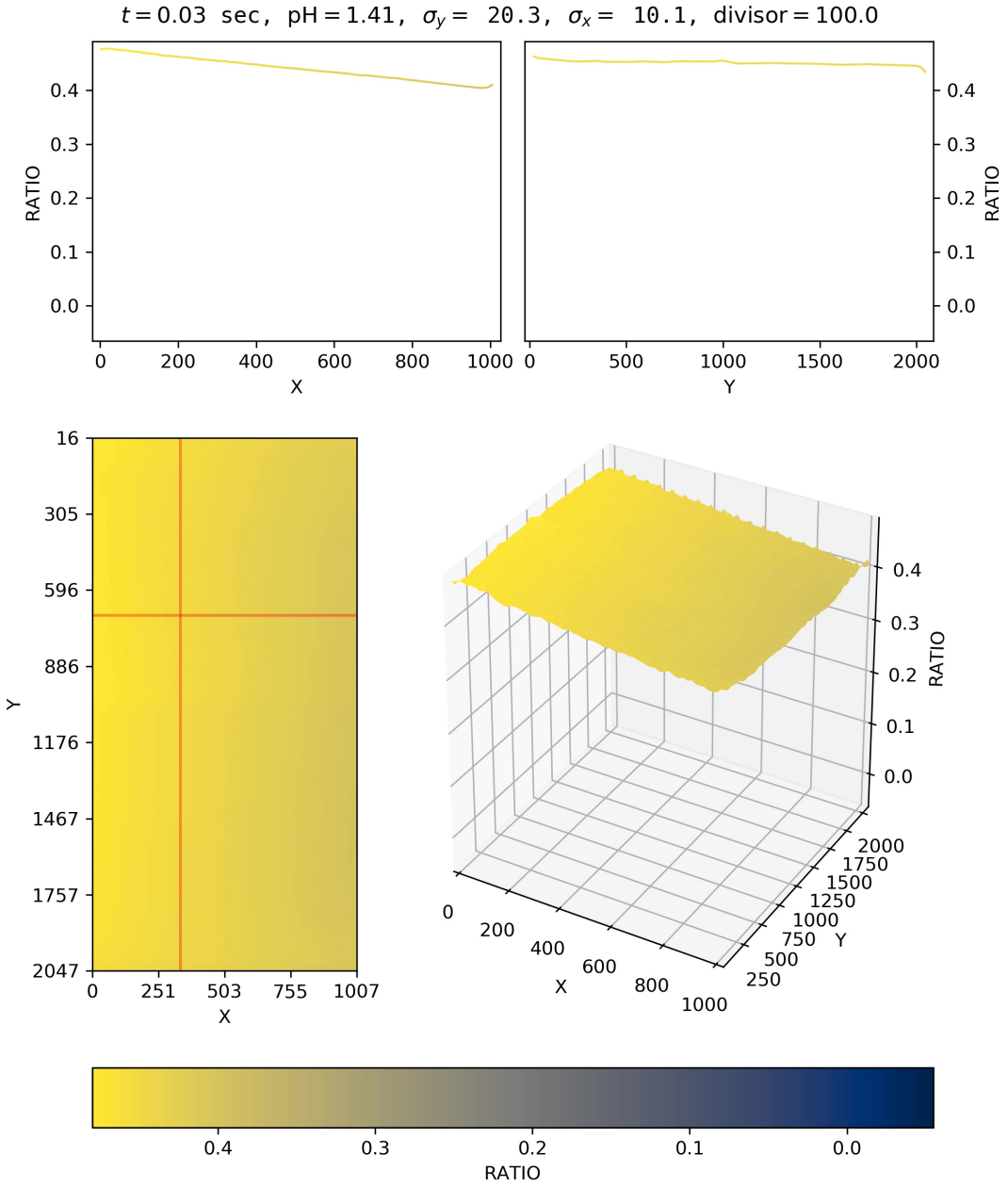

Figure 4.12. The image above shows the first frame of a video showing the microscope OG488 calibration; for the full video see `microscopeCal.mp4`. The image shows the calibration emission ratio as a function of position for pH = 1.41 and for $E_e \approx 14.6\,\mathrm{W\,cm^{-2}}$ at $z \approx 3.5\,\mu\mathrm{m}$. The full video shows the ratio image of every pH in the calibration where the pH are indicated on the top line. Data shown are the same as the blue curves in fig. 4.11 using only the acquisition time shown in the upper left corner (seconds). σ_y and σ_x determine the amount of Gaussian smoothing applied to the data and are calculated by the image dimensions and the divisor. In the video all frames and all plots share the same color bar shown on the bottom.

smoothing. When the per-pixel lookup was performed the calibration emission ratios were determined as averages over masked regions of the calibration ratio images where the mask used was identical to what is used in the particle tracking algorithm. This method produced nearly identical results to the former method so the former method was used as the data had already been processed using that method.

4.5 Droplet Analysis

After acquiring droplet data as described in section 4.2.3 the data were affine transformed as discussed in section 4.3.2 and then the data were stored as stacks with dimensions $(N, 2, h, w)$ where N is the number of acquisitions in the stack, 2 is the number of channels, h is the height of the frame (typically 2048), and w is the width of the frame (typically between 1000 and 1024). Then the transformed data were used for particle tracking, first by summing (or equivalently averaging) the two channels of each stack giving (N, h, w) shaped stacks, then by applying the algorithm given in section 4.3.1 on each frame of each stack.

For the particle tracking parameters (see table 4.2) I set `diameter` = 15, `minmass` = 180, `separation` = 16, and `search_range` was set to three times the expected Brownian diffusion "step-size" for the minimum expected droplet size:

$$\texttt{search\_range} = 3\frac{\sqrt{4Dt}}{a}, \tag{4.6}$$

where D is the diffusion coefficient of the droplet in FC-40, t is the time between two successive frames of the image stack, and $a = 54.5\,\mathrm{nm\,px^{-1}}$ is the camera resolution. The "step-size" will be explained in the next section. To calculate the diffusion coefficient I used the Stokes–Einstein equation [70]:

$$D = \frac{k_\mathrm{B}T}{6\pi\eta r}, \tag{4.7}$$

where k_B is the Boltzmann constant, T is the absolute temperature, η is the dynamic viscosity of the medium (0.0041 Pa s for FC-40), and r is the minimum expected droplet radius which I set to 35 nm. The remaining tracking parameters were left at their default values: `noise_size` = 1, `smothing_size` = `diameter`, `threshold` = 1, and `memory` = 0.

After localization, the features were filtered out based on location and eccentricity, ϵ. The eccentricity of a perfect circle is zero while an ellipse has an eccentricity between zero and one. Features with $\epsilon > 0.3$ were removed before tracking since droplets are expected to be spherical (circular in 2D) and larger eccentricities could be aggregates of droplets, out of focus droplets, two droplets near each other but not aggregated, the Airy disk of a nearby bright droplet, or any combination thereof. In the summed frames there are often sharp edges due to the misalignment of the two channels. These sharp edges have locally high contrast and are misidentified by the tracking algorithm as features. Features near these edges, typically about 20 px, are removed before tracking.

Finally, after tracking only trajectories lasting at least 50 frames were used to get an accurate estimate of the droplet size. An example of the tracking results for droplets is shown in figs. 4.13 and 4.14. In the next two sections I will discuss how I obtain the size and the pH of droplets from these trajectories.

4.5.1 Size Determination

In these experiments droplets undergo simple, free Brownian diffusion thus are described by a random walk wherein the transition probability that a particle originally at location $\boldsymbol{r}_0$ is found at location $\boldsymbol{r}$ after time t is given by [71, 72]:

$$P(\boldsymbol{r}|\boldsymbol{r}_0, t) = \frac{1}{(2d\pi Dt)^{d/2}} \exp\left(\frac{-(|\boldsymbol{r} - \boldsymbol{r}_0|)^2}{2dDt}\right), \tag{4.8}$$

where for spherical particles D is given by the Stokes–Einstein equation 4.7, and d is the number of dimensions which was always 2 for my data. This transition

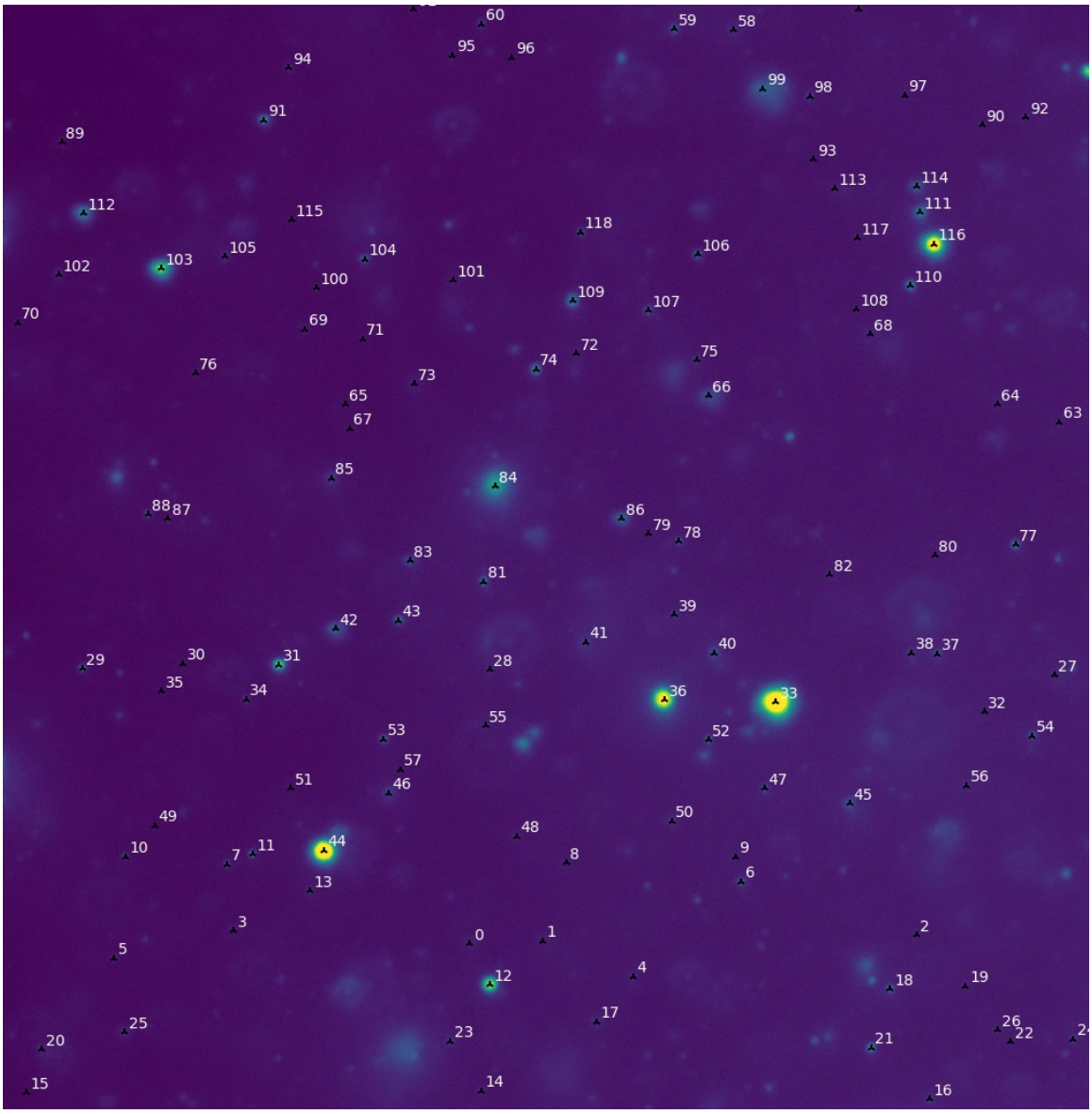

Figure 4.13. Localized and tracked droplet data for the emulsion shown in fig. 4.6. The localized centers are indicated by unique particle identification numbers and black markers. The transformed and summed frames are shown with a colormap to enhance contrast. Only a centrally cropped region half the height and equal to the width of channel 0 is shown. For the full movie for this sample see `dotframes.mp4`.

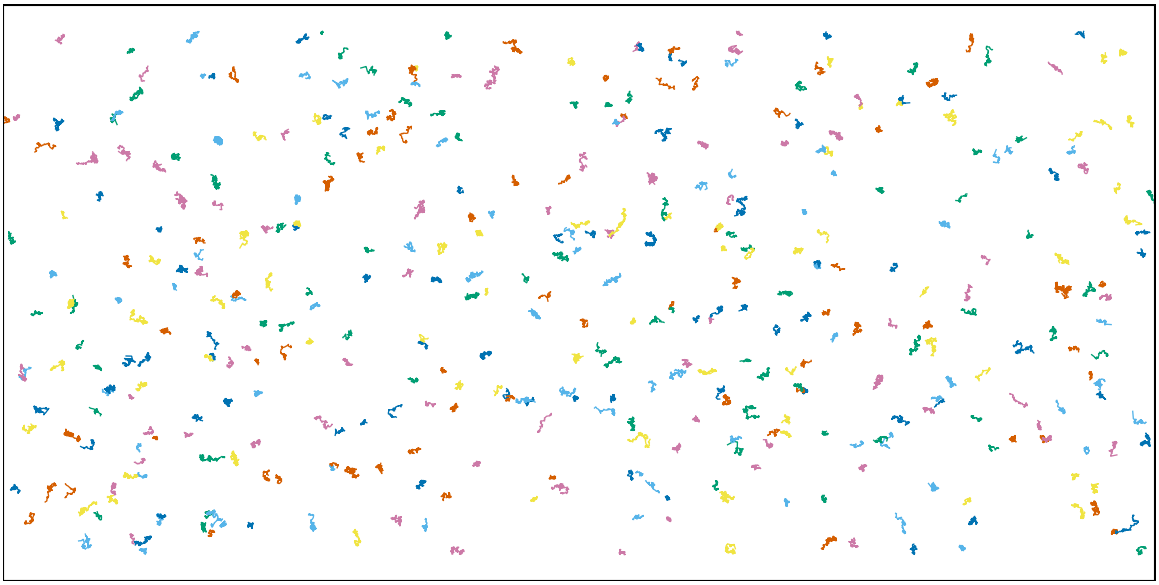

Figure 4.14. Droplet trajectories for data shown in fig. 4.6 and fig. 4.13. Trajectories are shown for the entire frame, not just for the centrally cropped region shown in fig. 4.13. The frame is rotated only for presentation purposes.

probability is valid as long as $2dDt \ll L^d$ where L is a characteristic dimension of the space available for diffusion. In the data I have observed the droplet radii were always greater than 10 nm and t was usually 0.01 s (the frame interval time) then the maximum value for $2dDt$ was about 0.2 µm^2. The median droplet size in my experiments was about 146 nm giving $2dDt = 0.015\,\mu m^2$. Since the closest focal plane I have observed data at was 3.5 µm it is likely that $2dDt \ll L^2$ was always valid therefore I can assume free diffusion of the droplets.

While the first moment of Brownian diffusion vanishes, the second moment is known as the MSD:

$$\rho(t) = \int (\boldsymbol{r}(t) - \boldsymbol{r}_0) P(\boldsymbol{r}|\boldsymbol{r}_0, t) \mathrm{d}\boldsymbol{r} = 2dDt. \tag{4.9}$$

This quantity can be readily measured in the droplet data since Brownian diffusion is a stationary ergodic process then the ensemble average can be computed as a time average of a single particle trajectory as [71]

$$\begin{aligned}\rho(t) &= \langle |\boldsymbol{r}(t) - \boldsymbol{r}_0|^2 \rangle_{\text{Av}} \\ &= \int |\boldsymbol{r}(t+t') - \boldsymbol{r}(t')|^2 \mathrm{d}t'.\end{aligned} \tag{4.10}$$

It follows from eq. (4.10) that the MSD along any given direction, say the x direction, is given by

$$\rho(t) = \langle (x(t) - x_0)^2 \rangle_{\text{Av}} = 2Dt. \tag{4.11}$$

Therefore the diffusion "step-size" for a time increment t is given by $\sqrt{2dDt}$ which is what I used in calculating the `search_range` [see eq. (4.6)]. However, the more accurate definition is that the diffusion steps are drawn, independently for each dimension, from the $\mathcal{N}(0, 2Dt)$ normal distribution. It is the latter definition that I used for the simulated data I will discuss briefly.

For a discrete time trajectory, like the droplet trajectories, with N frames there are $N(N-1)/2$ nontrivial forward displacements such that the MSD can be calculated as [73]

$$\rho_n = \frac{1}{N-n} \sum_{i=1}^{N-n} (\boldsymbol{r}_{i+n} - \boldsymbol{r}_i)^2, \; n = 1, \ldots, N-1, \tag{4.12}$$

where the displacements have duration nt know as time lags. Equation (4.12) was used for calculating the MSD in all data using a function from the `trackpy` library.

Now given the MSD of a trajectory calculated at all possible time lags it is tempting to think we can fit the data to a line and get the diffusion coefficient from the slope of the line ($= 2dD$); however, there are two issues with this assumption: (1) the MSD becomes more noisy as the time lag increases due to the fewer sets of points available to calculate the MSD and (2) due to localization uncertainty present in real data, the finite camera exposure time (t_E), and the finite frame interval (t). The implication of (1) is that it is not trivial to choose the maximum time lag to be used in the fit, and the implications of (2) are that

there is a non-zero y intercept which depends on the diffusion coefficient and there is additional noise added to the MSD curve. The only time it would be valid to assume the slope of the MSD curve is $2dD$ would be in the limit of infinitesimal t_E and t with an infinitely long trajectory $N \to \infty$ [73, 74].

To demonstrate these effects I performed a Monte Carlo simulation of Brownian diffusion with localization uncertainty in two dimensions. Each dimension follows $x_{i+1} = x_i + \Delta x_i + \eta_i$ where $\Delta x_i \sim \mathcal{N}(0, 2Dt)$, where $x_0 = 0$, and where $\eta_i \sim \mathcal{N}(0, \sigma^2)$ is known as the localization uncertainty. In this simulation I used the expected diffusion coefficient for a 100 nm radius droplet in FC-40 at 22 °C using eq. (4.7), $D = 0.53\,\mu\text{m}^2/\text{sec}$, the frame interval or time step, $t = 0.01$ s, and an exaggerated localization uncertainty of twice the diffusion step-size, equal to 0.205 µm, to better demonstrate the effect of localization uncertainty. I generated one trajectory with $N = 1 \times 10^4$ steps and calculated the mean displacements, $\langle x \rangle$, one-dimensional MSDs, $\langle x^2 \rangle$, and two-dimensional MSDs, ρ, for subtrajectories from the first step to the Mth step with M = 10, 20, 30, 40, 50, 60, 70, 80, 90, 100, 300, 500, 1000, and 10 000. The results of this simulation are shown in fig. 4.15 where only time lags up to 1 s are shown so that the MSDs from shorter subtrajectories can be seen.

In this figure brighter shades represent MSDs from shorter subtrajectories, the left column shows the MSDs from subtrajectories without localization uncertainty while the right column shows MSDs from the same subtrajectories with added localization uncertainty. It can be seen that the average displacements for short subtrajectories heavily deviate from zero while for long subtrajectories tend to zero. This means that the time average of a short trajectory is not a good estimation of the ensemble average. In the 1D and 2D MSDs it can be seen that as time lag increases the MSDs from the shorter subtrajectories often rapidly deviate from the MSD from the full length trajectory. While the MSD from the full length trajectory is a good approximation of the ideal MSD from an infinitely long trajectory (a straight line with slope $2dD$, the MSDs from the short subtrajectories would give a bad approximation of the slope and thus the

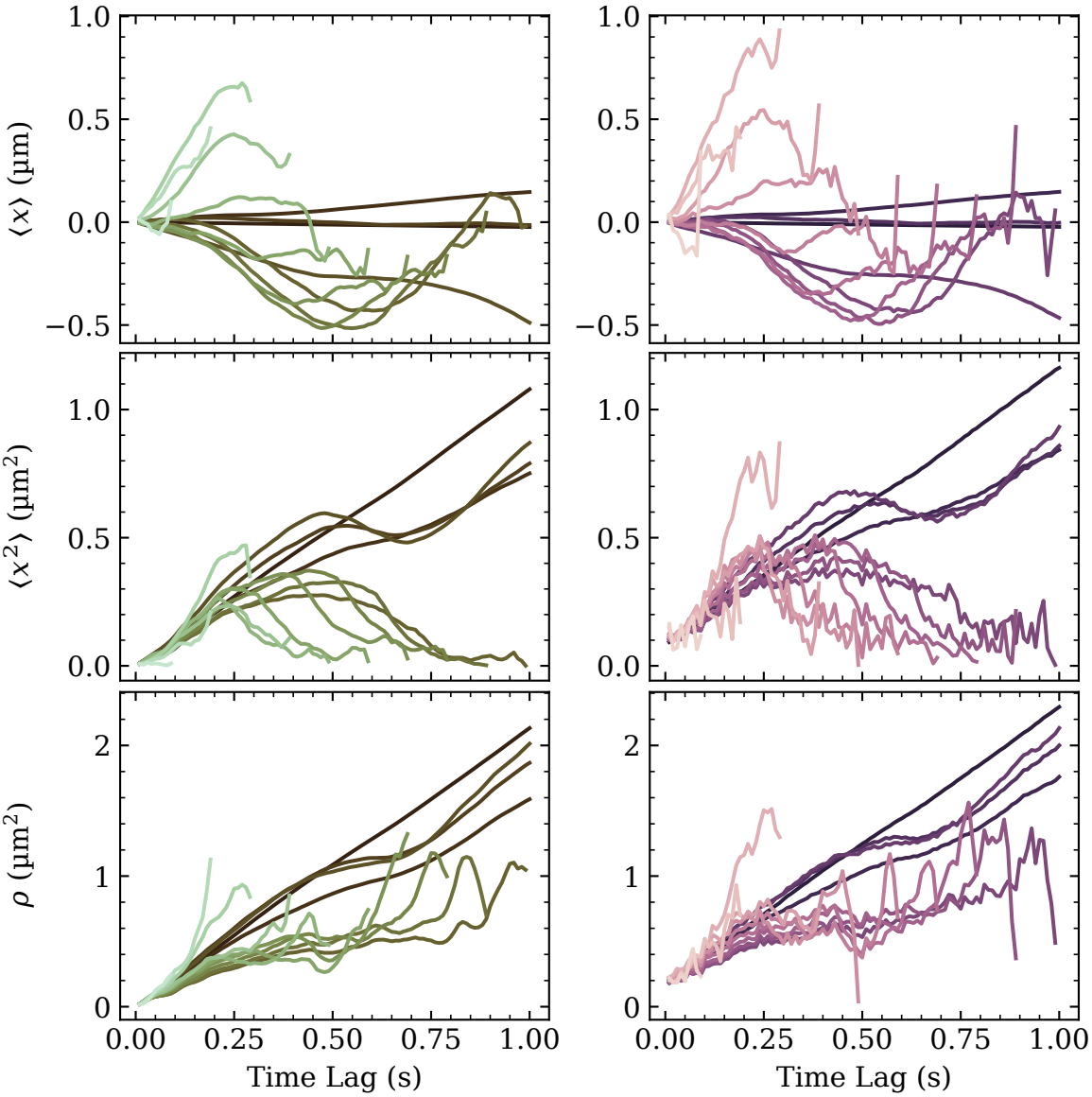

Figure 4.15. MSDs from subtrajectories of a simulated trajectory exhibiting Brownian diffusion with localization uncertainty of zero (left column) or 205 nm (right column). In each panel 14 subtrajectories of a $N = 10\,000$ step random walk are shown. The subtrajectories are taken from the first step to the Mth step where $M = 10$, 20, 30, 40, 50, 60, 70, 80, 90, 100, 300, 500, 1000, and 10 000 and shaded from bright to dark. The brighter shaded, and shorter, subtrajectories are shown on top of the darker shaded, and longer, subtrajectories. The top row shows the mean displacements in the x direction, the middle row shows the mean square displacements in the x direction, and the bottom row shows the two-dimensional mean square displacements. The mean square displacements in the y direction are not shown.

diffusion coefficient if all time lags were used in a line fit. However, if you pay careful attention to the early times of the MSDs from the short subtrajectories it can be seen that if the first few time lags were used in a line fit, they would give a much better approximation of the slope and thus the diffusion coefficient. Of course this is all manifest because larger time lags have fewer intervals to average while the first two time lags have the most intervals in the average, so produce the most reliable slope.

When localization uncertainty is added (right column) the situation changes. First notice that the localization uncertainty introduces a y intercept. This y intercept is actually dependent on the diffusion coefficient because of motion blur due to particle diffusion during the finite exposure time. Due to the motion blur the weighted average position during the exposure is what is actually measured [75]. The motion blur also effectively broadens the microscope point-spread function (PSF) due to the diffusion about the average position throughout the exposure [73]. Despite the y intercept the slope is still equal to $2dD$.

In the simulation with localization uncertainty the MSD for the first two time lags are dominated by noise so the number of time lags to use that would give the best estimate of the diffusion coefficient is more than the first two. It can also be seen that with or without localization uncertainty the two-dimensional MSD has less fluctuation than the one-dimensional MSD such that a better result would be obtained by fitting the two-dimensional MSD.

To fit the MSDs I used an optimized least-squares fit method developed by Michalet [73] and later further developed by Michalet and Berglund [74]. In this method the MSD is fit to a line

$$\rho(t) = A + Bt \tag{4.13}$$

$$A = 2d(\sigma^2 - 2RDt) \tag{4.14}$$

$$B = 2dD, \tag{4.15}$$

where σ^2 is the called the *dynamic localization uncertainty* and is what was used in the simulation, and R is the camera blur coefficient (equal to $1/6$ when $t_E = t$. The dynamic localization is related to the static localization uncertainty, σ_0^2 by:

$$\sigma^2 = \sigma_0^2 \left(1 + \frac{Dt_E}{s_0^2}\right), \tag{4.16}$$

where s_0^2 is the variance of a Gaussian approximation of the microscope PSF or any other more complex model of the PSF. If using the Gaussian approximation then [76]

$$s_0 \approx 0.21 \frac{\lambda_{\text{ex}}}{\text{NA}}, \tag{4.17}$$

where NA is the numerical aperture of the objective. The static localization uncertainty can be estimated using [77]

$$\sigma_0^2 = \frac{s_0^2 + a^2/12}{N} + \frac{4\pi s_0^3 b^2}{aN^2}, \tag{4.18}$$

where a is the effective pixel width, b^2 is the variance of the background noise, and N is the total number of photons in the spot.

The next step in the optimized least-squares fit method is to calculate the reduced square localization uncertainty:

$$x = \frac{\sigma^2}{Dt} - 2R. \tag{4.19}$$

The value of x determines how well the fit will perform in determining D and σ^2. When x is large, σ^2 is well defined while the error on D diverges; for small x the opposite is true. After an initial fit of the MSD to 10 % of the time lags and calculation of x, the optimum number of points for fitting the MSD can be determined using heuristic formulas $p_{\text{min}}^{(A)}(x, N)$ and $p_{\text{min}}^{(B)}(x, N)$, where N is the trajectory length. These ad hoc formulas were determined by Michalet and Berglund [74] as a fit to their simulation results. For the formulas and

full algorithm details please refer to [74] or my Python implementation of their algorithm in appendix A. Note that since their simulations and calculations were on unbroken trajectories with no missing frames, they may not be valid for trajectories with missing frames. Therefore I always set the tracking parameter `memory` to zero which gives only unbroken trajectories.

After fitting the values of D and σ^2 and the relative error on them, `errD` = S(D)/D and `errS2` = S(σ^2)/σ^2, are readily determined using formula from [74]. As an example I have analyzed the simulated trajectories in fig. 4.15 and shown the results in table 4.3. It can be seen that without localization uncertainty (top table) the estimates for D and r are very close to their nominal values, only the first two time lags are necessary to get the best fit, and it is impossible to determine the error on σ^2 in all but one of the subtrajectories. And with localization uncertainty the estimate for σ^2 is good, the optimum number of parameters is greater than two in all cases, and the estimates for D and r are unreliable up until a subtrajectory of length 60 or 70 frames.

Finally as I discussed in section 4.5 for my droplet data I only used droplets which had trajectories with at least 50 frames. From these trajectories I calculated the median reduced square localization uncertainty was $x_{\text{med}} = 1.8 \times 10^{-4}$, and in most cases only the first two time lags are used for fitting. With such a low value of x and for a droplet with a 50 frame trajectory, I expect that the measurement of its size would be within 25 % of the true size 70 % of the time based on the success map in [74, see fig. 3.] for the OLSF method. However, in most cases I have a trajectory longer than 50 frames so the size measurements were generally better than this. A sample plot of the MSDs and a histogram of the radii from their fits are shown for all tracked droplets in a single emulsion in fig. 4.16. This sample is one of 424 total droplet videos acquired and analyzed. Based on all 424 videos the 0, 25, 50, 75, and 98.5 percentiles of the relative error on the radius measurements, $S(r)/r$, were 0.078, 0.173, 0.214, 0.248, and 0.498, respectively.

N	D	errD	sig2	errS2	r	sigr	pminA	pminB
10	0.68	0.62	0.001	inf	77.7	48.2	2	2
20	0.67	0.41	0.002	inf	78.4	32.3	2	2
30	0.66	0.33	0.001	inf	80.4	26.4	2	2
40	0.64	0.28	0.001	inf	81.7	23.1	2	2
50	0.64	0.25	0.001	inf	81.7	20.5	2	2
60	0.70	0.23	0.001	inf	75.0	17.1	2	2
70	0.63	0.21	0.001	inf	83.2	17.5	2	2
80	0.61	0.20	0.001	inf	86.2	16.9	2	2
90	0.58	0.18	0.001	inf	90.4	16.7	2	2
100	0.63	0.18	0.001	inf	83.0	14.5	2	2
300	0.57	0.10	0.002	inf	92.8	9.3	2	2
500	0.53	0.08	0.002	inf	100.0	7.8	2	2
1000	0.50	0.05	0.002	0.095	105.2	5.8	2	2
10000	0.53	0.02	0.002	inf	99.2	1.7	2	2

N	D	errD	sig2	errS2	r	sigr	pminA	pminB
10	0.29	2.05	0.044	0.470	182.6	373.9	5	5
20	0.54	0.88	0.044	0.315	98.4	86.8	6	6
30	0.31	0.87	0.036	0.260	168.9	147.2	6	7
40	0.47	0.55	0.036	0.222	112.2	61.2	6	6
50	0.36	0.61	0.037	0.202	145.5	89.1	6	7
60	0.46	0.51	0.045	0.176	115.4	59.1	7	7
70	0.64	0.38	0.040	0.170	82.8	31.2	5	5
80	0.59	0.36	0.042	0.156	89.3	32.3	6	6
90	0.52	0.36	0.044	0.143	101.9	36.9	6	6
100	0.53	0.34	0.043	0.137	99.5	33.4	6	6
300	0.42	0.20	0.045	0.075	126.6	25.7	7	7
500	0.49	0.15	0.044	0.060	107.3	15.7	6	6
1000	0.49	0.11	0.042	0.042	108.0	11.4	6	6
10000	0.51	0.03	0.045	0.013	104.1	3.5	6	6

Table 4.3. Results of fits to MSDs from simulation data in fig. 4.15 using the MSD code given in appendix A. The upper table shows the results of fitting MSDs without localization uncertainty and the lower table with localization uncertainty. `N` is the subtrajectory length, `D` is the diffusion coefficient, `r` is the radius, `sig2` = σ^2 is the dynamic localization error, `errD` and `errS2` are the relative uncertainty on the diffusion coefficient and localization uncertainty, and `pminA` and `pminB` give the optimum number of fitting points used to determine the y intercept and slope respectively. The values modeled in the simulation were `r` = 100 nm, `D` = 0.53 µm^2/sec, and `sig2` = 0 µm^2 (top) or `sig2` = 0.042 µm^2 (bottom). For more details see the document string of the `fit_msds` function in appendix A.

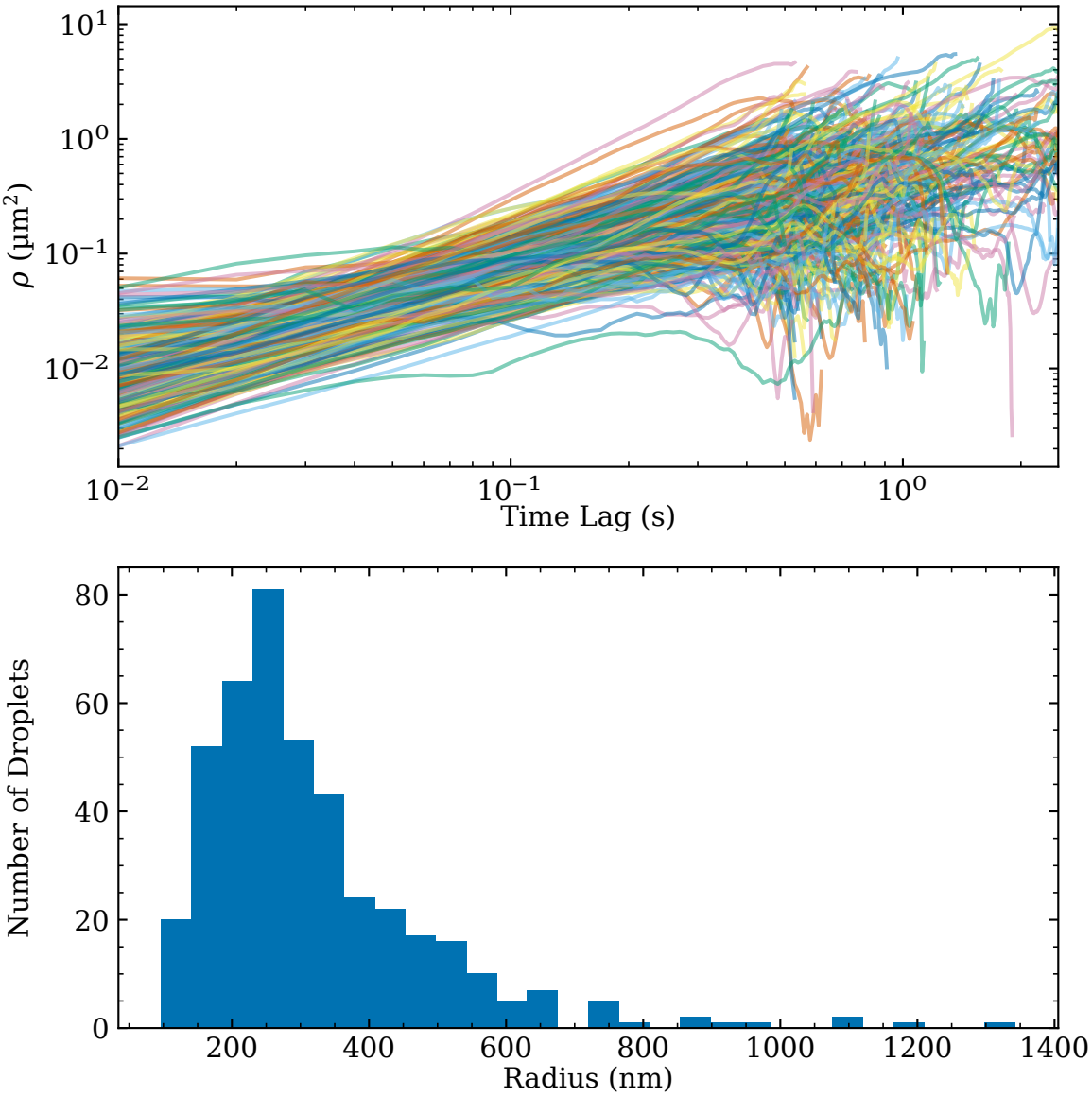

Figure 4.16. MSDs from 428 droplet trajectories (top) and histogram of their corresponding radii (bottom) for the emulsion which is shown in figs. 4.6, 4.13 and 4.14. The median and mean radii for this sample were 237.4 nm and 318.9 nm respectively. The median and mean trajectory lengths were 83 and 105.4 frames respectively.

4.5.2 pH Determination

As stated in section 4.3.1 the droplet data are affine transformed and the summed images are tracked. To determine the droplet pH from these trajectories the half-images must be analyzed separately. Although the affine transform was carefully broken into 8 pieces there is still radial distortion present in the images, since no optical setup is perfect, such that the droplet locations in the transformed and summed images may not be the correct location in the individual half-images. For this reason, before calculation of the emission ratio I re-localized the droplets in each half-image for all frames. If the re-localized position was greater than 4 px away from the original location, the original location was used instead. I chose this method, and this amount, arbitrarily to prevent dim particles in later frames of the videos from being improperly localized. It is unlikely that discarding the re-localization positions occurred for particles in the first frames. This re-localization is depicted in the upper left panel of fig. 4.17. This panel shows six images: the top-left and top-right images respectively show channel 0 and channel 1 of the first frame with the images centered on the tracked droplet, the bottom-left and bottom-right images show the pixel-average intensities, averaged over all frames of the video, (typically called a z projection, where z indicates time in this case) for a region centered around the initial droplet position for channel 0 and channel 1, respectively, and the two centered images show a central crop of the upper images. In the central cropped images it can be seen that there are two black tri markers. The small black tri markers correspond to the original localization from the summed images while the larger black tri markers correspond to the re-localized position in each channel.

After re-localization the intensities in each channel, I_0 and I_1, must be calculated. These intensities are calculated by first using eq. (4.3) with $w = 7$ px, the same as `diameter` = 15 px as was used in particle tracking. And then by subtracting the average background intensity times the number of pixels in the masked region: 149 for this diameter. Since the background was usually

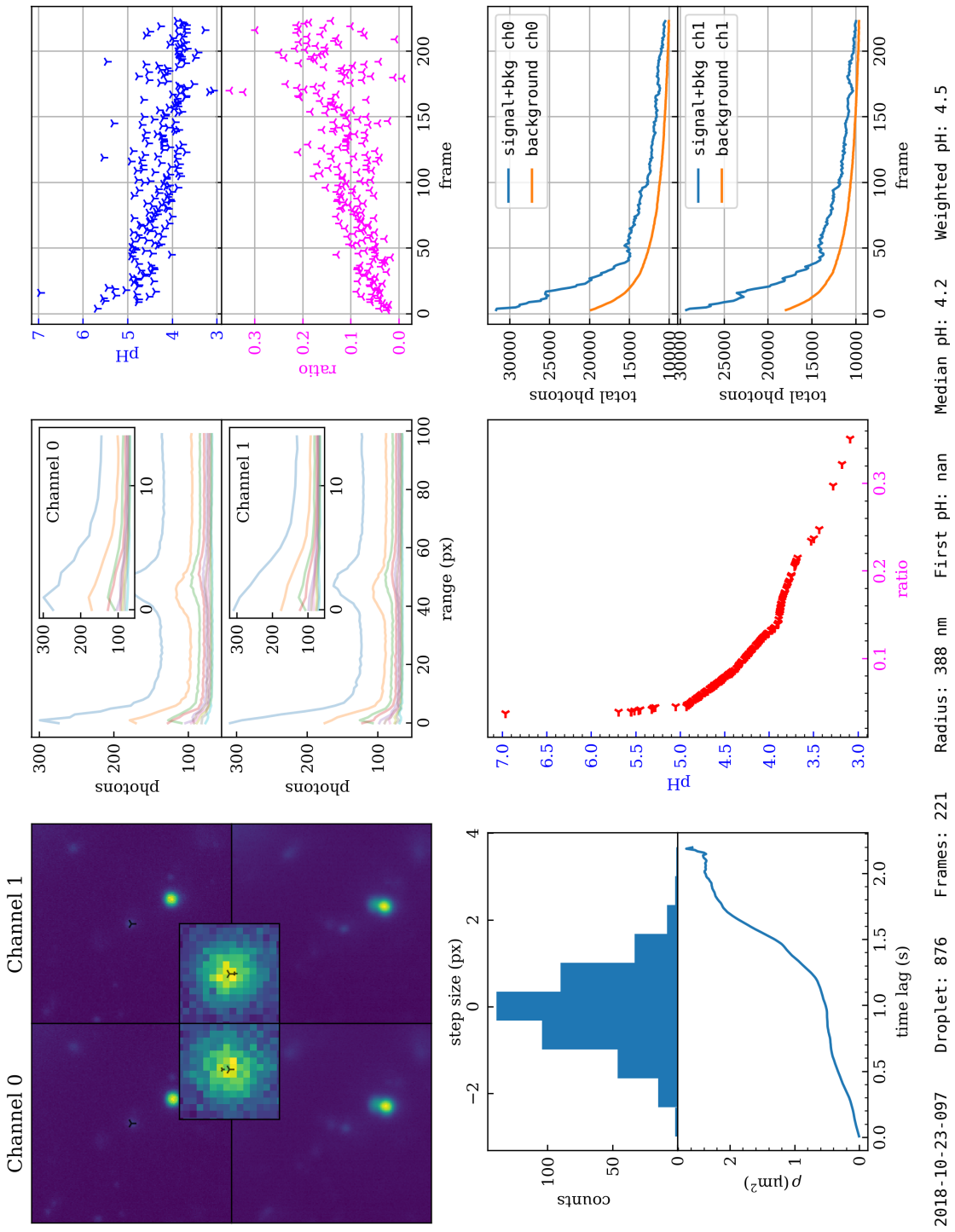

Figure 4.17. A droplet exposé. Designed as a diagnostic tool for printing on a full sheet of standard letter paper and reproduced here in its original form but scaled to fit the margins.

uniform I calculated the average background intensity from the surrounding neighborhood of pixels with a multistep process. First I calculated the average intensity of concentric annuli about the droplet coordinates according to the following formula:

$$I_b(r) = N_{\text{px}}^{-1} \sum_{(r-1)^2 < i^2 + j^2 \leq r^2} A(x_0 + i, y_0 + j), \tag{4.20}$$

where r is the radius of an annulus (restricted to integers only), N_{px} is the number of pixels in the annular region, and the sum runs over all pixels satisfying the condition while being within the bounds of the image $A(x, y)$. In other words the annuli were pixelated rings of radius r with a width of 1 px. Then I calculated the minimum of the median filter of $I_b(r)$, where the median filter had a width of 15 px. This minimum value was taken as the average background intensity per pixel for background subtraction. An example of the $I_b(r)$ is shown in the upper center panel of fig. 4.17. In this panel the top plot shows channel 0 and the bottom plot shows channel 1. The outer plots show from $r = 0$ to $r = 100$ while the insets show a zoom into the outer plots from $r = 0$ to $r = 15$. In these 4 plots are 10 sets of curves shown where each set represents one time point in the droplet trajectory with the 10 sets spaced evenly throughout the duration of the trajectory. It can be seen that the very bright droplet nearby introduces a bump in $I_b(r)$, but this does not impact the background estimation since I take the minimum of the median filter of $I_b(r)$ as the background. It can also be seen that at early and late times the background level is easily determined and always yields a value less than the central region (when r is small).

For this sample droplet the integrated intensity of the signal and signal plus background can be seen in the lower right panel of fig. 4.17. In this panel the top plot shows channel 0 and the bottom plot shows channel 1. It can be see that the background is very well defined, smoothly decays with time, and is always less than the signal level. The signal also has fluctuations which are likely due to the droplet diffusing in the z direction.

The droplet ratio is then easily calculated using eq. (2.21) and the droplet pH by a spline "look-up" using the calibration data taken under the same excitation irradiance, z focal position, and sample conditions as was discussed in section 4.4. In fig. 4.17 the ratio versus frame number and apparent pH versus frame number are shown in the upper right panel. For this droplet there was a significant change in ratio and apparent pH with time. If the ratio was out of the bounds of the calibration data, as was the case for the very first data point of this droplet, then there was no corresponding point in the apparent pH versus time plot and the apparent pH was marked as `nan` for that time point. A video of just this droplet with its localized center, ratio versus time, and its intensities versus time is shown in fig. 4.18.

Also shown in the droplet exposé, fig. 4.17, which was designed as a diagnostic plot, are the step size histogram for a one frame displacement (top of lower left panel), the MSD of this droplet (bottom of lower left panel), and a scatter plot of apparent pH versus emission ratio (lower center plot) which effectively shows the shape of the calibration curve sampled by this emulsion. Some statistics about the droplet are also shown on the lower line including the droplet ID, radius, apparent pH at the first time point, median of all apparent pH, and the weighted apparent pH which was calculated from an emission ratio derived from the total integrated intensity of all time points while using the average (x, y) position for the calibration look-up. It can be seen that this droplet has `nan` as the first apparent pH.

For the same reasons outlined in section 4.4.1 only the droplets present in the first usable frame (after shutter was fully opened) were used in the plots in the next section and only the first time point of these droplets' trajectories was used for determining their apparent pH. This point is subject to the least uncertainty in the electronic state of the dyes as we know they must all start in the ground state. However, occasionally the emission ratio of the first frame is beyond the calibration edges, due to the noise in the droplet and calibration measurements, and it is not possible to determine pH. This was the case for

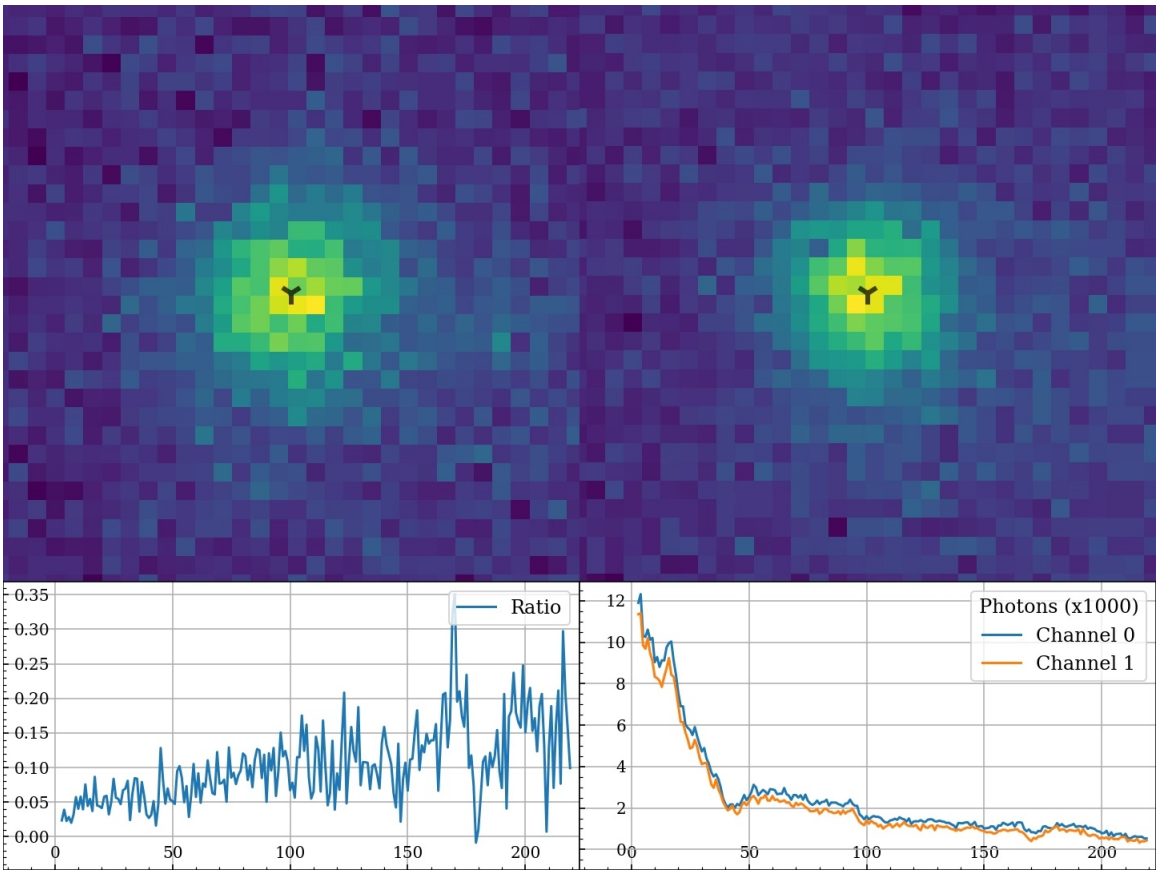

Figure 4.18. The images above shows a composite of the first and last frames of a movie of a tracked droplet and its ratio versus frame (bottom left) and photon flux versus frame (bottom right); for the full movie see `trackedDroplet.mp4`. Channel 0 is shown in the upper left and channel 1 in the upper right. The refined localizations are pinned in the centers of the two upper plots and indicated by black markers. The photon flux is in units of thousands of photons. This droplet is the same droplet shown in fig. 4.17.

the droplet shown in figs. 4.17 and 4.18; for an example droplet exposé with the first pH determined see fig. 4.19.

Although an exact pH may not be able to be calculated, it is still possible to discern a droplet with high pH versus one with low pH by determining which edge of the calibration the droplet emission ratio has gone beyond. In the case of the droplet in figs. 4.17 and 4.18 we can infer this droplet has pH greater than 5 and possibly greater than 6. Out of all the data I have obtained for droplets appearing in the first frame without any photophysics-tuning sample components and without any viscosity modifiers there were 8597 droplets within the calibration edges, 1261 droplets beyond the lower edge with high pH, and 292 droplets off the upper calibration edge with low pH.

4.6 Results and Discussion

The final step in the analysis of droplets is to apply eqs. (3.8) and (3.17) to calculate the molar change in OH^- ions, Δn, and the surface charge density of OH^- ions, σ, as was done in section 3.7 for the fluorimeter data. In the fluorimeter data there was a richer model to calculate uncertainty on the data while in the single-droplet data there is no such model, but due to the large number of droplets for each sample condition, average trends can still be determined by the scatter of the data.

A droplet dataset containing emulsions prepared with three different buffer concentrations is shown in fig. 4.20. In this figure there are four scatter plots showing emission ratio, pH, Δn, and σ versus radius for droplets made from samples containing $2\,\mathrm{mmol\,L^{-1}}$, $20\,\mathrm{mmol\,L^{-1}}$, or $200\,\mathrm{mmol\,L^{-1}}$ tris buffer at $200\,\mathrm{mmol\,L^{-1}}$ ionic strength and at pH $\approx$ 7.8. The emulsions were prepared with FC-40 with 4 wt% surfactant with a sample:FC-40 ratio of 1:400 via tip sonication for 10 s at 70 % amplitude. The data were acquired with varying excitation irradiance: $E_\mathrm{e} = 4\,\mathrm{W\,cm^{-2}}$ to $167\,\mathrm{W\,cm^{-2}}$. Out of the 3565 total

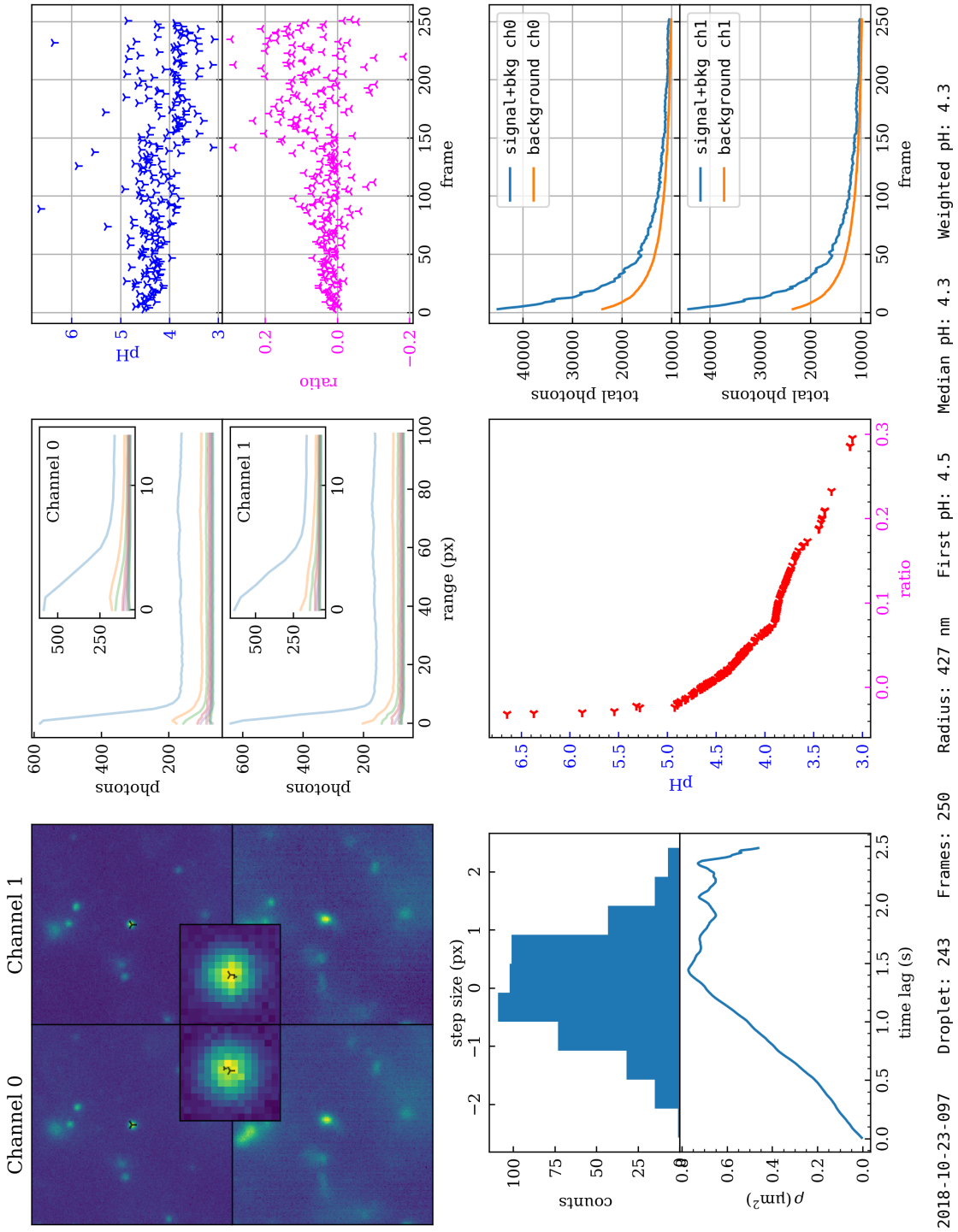

Figure 4.19. A droplet exposé for a droplet with a first pH of 4.5.

droplets in this dataset there were 847 droplets with an indeterminate pH (844 due to too low emission ratio and 3 due to too high emission ratio).

The top plot of fig. 4.20 shows the emission ratios of the 844 droplets with an indeterminate pH due to too low emission ratio. The other 2721 droplets in this dataset are not shown in this plot. For a droplet to be present in the top plot first recall that the calibration curves are position dependent (see fig. 4.12) so the lowest and highest ratios in the calibration curves are dependent on the droplets' locations. In other words, given the varying droplets' locations there are no two ratios that define the lower and upper bounds of the calibration curves. Therefore it is necessary to choose a middling ratio, R_m, which is safely within the bounds of *every* calibration curve, such as 0.2, then identify droplets with pH = nan and $R < R_m$. These droplets would have too low of an emission ratio and therefore are indicative of high pH.

The other three plots of fig. 4.20 show the pH, Δn, and σ of the 2718 droplets in this dataset for which a pH could be determined. In the pH and Δn plot it can be seen that this dataset presents the same result as was seen in the fluorimeter data, namely that the pH of the droplets are independent of the buffer concentration (see fig. 3.10) and as the buffer concentration was increased Δn was decreased (see fig. 3.14).

Another very interesting aspect of the emission ratio, pH, and Δn plots are the lack of any size dependence. Combining the lack of size dependence and lack of pH dependence leads to the surface charge density to be linearly increasing with size. Since the size measurements are likely very accurate, 98.5 % of droplets had a relative error of not more than 50 %, one interpretation is that the surface charge density is truly unbounded; however, this is not a realistic scenario. Or the surface charge density could level off at larger droplet sizes, but at up to 1.3 µm there is still no change in the slope. Another possibility is that the dye molecules adsorbed to the surface, which may not have had adsorbed hydroxide ions, and its ionization constants were altered.

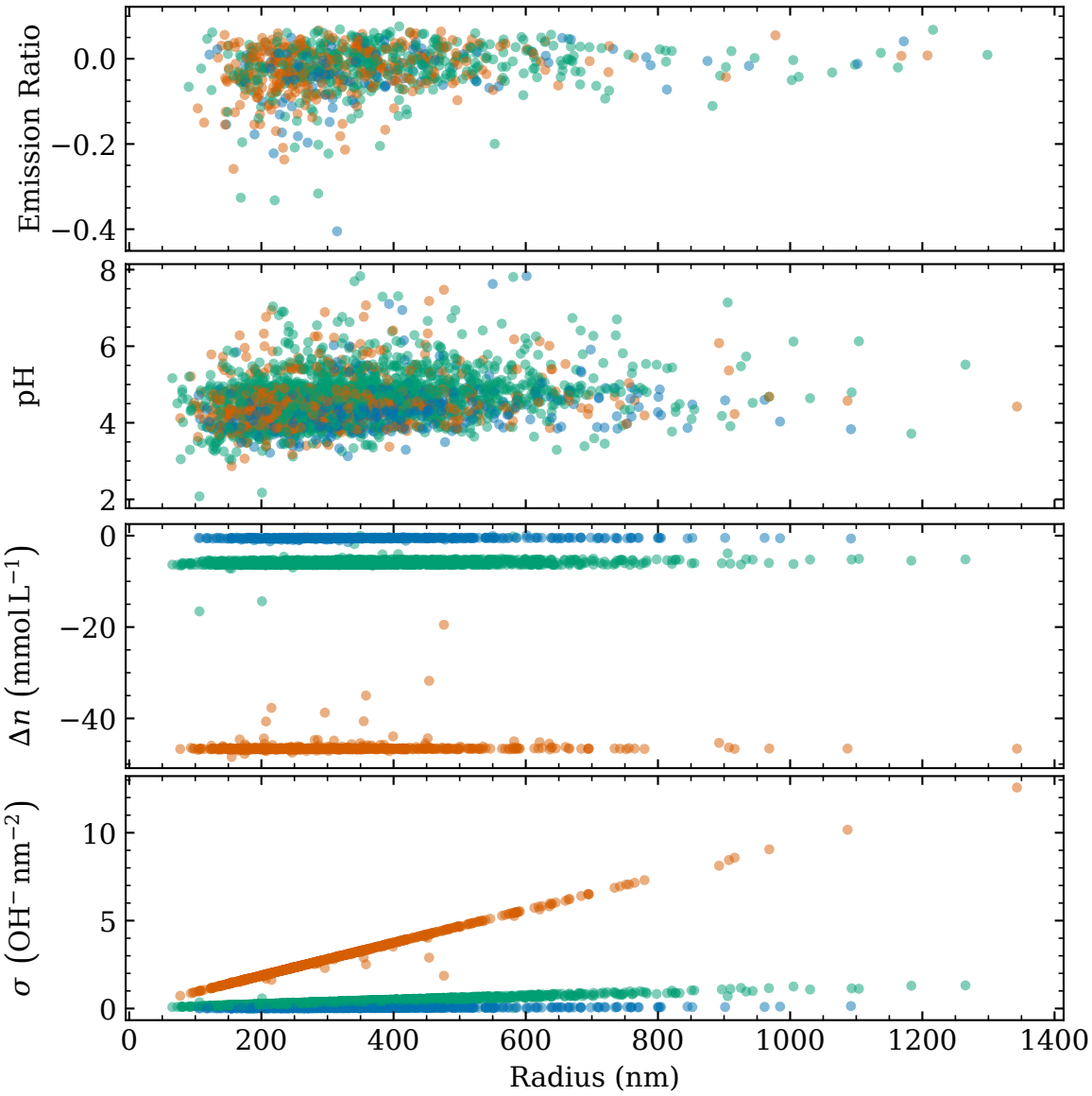

Figure 4.20. Scatter plots of emission ratio, pH, Δn, and σ as a function of radius for droplets made with tris buffer at three different concentrations. The buffer strengths, 2 mmol L^{-1}, 20 mmol L^{-1}, and 200 mmol L^{-1}, are shown by blue, green, and orange respectively. The emission ratio plot (top) shows 844 droplets, out of the 3565 droplets in this dataset, for which a pH were indeterminate since their ratios were lower than the lowest calibration ratio at the location of the droplet in the first frame. The lower three plots contain data from 2718 droplets. In all data the ionic strength was 200 mmol L^{-1} and the initial pH was approx. 7.8. Droplets were made with 4 wt% surfactant and 1:400 sample:FC-40 via tip sonication for 10 s at 70 % amplitude. In these data E_e varied from 4 W cm^{-2} to 167 W cm^{-2}.

In fig. 4.21 another dataset is shown where two parameters were varied: surfactant concentration and emulsion dilution. The emulsions were prepared with FC-40 with 1 wt% (left column), 4 wt% (middle column), or 8.8 wt% (right column) surfactant with a sample:FC-40 ratio of 1:400 via tip sonication for 10 s at 70 % amplitude. Emulsion was always diluted with the same concentration surfactant used to prepare the emulsion. In all cases for this dataset, the dispersed phase contained 8 mmol L^{-1} citrate buffer at 50 mmol L^{-1} ionic strength and at pH = 7.01. The data were acquired with $E_e = 172\,W\,cm^{-2}$ and $z = 3.5\,\mu m$ or $z = 20.1\,\mu m$ with no z dependence to the results. All plots contain data from 1520 droplets and the black lines show rolling boxcar means of all points in the respective plots.

The dilutions shown in these plots, by different colored points, are 0x, 2x, 5x, and 20x where 0x indicates no dilution, 2x shows 1 part emulsion to 1 part FC-40 with surfactant at the same concentration as was used for the emulsion preparation, and so on. It can be seen that as the emulsions were diluted there was a corresponding reduction in the average droplet size. It may be possible that dilution changes the droplet size due to the addition of surfactant since the diluent contains the same concentration of surfactant as the used for the emulsion preparation, but the prepared emulsion has "lost" surfactant to the oil-water interface. Though I do not know what the underlying mechanism may be. Another possibility is that dilution preferentially reduces the number of larger droplets because diluting requires mixing which causes collisions and since larger droplets have a larger surface area they have a higher collision rate. If collisions lead to coalescence then large droplets would swell more rapidly and cream to the top surface of the emulsion where they cannot be sampled via this microscopy technique. It is also possible that the higher curvature of the larger droplets is more favorable for coalescence. I also believe that larger droplets preferentially adhere to the walls of the tubes used to hold the emulsion or the pipette tips used to mix and dilute the emulsion.

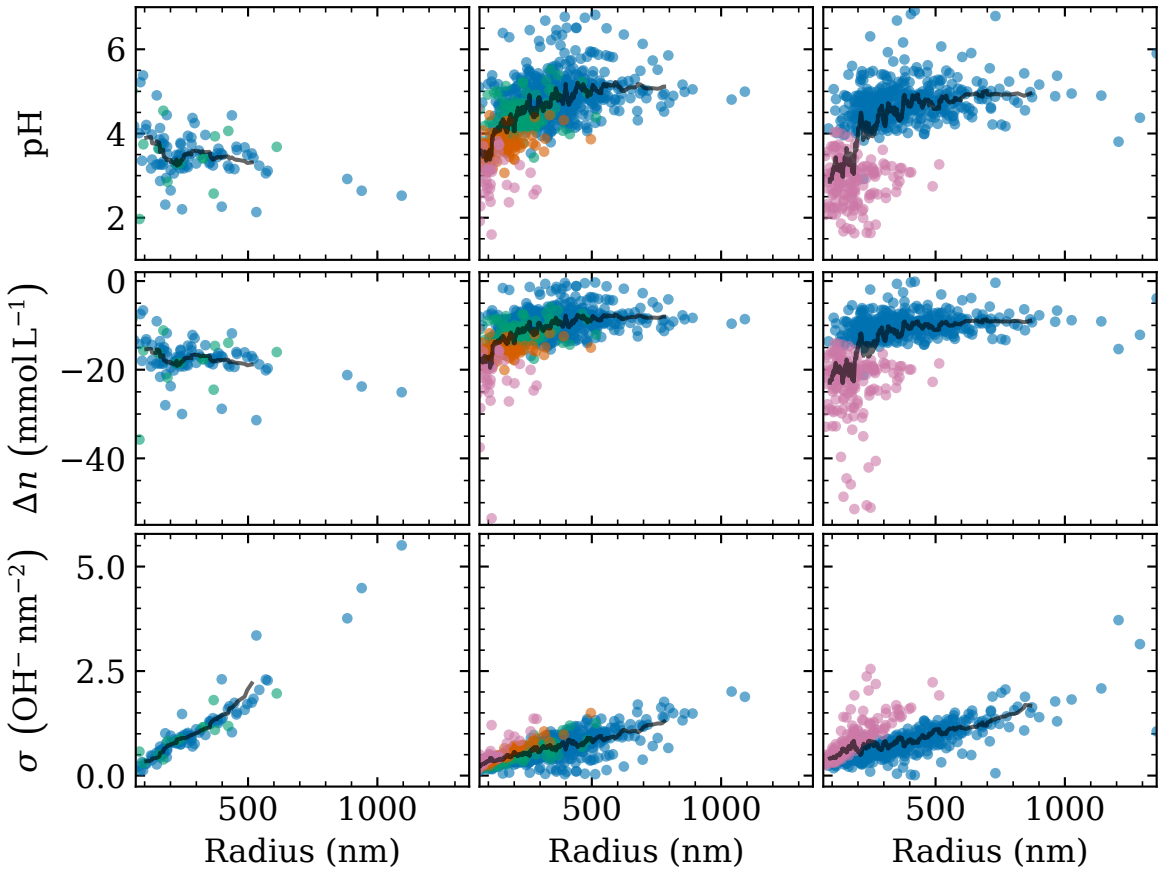

Figure 4.21. Scatter plots of pH, Δn, and σ as a function of radius for droplets at three surfactant concentrations and four dilutions. The dilutions, 0x, 2x, 5x, and 20x, are shown by blue, green, orange, and pink respectively. In all data 8 mmol L^{-1} citrate buffer was used, initially at pH = 7.01 with 50 mmol L^{-1} ionic strength. Droplets were made with 1:400 sample:FC-40 via tip sonication for 10 s at 70 % amplitude. The left, middle, and right columns show 1 wt%, 4 wt%, and 8.8 wt% surfactant respectively. The black lines show a rolling boxcar mean, including all dilutions. The excitation irradiance was 172 W cm^{-2}. In these data $z = 3.5$ µm or $z = 20.1$ µm with no change in the result. This plot contains data from 1520 droplets. Only 77 droplets were out of the calibration bounds and are not shown.

Buffer (mmol L^{-1})	pH	Δn (mmol L^{-1})	Radius (nm)
2.0	4.29	-0.5	338
20.0	4.71	-6.0	335
200.0	4.43	-46.6	278

Dilution	Surfactant (wt%)	pH	Δn (mmol L^{-1})	Radius (nm)
0	1.0	3.41	-17.7	240
	4.0	4.48	-11.5	329
	8.8	4.44	-11.7	358
2	1.0	3.61	-16.5	223
	4.0	4.15	-13.4	203
5	4.0	3.66	-16.2	154
20	4.0	3.07	-20.0	96
	8.8	2.93	-21.1	164

Table 4.4. Tables of median pH, median Δn, and median radii values for tris buffer data shown in fig. 4.20 as a function of buffer strength (top table) and for citrate buffer data shown in fig. 4.21 as a function of dilution and surfactant concentration (bottom table). The tris buffer data are for zero dilution and 4 wt% surfactant. For more details about the emulsion preparation for these samples see the respective figure captions of figs. 4.20 and 4.21 and the text.

Regardless of the cause of the reduced droplet radius with dilution, it can be seen that smaller droplets apparently have a lower pH, larger Δn, and therefore larger slope in surface charge density, σ, versus radius. It can also be seen that at 1 % surfactant there is a significantly reduced pH and increased Δn compared to the 4 % and 8.8 % data. This data and the data in fig. 4.20 are summarized in table 4.4.

From these the figures and tables it can be seen that the undiluted citrate data with 4 wt% and 8.8 wt% surfactant have nearly the same pH as the tris data yet very different Δn. It could be that this difference in Δn is due to differences in the behavior of the tris and citrate ions in the droplets or it could be due to the difference in ionic strength which were 200 mmol L^{-1} and 50 mmol L^{-1} respectively. However, it is not possible to rule out that that the pH in these undiluted, high surfactant droplets are not distinguishable from the bulk pH within the noise and limitation of this experiment. This stems

from the photophysics of the dye and from the fact that the initial sample pH were adjusted to values beyond the calibration sensitivity range due to the expectation that the pH in droplets would be lower and therefore the emission ratio in the calibration sensitivity range.

At high pH the calibration curve is nearly flat for early excitation times or for lower excitation irradiance (see fig. 4.11). Therefore for samples with an emission ratio near the high pH edge of the calibration curve, there is a high probability for the sample emission ratio to be out of bounds or for it to register as a lower pH than the correct sample pH due to the noise in the emission ratio measurement. For example in a self-check of the calibration data for a pH = 7 sample, where the self-check treated the calibration data similarly to how droplet data were processed, missed the calibration curve for 50 % of the pixels in the self-check and the remaining pixels measured as pH = 6.8, on average, instead. When considering the dynamical nature of the emission ratio due to dye photophysics it becomes clear that if a droplet were to have pH ≈ 7 and if the emission ratio in this droplet were to increase more rapidly than the bulk calibration samples increase at this pH, than it is conceivable that the measured pH of the droplet could be either off the calibration curve or in the range of 4.5 to 5.5 depending on how fast the emission ratio changed and the noise in the measurements.

This may be precisely what occurs in the undiluted citrate droplets prepared with 4 wt% or greater surfactant and the tris droplets, also prepared with 4 wt% surfactant. In both datasets the median pH are about the same and near the pH range just described. On deeper inspection it appears that 15 of the 1597 droplets had a low emission ratio beyond the calibration edge indicating high pH for the citrate data where the excitation irradiance was always high. Whereas in the tris data 844 of the 3565 droplets had a low emission ratio beyond the calibration edge indicating high pH. Though the tris data were a blend of high and low excitation irradiance it can be seen in table 4.5 that lower excitation irradiances have a higher proportion of droplets with an emission ratio below the

E_e (W cm^{-2})	N_{high}	N_{low}	N_{mid}	N_{low}/N_{tot}
4	0	335	754	0.308
15	1	399	1249	0.242
59	2	7	110	0.059
167	0	103	605	0.145
173	62	15	1520	0.009

Table 4.5. Number of droplets with an emission ratios above the calibration curve, N_{high}, with an emission ratios below the calibration curve, N_{low}, and with an emission ratios within the calibration curve, N_{mid}, as a function of excitation irradiance. Also calculated is the fractional number of droplets with low emission ratio out of the total number of droplets. The top four rows are for the tris data shown in fig. 4.20 and the bottom row is for the citrate data shown in fig. 4.21.

calibration curve compared to the higher irradiance data. Therefore it is likely that the higher the excitation irradiance, the more rapidly droplet emission ratio changes from about zero or lower to somewhere between 0 and 0.05 which then registers as lower pH between 4.5 and 5.5 (see fig. 4.11). Conversely lower excitation irradiance data exhibits less changes thus more calibration misses. Then perhaps it is safe to assume that samples with a median pH of about 4.5 are measuring at the detection limit of this measurement technique regardless of the excitation irradiance since the only distinguishing factor between different excitation irradiances is the number of misses.

Under the assumption that a median pH of about 4.5 is at the detection limit it can be seen from table 4.4 the emulsions with pH about 4.5 only include undiluted droplets prepared with 4 wt% surfactant or more. If I assume that these emulsions have no change in pH from the initial pH of the aqueous sample used to prepare them, or equivalently $\Delta n = 0\,\text{mmol}\,\text{L}^{-1}$, then the strange behavior where Δn increases rapidly with buffer strength would disappear and I can shift the pH and Δn of diluted emulsions to get a minimum estimate of the magnitude of Δn and σ for the FC-40 emulsions in my studies in general.

For example take the median measurements of the 0x and 20x diluted emulsions for the 4.0 % surfactant citrate data from table 4.4: pH = 4.48 and

Dilution	Surfactant (wt%)	Δn (mmol L^{-1})	Radius (nm)	σ (OH^- nm^{-2})
0	1.0	-6.2	240	0.299
	4.0	0	329	0
	8.8	-0.2	358	0.014
2	1.0	-5.0	223	0.224
	4.0	-1.9	203	0.077
5	4.0	-4.7	154	0.145
20	4.0	-8.5	96	0.164
	8.8	-9.6	164	0.316

Table 4.6. Table of re-scaled median Δn, median radii, and estimated median σ for citrate droplets at various dilutions and surfactant concentrations. Δn data was re-scaled from table 4.4 by subtracting the value for the 0x diluted, 4.0 wt% emulsion, $-11.5\,\mathrm{mmol\,L^{-1}}$, from every row. Radius was copied from table 4.4 and σ was calculated using the re-scaled Δn and median radii.

$\Delta n = -11.5\,\mathrm{mmol\,L^{-1}}$ for undiluted and pH = 3.07 and $\Delta n = -20.0\,\mathrm{mmol\,L^{-1}}$ for 20x diluted. Then by setting the undiluted emulsion as the baseline I get $\Delta(\mathrm{pH}) = -1.41$ and more importantly the change in Δn since it accounts for the buffer strength is $\Delta(\Delta n) = -8.5\,\mathrm{mmol\,L^{-1}}$. There was also a reduction in median radius from 329 nm to 96 nm for these two conditions.

As another example compare the data for undiluted citrate droplets with 4 wt% and 1 wt% surfactant from table 4.4: it can be see that there is also a small reduction in median radius, 329 nm to 240 nm. For these two samples pH = 4.48 and $\Delta n = -11.5\,\mathrm{mmol\,L^{-1}}$ for 4 wt% while pH = 3.41 and $\Delta n = -17.7\,\mathrm{mmol\,L^{-1}}$ for 1 wt% then taking the same approach I calculate $\Delta(\mathrm{pH}) = -1.07$ and $\Delta(\Delta n) = -6.2\,\mathrm{mmol\,L^{-1}}$.

Thus by taking the undiluted citrate droplets prepared with 4 wt% surfactant as the baseline for all other measurements under the assumption this emulsion's real pH was unperturbed then I can calculate a *minimum* Δn and σ for all other emulsions. So dropping the extra Δ in $\Delta(\Delta n)$ and calculating the surface charge density using the re-scaled values and median radii I get the results shown in table 4.6. The surface charge densities in this table are what I suggest to be the *minimum* effect. From these data we can conclude that to avoid charging

of the oil-water interface for water in Fluorinert FC-40 reverse nanoemulsions stabilized with PFPE–PEG–PFPE I recommend to use 4 wt% surfactant or more and to avoid diluting the prepared emulsion.

APPENDIX

MSD ANALYSIS CODE

```
"""
The main user-facing function of this module is fit_msds. It is
based on two papers by Xavier Michalet (and Andrew Berglund).

[1] Michalet, X. (2010). Mean square displacement analysis of
    single-particle trajectories with localization error:
    Brownian motion in an isotropic medium.
    Phys. Rev. E, 82(4), 1–13.
    http://doi.org/10.1103/PhysRevE.82.041914
[2] Michalet, X., & Berglund, A. J. (2012). Optimal diffusion
    coefficient estimation in single-particle tracking. Phy.
    Rev.E, 85(6), 1–14.
    http://doi.org/10.1103/PhysRevE.85.061916
"""
import numpy as np
import pandas as pd

def f(i,N,x):
    """
    Calculate the variance of the MSD for a trajectory of length
    N with localization error x for a time lag of i less than
    N-1. x should be from zero to infinity. Replace negative
    values of x with 0.

    Using equations B12 and C1
    """
    n = i
    K = N - n
    if n <= K:
        V = n/6/K**2 * (4*n**2*K + 2*K - n**3 + n) + 1/K * (2*n*x + (1 + (1 -
         ↪  n/K)/2)*x**2)
    else:
        V = 1/6/K * (6*n**2*K - 4*n*K**2 + 4*n + K**3 - K) + 1/K * (2*n*x +
         ↪  x**2)
    return 1/V

def g(i,j,N,x):
    """
    Calculate the covariance of the MSD for a trajectory of
    length N with localization error x between two time lags
    i and j where i and j are less than N-1 and i is greater
    than j. x should be from zero to infinity. Replace negative
    values of x with 0.

    Uses equations B12 and C1
    """
    # For i > j
```

```
    m, n = i, j
    K = N - n
    P = N - m
    if m+n <= N:
        V = n/6/K/P * (4*n**2*K + 2*K - n**3 + n + (m-n)*(6*n*P-4*n**2-2)) + 1/K
         ↪  * (2*n*x + (1-n/2/P)*x**2)
    else:
        V = 1/6/K * (6*n**2*K - 4*n*K**2 + K**3 + 4*n - K + (m-n)*((n+m)*(2*K+P)
         ↪  + 2*n*P - 3*K**2 + 1)) + 1/K * (2*n*x + x**2/2)
    return V

def rel_err(p,N,x,R=1/6,d=2):
    """
    Calculate the relative errors on D and σ² Std(D)/D and
    Std(σ²)/σ² from a least squares fit using p points for a
    length N trajectory with localization error x and motion
    blur factor R. x should be from zero to infinity. Replace
    negative values of x with 0.

    Using equations B11, B15 and B16
    """
    if x is np.inf:
        return np.inf, np.inf

    # Calculate var(b)/b**2
    coeff = 2/d*(12/p/(p**2-1))**2
    SUM = 0
    for i in range(1,p+1):
        SUM += ((p+1)/2 - i)**2 * f(i,N,x)**-1
        for j in range(1,i):
            SUM += 2*((p+1)/2 - i)*((p+1)/2 - j)*g(i,j,N,x)
    rel_err_b_sq = coeff*SUM

    if x is 0:
        with np.errstate(invalid='ignore'):
            rel_err_D = np.sqrt(rel_err_b_sq)
        return np.inf, rel_err_D

    # Calculate var(a)/a²
    coeff = 2/d * 1/x**2 * (6/p/(p-1))**2
    SUM = 0
    for i in range(1,p+1):
        SUM += ((2*p+1)/3 - i)**2 * f(i,N,x)**-1
        for j in range(1,i):
            SUM += 2*((2*p+1)/3-i)*((2*p+1)/3-j)*g(i,j,N,x)
    rel_err_a_sq = coeff*SUM

    # Calculate U(p,N,x) (proportional to covariance(a,b))
    # and necessary to calculate var(σ²)/σ⁴
    coeff = 2/d/(p+1) * (6/p/(p-1))**2
    SUM = 0
    for i in range(1,p+1):
        SUM += ((2*p+1)/3 - i)*(i-(p+1)/2) * f(i,N,x)**-1
        for j in range(1,p+1):
            if j == i:
                continue
            SUM += ((2*p+1)/3 - i) * (j - (p+1)/2) * g(i,j,N,x)
    U = coeff*SUM
```

```
    # Calculate var(σ²)/σ⁴
    rel_err_sig2_sq = 1/(x+2*R)**2 * (x**2 * rel_err_a_sq + 4*R**2 *
     ↪  rel_err_b_sq + 8*R*U)
    with np.errstate(invalid='ignore'):
        rel_err_sig2 = np.sqrt(rel_err_sig2_sq)
        rel_err_D = np.sqrt(rel_err_b_sq)
    return rel_err_sig2, rel_err_D

def p_min_a(x,N):
    """
    Calculate the number of points to fit the msd to minimize
    the error in a with localization error x and the trajectory
    length N. x should be from zero to infinity. Replace
    negative values of x with 0.
    """
    L_a = 3 + (4.5*N**0.4 - 8.5)**1.2
    if x is np.inf:
        return int(L_a)
    f_a = 2 + 1.6*x**0.51
    pmin = f_a*L_a/(f_a**3 + L_a**3)**(1/3)
    return int(pmin)

def p_min_b(x,N):
    """
    Calculate the number of points to fit the msd to minimize
    the error in b with localization error x and the trajectory
    length N. x should be from zero to infinity. Replace
    negative values of x with 0.
    """
    L_b = 0.8 + 0.564*N
    if x is np.inf:
        return int(L_b)
    f_b = 2 + 1.35*x**0.6
    pmin = f_b*L_b/(f_b**3 + L_b**3)**(1/3)
    return int(min(L_b, pmin))

def fit(time, rho, p, fpmin):
    """
    Fit the MSD (rho vs. time) using p points and then calculate
    a new p_min using the function passed in as fpmin.
    """
    A = np.stack([np.ones(p), time[:p]],1)
    B = rho[:p]
    # lin-least-sq A*x=B solution (A'A*x=A'B)
    a, b = np.linalg.solve(A.T.dot(A),A.T.dot(B))

    dt = time[1]-time[0]
    if a < 0:
        x = 0
        pmin = 2
    elif b < 0:
        x = np.inf
        pmin = fpmin(x, len(rho))
    else:
        x = a/b/dt
        pmin = fpmin(x, len(rho))
    return a, b, x, max(pmin,2)

def fit_msds(msd, R=1/6, d=2, eta=1, T=25, plot=False):
```

```
    """
    Fit the msds contained in the DataFrame msd using the
    method described by Xavier Michalet and Andrew J.
    Berglund in their 2012 Phys. Rev. E paper. [2]

    Parameters
    ----------
    msd : DataFrame of msds
        The index must contain the time lags and each column
        the msds for the particle with particle ID indicated
        by the column's key. The msds should be in units of
        μm²/s and the index in seconds.
    R : integer
        The motion blur coefficient in range [0,1/4]
    d : integer
        Dimensionality used to calculate the msds
    eta : float
        Viscosity [centiPoise] of fluid that colloid is
        suspended in (used to calculate radii)
    T : float
        Temperature in Celsius
        (used to calculate radii)
    plot : bool, optional
        If true will plot a histogram of diffusion
        coefficients and radii

    Returns
    -------
    DataFrame with the following attributes for each particle:
        N : Length of trajectory
        D : Diffusion coefficient in μm²/s
        errD : Relative error on D (Std(D)/D)
        sig2 : Localization error in μm²
        errS2 : Relative error on σ² (Std(σ²)/σ²)
        r : Radius in nm
        sigr : 1σ error on radius in nm
        pminA : Number of points used to calculate sig2
                and errS2
        pminB : Number of points used to calculate D and errD

    Note that errD, errS2, and sigr may be infinite if reduced
    square localization error (x = σ²/DΔt - 2R) is either very
    big or very small which causes noisy data and indicates an
    unreliable estimate of D (and r) or σ².
    """
    df = pd.DataFrame()
    for col, vals in msd.iteritems():
        vals = vals[vals.notnull()]
        time, rho = vals.index, vals.values
        dt = time[1]-time[0]
        N = len(vals) + 1

        # Fit to find localization error sig2
        pmin = max(len(vals)//10, 2)
        pmins = []
        for i in range(100):
            a, b, x, pmin = fit(time, rho, pmin, p_min_a)

            if pmin in pmins:
```

```
                D2 = b/2/d  # only used to calculate sig2
                sig2 = a/2/d + 2*R*D2*dt
                errS2 = rel_err(pmins[-1],N,x,R,d)[0]
                pminA = pmin
                break
            pmins.append(pmin)
        else:
            sig2 = None
            errS2 = None
            pminA = None
            print('Could not converge on pmin_a for particle %d' % col)

        # Fit to find diffusion coefficient
        pmin = max(len(vals)//10, 2)
        pmins = []
        for i in range(100):
            a, b, x, pmin = fit(time, rho, pmin, p_min_b)

            if pmin in pmins:
                D = b/2/d
                errD = rel_err(pmins[-1],N,x,R,d)[1]
                pminB = pmin
                break
            pmins.append(pmin)
        else:
            D = None
            errD = None
            pminB = None
            print('Could not converge on pmin_b for particle %d' % col)

        kB = 1.38065e-23
        # convert D from um^2/s to m^2/s
        # convert eta from cP to Pa*s = kg per meter per sec
        r = kB*(T+273.15)/(6*np.pi*(eta/1000)*(D*1e-12))
        # convert r from m to nm
        r = r * 1e9

        df[col] = pd.Series([N, D, errD, sig2, errS2, r, r*errD, pminA, pminB],
         ↪  index = ['N', 'D', 'errD', 'sig2', 'errS2', 'r', 'sigr', 'pminA',
         ↪  'pminB'])

    df = df.T
    df.index = df.index.astype(int)
    df.index.name = 'particle'
    if plot:
        fig, (ax0, ax1) = pl.subplots(1, 2, figsize=(6,4))
        df.hist('D', ax=ax0)
        df.hist('r', ax=ax1)
        ax0.set_xlabel('Diffusion coefficient (μm²/s)')
        ax1.set_xlabel('Radius (nm)')
        return df, fig
    print('Mean Diameter: %.3f nm' % (df.r.mean()*2))
    return df
```

BIBLIOGRAPHY

[1] D. Julian McClements. “Nanoemulsions versus Microemulsions: Terminology, Differences, and Similarities”. In: *Soft Matter* 8.6 (2012), pp. 1719–1729. DOI: 10.1039/C2SM06903B.

[2] C. Solans et al. “Nano-Emulsions”. In: *Current Opinion in Colloid & Interface Science* 10.3 (Oct. 1, 2005), pp. 102–110. ISSN: 1359-0294. DOI: 10.1016/j.cocis.2005.06.004.

[3] M. M. Fryd and T. G. Mason. “Advanced Nanoemulsions”. In: *Annual Review of Physical Chemistry* 63.1 (2012), pp. 493–518. DOI: 10.1146/annurev-physchem-032210-103436.

[4] Y. Singh et al. “Nanoemulsion: Concepts, Development and Applications in Drug Delivery”. In: *Journal of Controlled Release* 252 (Apr. 28, 2017), pp. 28–49. ISSN: 0168-3659. DOI: 10.1016/j.jconrel.2017.03.008.

[5] R. R. Bhosale et al. “Nanoemulsion: A Review on Novel Profusion in Advanced Drug Delivery”. In: *Indian Journal of Pharmaceutical and Biological Research* 2.01 (Mar. 20, 2014). ISSN: 2320-9267. DOI: 10.30750/ijpbr.2.1.19.

[6] M. P. Krafft. “Fluorocarbons and Fluorinated Amphiphiles in Drug Delivery and Biomedical Research”. In: *Advanced Drug Delivery Reviews*. Lipid Assemblies for Drug Delivery 47.2 (Apr. 25, 2001), pp. 209–228. ISSN: 0169-409X. DOI: 10.1016/S0169-409X(01)00107-7.

[7] T. Zhang et al. “Perfluorocarbon-Based Nanomedicine: Emerging Strategy for Diagnosis and Treatment of Diseases”. In: *MRS Communications* 8.2 (June 2018), pp. 303–313. ISSN: 2159-6859. DOI: 10.1557/mrc.2018.49.

[8] J. E. Reiner et al. “Optically Trapped Aqueous Droplets for Single Molecule Studies”. In: *Applied Physics Letters* 89.1 (2006), pp. 2–4. ISSN: 00036951. DOI: 10.1063/1.2219977.

[9] L. S. Goldner, A. M. Jofre, and J. Tang. “Chapter 5 - Droplet Confinement and Fluorescence Measurement of Single Molecules”. In: *Methods in Enzymology*. Ed. by N. G. Walter. Vol. 472. Single Molecule Tools: Fluorescence Based Approaches, Part A. Academic Press, Jan. 1, 2010, pp. 61–88. DOI: 10.1016/S0076-6879(10)72015-2.

[10] S. Rahmanseresht et al. “Single-Molecule-Sensitive Fluorescence Resonance Energy Transfer in Freely-Diffusing Attoliter Droplets”. In: *Applied Physics Letters* 106.19 (2015), p. 194107. ISSN: 0003-6951. DOI: 10.1063/1.4921202.

[11] H. Wakioka et al. “Attoliter Order Droplet Formation Using Nanochannels and Enzyme Reaction inside a Droplet”. In: *2013 IEEE 26th International Conference on Micro Electro Mechanical Systems (MEMS)*. Vol. 11. IEEE, Jan. 12, 2013, pp. 1161–1164. ISBN: 978-1-4673-5655-8. DOI: 10.1109/MEMSYS.2013.6474457.

[12] L. Shui, A. Van Den Berg, and J. C. T. Eijkel. “Scalable Attoliter Monodisperse Droplet Formation Using Multiphase Nano-Microfluidics”. In: *Microfluidics and Nanofluidics* 11.1 (2011), pp. 87–92. ISSN: 16134982. DOI: 10.1007/s10404-011-0776-7.

[13] K. Kawai et al. “Continuous Generation of Femtolitre Droplets Using Multistage Dividing Microfluidic Channel”. In: *Current Applied Physics* 12 (Dec. 2012), S33–S37. ISSN: 15671739. DOI: 10.1016/j.cap.2012.06.022.

[14] Y.-J. Yang et al. “Generation of Sub-Femtoliter Droplet by T-Junction Splitting on Microfluidic Chips”. In: *Applied Physics Letters* 102.12 (2013), p. 123502. ISSN: 00036951. DOI: 10.1063/1.4798510.

[15] R. Arayanarakool et al. “Single-Enzyme Analysis in a Droplet-Based Micro- and Nanofluidic System.” In: *Lab on a chip* 13.10 (May 21, 2013), pp. 1955–62. ISSN: 1473-0189. DOI: 10.1039/c3lc41100a.

[16] R. Weinmeister et al. “Single-Fluorophore Detection in Femtoliter Droplets Generated by Flow Focusing”. In: *ACS Nano* 9.10 (Oct. 27, 2015), pp. 9718–9730. ISSN: 1936-0851. DOI: 10.1021/acsnano.5b02422.

[17] J. H. Fendler. *Membrane Mimetic Chemistry: Characterizations and Applications of Micelles, Microemulsions, Monolayers, Bilayers, Vesicles, Host-Guest Systems, and Polyions*. 02944 OCLC: 476583838. New York: Wiley, 1982. ISBN: 978-0-471-07918-7.

[18] K. Vos, C. Laane, and A. J. W. G. Visser. “Spectroscopy of Reversed Micelles”. In: *Photochemistry and Photobiology* 45.S1 (1987), pp. 863–878. ISSN: 1751-1097. DOI: 10.1111/j.1751-1097.1987.tb07897.x.

[19] O. A. El Seoud. “Effects of Organized Surfactant Assemblies on Acid-Base Equilibria”. In: *Advances in Colloid and Interface Science* 30 (Jan. 1, 1989), pp. 1–30. ISSN: 0001-8686. DOI: 10.1016/0001-8686(89)80002-8.

[20] N. A. Vodolazkaya, Y. A. Kleshchevnikova, and N. O. Mchedlov-Petrossyan. “Differentiating Impact of the AOT-Stabilized Droplets of Water-in-Octane

Microemulsions as Examined Using Halogenated Fluoresceins as Molecular Probes". In: *Journal of Molecular Liquids* 187 (Nov. 1, 2013), pp. 381–388. ISSN: 0167-7322. DOI: 10.1016/j.molliq.2013.08.018.

[21] B. Baruah et al. "When Is Water Not Water? Exploring Water Confined in Large Reverse Micelles Using a Highly Charged Inorganic Molecular Probe". In: *Journal of the American Chemical Society* 128.39 (Oct. 1, 2006), pp. 12758–12765. ISSN: 0002-7863. DOI: 10.1021/ja0624319.

[22] B. S. Marques et al. "Measurement and Control of pH in the Aqueous Interior of Reverse Micelles". In: *The Journal of Physical Chemistry B* 118.8 (Feb. 27, 2014), pp. 2020–2031. ISSN: 1520-6106. DOI: 10.1021/jp4103349.

[23] N. A. Halliday, A. C. Peet, and M. M. Britton. "Detection of pH in Microemulsions, without a Probe Molecule, Using Magnetic Resonance". In: *The Journal of Physical Chemistry B* 114.43 (Nov. 4, 2010), pp. 13745–13751. ISSN: 1520-6106. DOI: 10.1021/jp108649x.

[24] J. Fu and L. Zhang. "Probing pH Difference between Micellar Solution and Nanoscale Water within Common Black Film by Fluorescent Dye". In: *Chemical Physics* 504 (Mar. 26, 2018), pp. 1–7. ISSN: 0301-0104. DOI: 10.1016/j.chemphys.2018.02.013.

[25] X. Sun et al. "Single-Molecule Studies of Acidity Distributions in Mesoporous Aluminosilicate Thin Films". In: *Langmuir* 31.20 (May 26, 2015), pp. 5667–5675. ISSN: 0743-7463. DOI: 10.1021/acs.langmuir.5b01628.

[26] D. C. Crans and N. E. Levinger. "The Conundrum of pH in Water Nanodroplets: Sensing pH in Reverse Micelle Water Pools". In: *Accounts of Chemical Research* 45.10 (Oct. 16, 2012), pp. 1637–1645. ISSN: 0001-4842. DOI: 10.1021/ar200269g.

[27] B. Baruah et al. "Do Probe Molecules Influence Water in Confinement?" In: *The Journal of Physical Chemistry B* 112.33 (Aug. 1, 2008), pp. 10158–10164. ISSN: 1520-6106. DOI: 10.1021/jp800390t.

[28] K. Marinova, R. Alargova, and N. Denkov. "Charging of Oil-Water Interfaces Due to Spontaneous Adsorption of Hydroxyl Ions". In: *Langmuir* 12.8 (1996), pp. 2045–2051.

[29] J. K. Beattie and A. M. Djerdjev. "The Pristine Oil/Water Interface: Surfactant-Free Hydroxide-Charged Emulsions". In: *Angewandte Chemie - International Edition* 43.27 (2004), pp. 3568–3571. ISSN: 14337851. DOI: 10.1002/anie.200453916.

[30] R. Zangi and J. B. F. N. Engberts. "Physisorption of Hydroxide Ions from Aqueous Solution to a Hydrophobic Surface". In: *Journal of the American*

Chemical Society 127.7 (2005), pp. 2272–2276. ISSN: 00027863. DOI: 10.1021/ja044426f.

[31] C. Márquez-Beltrán and D. Langevin. “Electrostatic Effects in Films Stabilised by Non-Ionic Surfactants”. In: *Journal of Colloid and Interface Science*. In Memory of Professor Hironobu Kunieda 312.1 (Aug. 1, 2007), pp. 47–51. ISSN: 0021-9797. DOI: 10.1016/j.jcis.2006.10.015.

[32] A. Gray-Weale and J. K. Beattie. “An Explanation for the Charge on Water’s Surface.” In: *Physical chemistry chemical physics : PCCP* 11.46 (2009), pp. 10994–11005. ISSN: 1463-9076. DOI: 10.1039/b901806a.

[33] C. S. Tian and Y. R. Shen. “Structure and Charging of Hydrophobic Material/Water Interfaces Studied by Phase-Sensitive Sum-Frequency Vibrational Spectroscopy.” In: *Proceedings of the National Academy of Sciences of the United States of America* 106.36 (2009), pp. 15148–15153. ISSN: 0027-8424. DOI: 10.1073/pnas.0901480106.

[34] R. Vácha et al. “The Orientation and Charge of Water at the Hydrophobic Oil Droplet–Water Interface”. In: *Journal of the American Chemical Society* 133.26 (July 6, 2011), pp. 10204–10210. ISSN: 0002-7863. DOI: 10.1021/ja202081x.

[35] E. R. Cohen et al. *Quantities, Units and Symbols in Physical Chemistry*. Aug. 2, 2007. ISBN: 978-0-85404-433-7. DOI: 10.1039/9781847557889.

[36] H. S. Harned and B. B. Owen. *The Physical Chemistry of Electrolytic Solutions*. Third edition. American Chemical Society. Monograph Series: No. 137. Reinhold Pub. Corp., 1958.

[37] R. P. Buck et al. “Measurement of pH. Definition, Standards, and Procedures”. In: *Pure and Applied Chemistry* 74.11 (2002), p. 32.

[38] P. Debye and E. Hückel. “Zur Theorie Der Elektrolyte”. In: *Physikalische Zeitschrift* 24.9 (1923), pp. 185–206.

[39] M. R. Wright. *An Introduction to Aqueous Electrolyte Solutions*. OCLC: 455986325. Chichester: J. Wiley, 2007. ISBN: 978-0-470-84293-5.

[40] C. W. Davies. *Ion Association*. OCLC: 29297233. Washington: Butterworths, 1962.

[41] C. Holtze et al. “Biocompatible Surfactants for Water-in-Fluorocarbon Emulsions”. In: *Lab on a Chip* 8.10 (Oct. 2008), pp. 1632–1639. ISSN: 1473-0197. DOI: 10.1039/b806706f.

[42] L. Mazutis and A. D. Griffiths. “Selective Droplet Coalescence Using Microfluidic Systems”. In: *Lab on a Chip* 12.10 (2012), p. 1800. ISSN: 1473-0197. DOI: 10.1039/c2lc40121e.

[43] R. Nassar. *RAN Biotechnologies, Surfactant for Microfluidics*. URL: https://www.ranbiotechnologies.com (visited on 04/20/2019).

[44] S. A. Smith and W. A. Pretorius. “Spectrophotometric Determination of pKa Values for Fluorescein Using Activity Coefficient Corrections”. In: *Water SA* 28.4 (2002), pp. 395–402. ISSN: 03784738. DOI: 10.4314/wsa.v28i4.4912.

[45] A. Orte et al. “Absorption and Emission Study of 2′,7′-Difluorofluorescein and Its Excited-State Buffer-Mediated Proton Exchange Reactions”. In: *Journal of Physical Chemistry A* 109.5 (2005), pp. 734–747. ISSN: 10895639. DOI: 10.1021/jp046786v.

[46] W. C. Sun et al. “Synthesis of Fluorinated Fluoresceins”. In: *Journal of Organic Chemistry* 62.19 (1997), pp. 6469–6475. ISSN: 00223263. DOI: 10.1021/jo9706178.

[47] M. Czerny and A. F. Turner. “Über den Astigmatismus bei Spiegelspektrometern”. In: *Zeitschrift für Physik* 61.11 (Nov. 1, 1930), pp. 792–797. ISSN: 0044-3328. DOI: 10.1007/BF01340206.

[48] R. A. Durst and B. R. Staples. “Tris/Tris·HCl: A Standard Buffer for Use in the Physiologic pH Range”. In: *Clinical Chemistry* 18.3 (Mar. 1, 1972), pp. 206–208. ISSN: 0009-9147.

[49] R. Sjöback et al. “Absorption and Fluorescence Properties of Fluorescein”. In: *Spectrochimica Acta Part A* 51.6 (1995), pp. L7–L21. ISSN: 13861425. DOI: 10.1016/0584-8539(95)01421-P.

[50] A. Orte et al. “2’,7’-Difluorofluorescein Excited-State Proton Reactions: Correlation between Time-Resolved Emission and Steady-State Fluorescence Intensity”. In: *Journal of Physical Chemistry A* 109.12 (2005), pp. 2840–2846. ISSN: 10895639. DOI: 10.1021/jp044681m.

[51] A. Orte et al. “Three-State 2′,7′-Difluorofluorescein Excited-State Proton Transfer Reactions in Moderately Acidic and Very Acidic Media”. In: *Journal of Physical Chemistry A* 109.39 (2005), pp. 8705–8718. ISSN: 10895639. DOI: 10.1021/jp051264g.

[52] P. Milas. “Single Molecule Studies of a Short RNA”. In: *Doctoral Dissertations* 269 (Sept. 1, 2014). DOI: 10.7275/5hm5-h206.

[53] P. C. Gregory. *Bayesian Logical Data Analysis for the Physical Sciences: A Comparative Approach with Mathematica Support*. Cambridge, UK; New York: Cambridge University Press, 2005. ISBN: 978-0-521-84150-4.

[54] E. Rusinova et al. “Alexa and Oregon Green Dyes as Fluorescence Anisotropy Probes for Measuring Protein-Protein and Protein-Nucleic Acid Interactions”. In: *Analytical Biochemistry* 308.1 (2002), pp. 18–25. ISSN: 00032697. DOI: 10.1016/S0003-2697(02)00325-1.

[55] J. Crocker and D. Grier. “Methods of Digital Video Microscopy for Colloidal Studies”. In: *Journal of Colloid and Interface Science* 179.1 (1996), pp. 298–310. ISSN: 00219797. DOI: 10.1006/jcis.1996.0217.

[56] D. B. Allan et al. *Trackpy: Trackpy V0.4.1*. Apr. 21, 2018. DOI: 10.5281/zenodo.1226458.

[57] S. van der Walt et al. “Scikit-Image: Image Processing in Python”. In: *PeerJ* 2 (June 19, 2014), e453. ISSN: 2167-8359. DOI: 10.7717/peerj.453.

[58] J. D. Hunter. “Matplotlib: A 2D Graphics Environment”. In: *Computing in Science Engineering* 9.3 (May 2007), pp. 90–95. ISSN: 1521-9615. DOI: 10.1109/MCSE.2007.55.

[59] T. A. Caswell et al. *Matplotlib/Matplotlib v3.0.2*. Zenodo, Nov. 10, 2018. DOI: 10.5281/zenodo.1482099.

[60] E. Jones, T. Oliphant, P. Peterson, et al. *SciPy: Open Source Scientific Tools for Python*. 2001–.

[61] D. B. Murphy. *Fundamentals of Light Microscopy and Electronic Imaging*. New York: Wiley-Liss, 2001. 368 pp. ISBN: 978-0-471-25391-4.

[62] B. Turkowyd, D. Virant, and U. Endesfelder. “From Single Molecules to Life: Microscopy at the Nanoscale”. In: *Analytical and Bioanalytical Chemistry* 408.25 (Oct. 2016), pp. 6885–6911. ISSN: 16182650. DOI: 10.1007/s00216-016-9781-8.

[63] T. Ha and P. Tinnefeld. “Photophysics of Fluorescent Probes for Single-Molecule Biophysics and Super-Resolution Imaging”. In: *Annual Review of Physical Chemistry* 63.1 (2012), pp. 595–617. ISSN: 0066-426X. DOI: 10.1146/annurev-physchem-032210-103340.

[64] C. G. Hübner et al. “Direct Observation of the Triplet Lifetime Quenching of Single Dye Molecules by Molecular Oxygen”. In: *The Journal of Chemical Physics* 115.21 (Nov. 14, 2001). 00112, pp. 9619–9622. ISSN: 0021-9606. DOI: 10.1063/1.1421382.

[65] P. V. Patil and D. P. Ballou. “The Use of Protocatechuate Dioxygenase for Maintaining Anaerobic Conditions in Biochemical Experiments”. In: *Analytical Biochemistry* 286.2 (2000), pp. 187–192. ISSN: 00032697. DOI: 10.1006/abio.2000.4802.

[66] C. E. Aitken, R. A. Marshall, and J. D. Puglisi. “An Oxygen Scavenging System for Improvement of Dye Stability in Single-Molecule Fluorescence Experiments”. In: *Biophysical journal* 94.5 (2008), pp. 1826–1835. ISSN: 00063495. DOI: 10.1529/biophysj.107.117689.

[67] T. Cordes, J. Vogelsang, and P. Tinnefeld. “On the Mechanism of Trolox as Antiblinking and Antibleaching Reagent”. In: *Journal of the American Chemical Society* 131.14 (2009), pp. 5018–5019. ISSN: 00027863. DOI: 10.1021/ja809117z.

[68] J. Vogelsang et al. “A Reducing and Oxidizing System Minimizes Photobleaching and Blinking of Fluorescent Dyes”. In: *Angewandte Chemie - International Edition* 47.29 (2008), pp. 5465–5469. ISSN: 14337851. DOI: 10.1002/anie.200801518.

[69] J. Vogelsang et al. “Controlling the Fluorescence of Ordinary Oxazine Dyes for Single-Molecule Switching and Superresolution Microscopy”. In: *Proceedings of the National Academy of Sciences* 106.20 (2009), pp. 8107–8112. ISSN: 0027-8424. DOI: 10.1073/pnas.0811875106.

[70] A. Einstein and R. Fürth. *Investigations on the Theory of Brownian Movement*. 00514 OCLC: 17520631. New York, N.Y.: Dover Publications, 1956. ISBN: 978-0-486-60304-9.

[71] H. Qian, M. P. Sheetz, and E. L. Elson. “Single Particle Tracking. Analysis of Diffusion and Flow in Two-Dimensional Systems”. In: *Biophysical Journal* 60.4 (Oct. 1, 1991). 01029, pp. 910–921. ISSN: 0006-3495. DOI: 10.1016/S0006-3495(91)82125-7.

[72] S. Chandrasekhar. “Stochastic Problems in Physics and Astronomy”. In: *Reviews of Modern Physics* 15.1 (Jan. 1, 1943). 09618, pp. 1–89. DOI: 10.1103/RevModPhys.15.1.

[73] X. Michalet. “Mean Square Displacement Analysis of Single-Particle Trajectories with Localization Error: Brownian Motion in an Isotropic Medium”. In: *Physical Review E - Statistical, Nonlinear, and Soft Matter Physics* 82.4 (2010), pp. 1–13. ISSN: 15393755. DOI: 10.1103/PhysRevE.82.041914.

[74] X. Michalet and A. J. Berglund. “Optimal Diffusion Coefficient Estimation in Single-Particle Tracking”. In: *Physical Review E - Statistical, Nonlinear, and Soft Matter Physics* 85.6 (2012), pp. 1–14. ISSN: 15393755. DOI: 10.1103/PhysRevE.85.061916.

[75] A. J. Berglund. “Statistics of Camera-Based Single-Particle Tracking”. In: *Physical Review E* 82.1 (July 22, 2010). 00126, p. 011917. DOI: 10.1103/PhysRevE.82.011917.

[76] B. Zhang, J. Zerubia, and J.-C. Olivo-Marin. “Gaussian Approximations of Fluorescence Microscope Point-Spread Function Models”. In: *Applied Optics* 46.10 (Apr. 1, 2007). 00389, pp. 1819–1829. ISSN: 2155-3165. DOI: 10.1364/AO.46.001819.

[77] R. E. Thompson, D. R. Larson, and W. W. Webb. “Precise Nanometer Localization Analysis for Individual Fluorescent Probes”. In: *Biophysical Journal* 82.5 (2002), pp. 2775–2783. ISSN: 00063495. DOI: 10.1016/S0006-3495(02)75618-X.